Diss. ETH Nr. 21988

Cycle-resolved analysis and modeling of knock in a homogeneous charge spark ignition engine fueled by ethanol and iso-octane

A thesis submitted to attain the degree of

DOCTOR OF SCIENCES of ETH ZURICH

(Dr. sc. ETH Zurich)

presented by

KAREL FRANS HILDA MARIA STEURS

Master in Electromechanical Engineering, University of Ghent,
born on 03.09.1984,
citizen of Belgium

Accepted on the recommendation of:
Prof. Dr. K. Boulouchos, examiner
Prof. Dr. T. Koch, co-examiner

2014

Preface

The present work was carried out at the Aerothermochemistry and Combustion Systems Laboratory (LAV) at the Swiss Federal Institute of Technology (ETH) in Zurich, Switzerland within the framework of the CoHyb project funded by the Swiss Competence Center for Energy and Mobility (CCEM).

I would like to thank Prof. Dr. K. Boulouchos for his support, his input and for giving me the chance of completing this work. I thank Prof. Dr. Th. Koch for the co-examination of this work.

I would like to thank the Competence Center for Energy and Mobility for funding the project as well as the project partners from IDSC/ETH and EMPA for the pleasant and fruitful cooperation. I would also like to mention all thesis students that have contributed to this work: A. Liebl, A. Bhat, C. Üresin, C. Blomberg, D. Willi, G. Lucchini, G. Georges, M. Egli, R. Postiglione, T. Nyitray, A. Inderbitzin, D. Schuler, M. Hörantner, A. Rossi, C. Bielitz, G. Tahiraj, M. Ferretti, L. Morales and T. Nagalingam. I would like to thank also the partners of other research project I have participated in during my time as a doctoral student, in particular those of the Paul Scherer Institute, MAHLE Behr GmbH & Co. KG, Audi AG, EWZ, SUNCAR and ETH groups IVT and PSL for the interesting and enjoyable collaboration.

I would like to thank all my friends and colleagues at LAV for creating a pleasant working environment. In particular I would like to thank P. Obrecht for his care and advice and C. Blomberg for his contributions to this work.

I want to thank the technical staff, G. Egli, M. Décosterd, P. Eberli and M. Wegmann, for their excellent job and devotion.

Last but not least I am very grateful to my parents, my family and my friends both in Switzerland and Belgium for their belief and support.

Abstract

The main limiting factor for the efficiency of spark ignition engines is knock, caused by the auto-ignition of the unburned mixture in front of the flame. The use of alternative renewable fuels with high octane numbers, such as ethanol, is ever increasing. The design of future dedicated engines will benefit greatly of a thorough understanding of the knock phenomenon and the availability of fast and reliable knock prediction models.

In order to study knock in a systematic way, experiments with ethanol and iso-octane have been carried out on a 250cc single cylinder spark ignition test engine with variable intake temperatures at wide open throttle and stoichiometric premixed fuel/air mixtures. At different speeds and intake temperatures spark angle sweeps have been performed ranging from late timing and non-knocking combustion up to early timing and strong knocking conditions.

A 1-D engine simulation model is used to calculate the heat release rates and burned/unburned zone temperatures. Special attention is given to the heat transfer in the cylinder and the intake port during the intake and compression strokes to accurately determine the temperature of the unburned mixture and the related sensitivities are explored.

A criterion for knock detection based on the amplitude of the characteristic pressure oscillations is used in this work. The onset of knock timing is found using the heat release rate preceding the pressure oscillations. As expected, much earlier and stronger knock can be observed for iso-octane compared to ethanol at otherwise same engine operating conditions. This is due to the cooling effect and higher octane number of ethanol and leads to different cycle-to-cycle variation behavior.

Detailed chemical kinetic mechanisms are used to compute ignition delay times for stoichiometric ethanol/air and iso-octane/air mixtures

at conditions relevant to the measurements and are compared to empirical correlations available in literature. The different correlations are used in a knock model approach and are tested against the measurement data. The importance of using accurate ignition delay time expressions in predicting the correct timing for the onset of knock is illustrated for both ethanol and iso-octane.

It is observed for both fuels and all intake temperatures that the probability of the occurrence of knock is significantly reduced towards the end of the cycle. In this case all the unburned fuel is close to the cylinder walls that are acting as a heat sink, making auto-ignition of the unburned gas impossible. A new model approach for the thermal boundary layer close to the cylinder walls is included in the knock integral to take into account its effect on the knock probability thus improving significantly the accuracy of the knock prediction. The formulation of the knock model can be derived from the geometry of the combustion chamber and includes its specific shape.

Zusammenfassung

Der wichtigste limitierende Faktor für den Wirkungsgrad von Ottomotoren ist das Klopfen, das durch die Selbstzündung vom Gemisch vor der Flamme ausgelöst wird. Alternative Kraftstoffe mit hohen Oktanzahlen, so wie Ethanol, werden immer häufiger im Automobilbereich eingesetzt. Ein grundlegendes Verständnis von den physikalischen und chemischen Vorgängen während des Klopfens, sowie die Verfügbarkeit von schnellen und zuverlässigen rechnerbasierten Klopfmodellen, sind bei der Entwicklung von neuen Motoren von hoher Wichtigkeit.

In dieser Arbeit wurde zur systematischen Untersuchung des Klopfens, Experimente an einem 250cc Einzylinder- Ottomotor, mit jeweils stöchiometrischen und vorgemischten Ethanol und Iso-Oktan und offener Drosselklappe durchgeführt. Ein grosser Datensatz mit unterschiedlichen Klopfintensitäten wurde für Zündwinkelvariationen bei variablen Drehzahlen und Einlasstemperaturen generiert und im Folgenden analysiert.

Ein 1-D Motorensimulationsmodel wurde für die Berechnung von der Wärmefreisetzung und den Temperaturen der verbrannten und unverbrannten Zone eingesetzt. Besondere Aufmerksamkeit wurde auf den Wärmeaustausch im Zylinder und dem Einlassbereich gerichtet, um die genaue Temperatur des unverbrannten Gemisches während Einlass und Kompression und dessen Einflüsse zu bestimmen.

Ein Kriterium für die Erkennung von klopfenden Zyklen wurde anhand der Amplitude der charakteristischen Druckschwingungen formuliert. Der Zeitpunkt der Selbstzündung wird aufgrund der Wärmefreisetzung, die den Druckschwingungen vorabgeht, bestimmt. Die Klopfneigung von Iso-Oktan ist, gemäss den Erwartungen, wegen dem Kühlungseffekt und der höheren Oktanzahl von Ethanol höher und führt daher zu einem anderen Zyklenverhalten.

Detaillierte kinetische Reaktionsmechanismen werden für die Be-

rechnung der Zündverzüge von stöchiometrischen Ethanol/Luft und Iso-Oktan/Luft Gemischen, bei motorrelevanten Bedingungen eingesetzt und die Resultate mit empirischen Korrelationen aus der Literatur verglichen. Die einzelnen Korrelationen werden wiederum in Klopfmodellen benutzt und direkt mit den Messdaten verglichen. Der Wichtigkeit von genauen Zündverzugskorrelationen für die korrekte Vorhersage vom Klopfbeginn für sowohl Ethanol als auch Iso-Oktan wird aufgezeigt.

Die Wahrscheinlichkeit des Klopfens reduziert sich stark für beide Kraftstoffe und alle Einlasstemperaturen gegen Ende des Zyklus. In diesem Fall ist der gesamte Restkraftstoff nahe der Wand lokalisiert, die als Wärmesenke agiert und somit die Selbstzündung vom noch unverbrannten Kraftstoff verhindert. Das allgemein angewendete Klopfintegral wird mit einem neuen Modellansatz für die thermische Grenzschicht an der Zylinderwand erweitert. Somit wird die Genauigkeit der Vorhersage vom Klopfen für verschiedene Kraftstoffe wesentlich verbessert. Daher ist die spezifische Formulierung vom Klopfmodell allein von der Geometrie vom Brennraum abhängig.

Contents

Contents

1 Introduction

There is a serious trend in the automotive industry towards more economic and ecologic vehicles. Increasing environmental awareness and fluctuating gas prices have increased the demand for cars with very low fuel consumption and CO_2 emissions. A common measure to decrease the carbon footprint is the use of alternative fuels. In this light ethanol has gained much interest over the last years, mainly due to its excellent knock resistance and the possibility to be produced in a renewable way.

In this work the use of ethanol in spark ignition engines is studied and specifically its behavior under knocking conditions. The results are then compared to those of a common surrogate for gasoline, iso-octane. Knock, which is caused by the auto-ignition of the unburned mixture in the end-zone of the combustion chamber, is often the limiting factor for brake efficiency in spark igntion engines. The design of future ethanol-fueled engines will benefit greatly from a thorough understanding of the knock phenomenon.

1.1 Ethanol as a renewable fuel

Ethanol can be used as a fuel for automotive applications and its use is increasing. Ethanol is often blended with regular gasoline in low volume percentages, typically between 5 and 10% (E5 and E10) as an octane enhancer or in high volume percentages known as E85. Contrary to gasoline, ethanol can be gained from agricultural products and can therefore be categorized as a renewable fuel.

Figure 1.1 shows the global ethanol production in recent years broken down for the main production regions. Up to 2010 the global production of ethanol has been steadily increasing. Since 2010 there has been a small reduction, mainly due to economic factors in the most
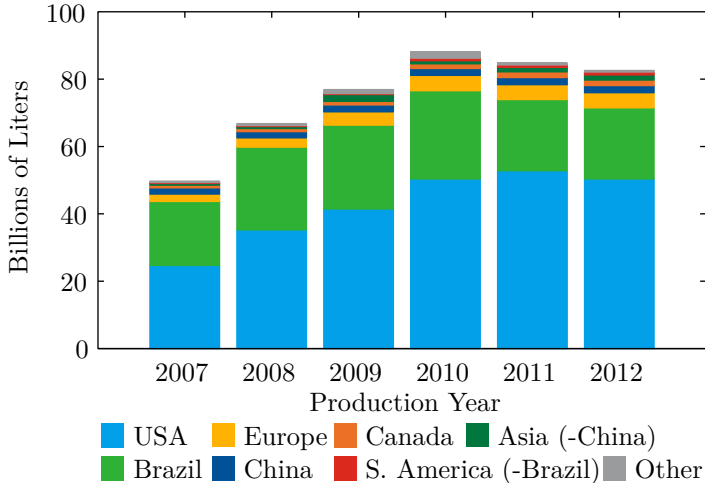
Figure 1.1: *Global ethanol production in the period 2007 - 2012 broken down geographically [1].*

important production countries. However the predictions for the future foresee a further increase in the production [2]. Ethanol can be produced essentially in two different ways: by fermentation of sugars or by chemical synthesis without a fermentation step. The two main production countries in the world use corn (USA) or sugar cane (Brazil). The use of these crops for fuel production is in direct competition with the food market and these fuels are commonly called 1st generation bio-fuels. Ethanol produced from edible agricultural products use the fermentation process. Alternatively ethanol can be produced from lignocellulosic materials, which include agricultural residues, grasses and wood residues. Ethanol produced from these sources is called 2nd generation bio-ethanol or cellulosic ethanol [3]. Production of ethanol from lignocellulosic materials is also based on the fermentation process, but the cellulose must first be converted to sugars. An overview of the different production processes for ethanol from corn and lignocellulose can be found in [4]. Another option for 2nd generation bio-fuels is the gasification of biomass to syngas (H_2 + CO) followed by the catalytic conversion of syngas to ethanol [5]. Non-renewable ethanol can be produced using catalytic hydratation of ethylene or the gasification of fossil fuels to syngas.
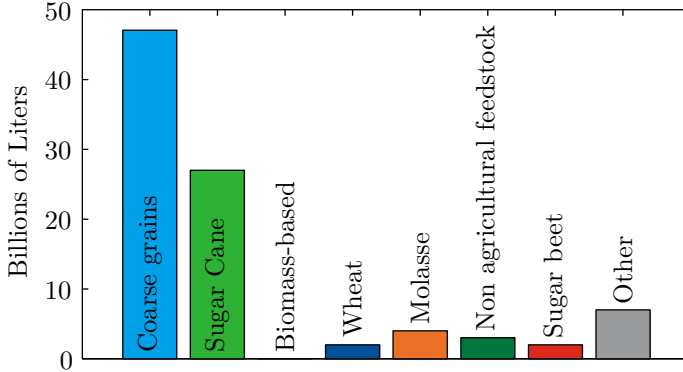
Figure 1.2: *Global ethanol production in the year 2010 broken down by feedstock used [2].*

An overview of the global ethanol production broken down by feedstock can be seen in figure 1.2. The main sources are, as mentioned, coarsed grains (corn) and sugar cane. With wheat, molasse and sugar beets the majority of ethanol produced is of the 1st generation. Bioethanol produced from lignocellulosic materials does not yet allow large scale production, mainly due to the costly conversion process into sugars [2]. The USA however passed the Energy Independence and Security Act in 2007, requiring a minimum of 36 billion gallons of ethanol to be produced in 2022 of which 15 billion gallons from cellulosic material, which reduces the life-cycle green house gas emissions by at 60% [6].

Next to the competition with food market, the sustainability of ethanol as a fuel depends strongly on the efficiency of the production cycle. Depending on the geographic location of the production, the feedstock, the input data used, etc. the life cycle analysis of the well-to-tank production chain can change significantly in terms of greenhouse gas emissions, primary energy demand and other environmental factors such as deforestation and the availability of clean water [7,8]. With the right combination of these factors the production of ethanol can be both renewable and sustainable, making it a viable long-term option for the automotive industry.

1.2 Current commercial use of ethanol as a transportation fuel

The use of ethanol in transportation fuels can be divided into two categories: low volume ethanol blends in gasoline for the use in regular cars and high volume or pure ethanol for the use in flex fuel vehicles.

In Europe ethanol is allowed in regular gasoline for all vehicles in a concentration up to 5% volume and for newer vehicles up to 10% volume (E10) [9]. In the USA the ethanol content in gasoline varies throughout the country. Ethanol levels up to 10% volume are sold at most gas stations. E15 is approved for all vehicles newer than 2001 [10].

On the other end of the spectrum E85, with nominally 85%vol ethanol and 15% gasoline, is becoming the standard for high volume ethanol blends. A minimum of 50% ethanol is required and the actual composition varies regionally and seasonally [11, 12]. Within Europe, Sweden is the country with the highest availability of E85 with over 2100 filling stations [13]. Germany only offers 340 [14] and Switzerland 38 [15]. In the USA 3306 filling stations with E85 are registered [16] with the highest density in the mid-west, where most ethanol is produced.

Brazil has the highest availability of ethanol fuels worldwide. The ethanol content in gasoline is nominally set to 22% but varies between 18 and 25%. Because of the relatively high volume fraction of ethanol Brazil's gasoline is also called gasohol. Ethanol is available as E100 as well without gasoline. Most cars are flex fuel vehicles, which means they can be fueled with any combination of E100 and gasohol, depending on availability and price [17].

1.3 State of the art in ethanol-fueled engines

The octane number (ON) of ethanol is higher than that of gasoline, making the fuel more knock resistant. At low volume blends ethanol is used as an octane enhancer for gasoline [18]. The octane number increases linearly with the molar concentration of ethanol in gasoline [19], which means the octane benefit is marginally higher for low ethanol blends. At high ethanol blends or pure ethanol, the complete potential

of the fuel can be exploited by advancing the spark timing, increasing the compression ratio (CR) or the boost pressure. A typical correlation for the CR gives 1 point of CR for 5 points octane number [20]. Caton [21] determines 5 degrees of spark advance per point of CR for gasoline and about 2 degrees for E85. All spark ignition (SI) engines are eventually knock limited. Because the brake efficiency of an engine scales with the CR, a high ON is an important benefit in SI engines.

The performance of different ethanol blends in terms of fuel consumption, power output, brake efficiency and pollutant emissions has been compared to regular gasoline operation in many publications. The results can be divided in three categories that yield different statements.

In a first category comparisons between ethanol blends and gasoline are made at wide open throttle (WOT) [21–33]. An increase in torque output at full load is usually observed for higher ethanol content, which is mainly due to a better spark timing. Due to the higher knock resistance of ethanol compared to gasoline, earlier spark timings at wide open throttle are possible for ethanol containing fuels and maximum brake torque (MBT) timing can be sustained where gasoline is knock limited. Earlier spark timings and overall lower combustion temperatures for ethanol often remove the requirement for fuel enrichment. This leads to an increase in both brake power and brake thermal efficiency (BTE). The better knock resistance of ethanol can even allow an increase of the CR in order to obtain even higher BTE. It has been shown that the MBT timing doesn't change significantly for different blends. The gains in BTE stagnate when MBT timing can no longer be sustained with ethanol at WOT [26]. A higher CR shifts MBT towards top dead center (TDC) and decreases combustion time.

In a second comparison (e.g. [34]) the brake torque is kept constant for all fuels. This case is a good comparison for part load behavior. At the same throttle position a higher ethanol content increases the brake torque production. In a comparison at constant torque more throttling is required and higher pumping losses lead to lower efficiency benefits for ethanol.

In a third and last category comparisons are made without closed loop mixture control [35–39]. A constant injection timing for all ethanol blends leads to changes in the air-to-fuel ratio. Due to the lower volumetric energy density of ethanol, the mixture becomes leaner with increasing ethanol content in the fuel. The lower energy content leads to a decrease in torque production, however the leaning effect leads to an increase in BTE. Due to the higher latent heat of vaporization the

volumetric efficiency improves with increasing ethanol content.

Many of the cited studies report comparisons of the pollutant emissions during their tests. There is no unique effect of ethanol content in the fuel on the pollutant emissions. An increase or decrease in the emissions is mainly due to the operation point shift caused by the addition of ethanol and is thus a function of the method of comparison. Nitrogen oxide (NOx) emissions are created at high temperatures when enough oxygen is available. Due to the higher latent heat of vaporization, the overall temperature in the combustion chamber is lower for higher ethanol content, which has the effect of reducing NOx emissions. Because of the higher knock resistance of ethanol, the ignition timing can be advanced and higher peak temperatures are reached. Carbon monoxide (CO) is formed in SI engines when there is a lack of oxygen and are a result of incomplete combustion. The CO emissions are primarily a function of air-to-fuel ratio. In the open loop mixture control measurements CO emissions reduced due to the leaning effect. It has been reported that the oxygen content in ethanol reduced the CO emissions [25, 40]. Unburned hydrocarbons (HC) are emitted as a result of incomplete combustion. The main reasons for HC emissions are flame quenching on the cylinder wall, unburned fuel in the piston crevices, absorption and desorption of fuel vapor in the oil, unstable combustion and rich air to fuel mixtures. Earlier spark timings and colder combustion temperatures at higher ethanol volume fractions cause therefore higher HC emissions. Issues with cold start, associated with high ethanol content fuels, are an important source of HC emissions as well [41]. Next to the regulated emissions (NOx, CO and HC), ethanol combustion produces emissions of non-regulated components which can be harmful to humans and the environment and of which aldehydes are the most important. Exhaust aldehydes are formed from post-flame oxidation of unburned alcohol and are thus directly related to the unburned fuel fraction and the conditions during exhaust and in the exhaust pipe. The formation is initiated after the end of combustion. Aldehyde emissions are only relevant in alcohol containing fuels and formaldehyde and acetaldehyde are the main components. Aldehyde concentrations reduce slightly due to the lower temperatures in the exhaust. A higher compression ratio results in a more efficient combustion and reduces the unburned fuel fraction which results in lower aldehyde formation [42–45].

The studies in the overview so far mainly use port fuel injection (PFI). The benefit of the charge cooling effect of ethanol is much more

pronounced for direct injection engines (DI) [46, 47], because more of the heat required for the evaporation of the fuel is taken from the incoming air and not the intake walls. The potential for gains in brake efficiency and power are thus higher with direct injection. A direct injection system can also reduce problems during cold start [48–59]. However the low volatility of ethanol can cause improper mixing and a high production of soot particles.

Compared gasoline ethanol can allow much higher levels of turbocharging and exhaust gas recirulation (EGR). Due to the excellent knock resistance of ethanol, turbocharging can be used to increase power output or have a high degree of engine downsizing. EGR can be used to reduce the peak combustion temperatures and consequently avoid knock and high NOx emissions. Ethanol has a higher flame speed and also broader dilution limits compared to gasoline and can thus sustain higher rates of EGR. Several prototype engines for high ethanol content fuels have been presented that use a combination of high CR, turbocharging and EGR to reach high brake efficiencies of over 40% [60–62].

Due to the limited availability of high ethanol content fuels in most countries, engines designed for the operation with ethanol are typically installed in flex-fuel concepts. Either the benefits of ethanol in terms of knock resistance and charge cooling are exploited, in which case there are serious reductions in power output and brake efficiency when using gasoline. Or the engine is designed for the use with gasoline and there are only little efficiency benefits when using ethanol. Concepts using a two tank, dual injection system have been proposed in which ethanol is only used for knock suppression and can be filled according to availability [63–68]. Depending on the price of ethanol, an optimal ethanol blend can be found between efficiency and fuel consumption [18].

As mentioned, high ethanol content fuels can suffer from cold start problems. A direct injection system can improve cold start behavior significantly [28]. Other measures include intake port and injector heaters [26], open valve injection [69], air-assist injectors [70], a separate gasoline system [71], increased spark energy [72] or valve time optimization [73].

1.4 Motivation and objectives

The literature review in the previous section shows that there is a large interest in ethanol fueled engines. With minor changes to a regular gasoline engine significant increases in power output and reduction in CO_2 emissions are reported. High efficiency spark ignition engine concepts are possible due to the excellent knock resistance of ethanol. In order to fully benefit from the specific properties of ethanol as a fuel, dedicated ethanol engines need to be designed instead of using ethanol in a gasoline engine. Only these engines can offset, to some extent, the lower volumetric energy density of ethanol - and thus reduced range - with higher brakes efficiencies. These dedicated ethanol engines are designed for the knock limits of ethanol. A fundamental understanding of the behavior of ethanol under knocking conditions is thus of crucial importance for the design of these engines. Therefore the study of knock in ethanol fueled engines is the main subject of this work. A comparison is made to the results obtained using iso-octane, a primary reference fuel and common surrogate for gasoline, under the same conditions. Cycle-to-cycle variations are unavoidable in the high turbulence environment of an internal combustion engine and play a large role in the knock phenomenon. A cycle-resolved analysis of the results gives a better insight into which cycles are more prone to auto-ignition of the end gas. Relating the timing for the onset of knock to the flame propagation shows the influence of the geometry of the combustion chamber. In the initial development phase of spark ignition engines, 0D and 1D simulation software, that rely heavily on empirical and phenomenological models to predict the performance of the simulated engine, are often used to define the main parameters of the engine. Because knock sets limits to peak pressures and temperatures in spark ignition engines, the availability of fast and reliable models for the prediction of knock is of crucial importance during this phase. The results obtained in this work are thus used to test the performance the knock models available in literature and formulate improvements based on the observations that are made. The current work does not use calculation intensive 3D simulations or engines with optical access, but shows that with standard equipment and fundamental understanding of the phenomena, accurate results can be obtained.

The structure of the report is as follows:

- In chapter 2 the experimental setup, the investigated conditions

and the selected fuels are presented. The specific properties of the fuels are discussed in more detail, because they are inherent to understanding the differences in the results obtained with both fuels.

- In a following chapter the thermodynamic analysis of the combustion process is explained. The accuracy of the calculations of the unburned temperatures and the heat release rates are very important for a correct analysis of the study of knock. A parameter study is included to show the sensitivity of the results.

- In chapter 4 the knock criterion used in this work is defined, which determines when a cycle is detected as a knocking cycle. A definition for the timing for the onset of knock is presented as well.

- The ignition delay time is an important value used in knock models. Chapter 5 gives an overview of the available ignition delay time correlations.

- The selected knock models are presented in chapter 6. A method for the assessment of the performance of different knock models is introduced.

- Chapter 7 discusses the influence of the cylinder walls on the occurrence of knock. A model for the thermal boundary layer is presented.

- In chapter 8 the different methodologies and models are applied to the data gathered on the test bench. The results of the analysis are presented and their impact discussed.

This introduction chapter does not contain an extensive literature review on all aspects of the study. Each chapter is structured in such a way that in a first section the state of the art in literature is presented. In further sections the approach that is chosen for this work in particular on the respective topic is justified and its added value underlined.

2 Fuel properties and experimental setup

In order to study knock experimentally, an engine test bench has been installed. This chapter describes the selected fuels, the test engine, the design of the test bench, the modifications to the original engine and the sensors used to record data. Furthermore, the measurement operating points as well as the measurement procedures are specified.

2.1 Fuel properties

Two fuels are selected for this study of knock: ethanol and iso-octane. Table 2.1 lists the main properties of these fuels and compares with typical values for regular gasoline. Each of the following sections compares one aspect of the differences between both fuels. Understanding the specific properties of the fuels allows the explanation of the observed differences in the experimental data and to interpret the modeling results.

Fuel molecules and combustion equations

While gasoline is a blend of different molecular components, ethanol and iso-octane are single molecular fuels. Ethanol contains an oxygen atom, which makes it a so-called oxygenated fuel. The complete combustion equations for stoichiometric ethanol/air and iso-octane/air mixtures can be seen in equation 2.1 and 2.2 respectively.
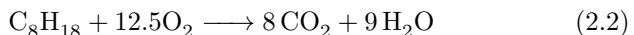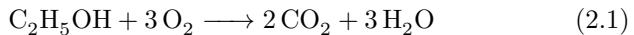
$$C_2H_5OH + 3\,O_2 \longrightarrow 2\,CO_2 + 3\,H_2O \tag{2.1}$$

$$C_8H_{18} + 12.5O_2 \longrightarrow 8\,CO_2 + 9\,H_2O \tag{2.2}$$

Table 2.1: *Fuel properties [74].*

		Gasoline	Ethanol	Iso-octane
Chemical Formula		C_4 - C_{12}[1]	C_2H_5OH	C_8H_{18}
Molecular weight	$\left[\frac{g}{mol}\right]$	100-105	46.07	114.23
Density[2]	$\left[\frac{kg}{l}\right]$	0.72-0.78	0.794	0.692
Latent heat of vaporization[2]	$\left[\frac{kJ}{kg}\right]$	348	920	307
Lower heating value	$\left[\frac{MJ}{kg}\right]$	41.8 - 44.2	26.75	44.42
Stoichiometric air to fuel ratio	$[-]$	14.7	9.00	14.7
RON	$[-]$	90 - 100	107-109	100
MON	$[-]$	80 - 90	89-90	100
Carbon mass frac.	$[\%]$	85 - 88	52.2	84.12
Hydrogen mass frac.	$[\%]$	12 - 15	13.1	15.88
Oxygen mass frac.	$[\%]$	0	34.7	0
Boiling point	$[°C]$	26 - 225	78.5	99.1
Reid vapor pressure	$[bar]$	0.55 - 1	0.158	0.55
Autoignition temp.	$[°C]$	257	696	396

[1] Number of carbon atoms in the corresponding hydrocarbons
[2] at 15.5°C

Based on these equations, the specific CO_2-emissions per energy of fuel burned can be calculated. Equations 2.3 and 2.4, with M, the molecular weight and H_u, the lower heating value, show that there is only a small difference in CO_2-emissions when fuel with the same amount of energy is burned. Only differences in engine efficiency and well-to-tank emissions can change the specific CO_2 emissions.

$$\frac{2 \cdot M_{CO_2}}{M_{C_2H_5OH} \cdot H_{u,C_2H_5OH}} = 71.5 \frac{kg_{CO_2}}{MJ_{C_2H_5OH}} \quad (2.3)$$

$$\frac{8 \cdot M_{CO_2}}{M_{C_8H_{18}} \cdot H_{u,C_8H_{18}}} = 69.4 \frac{kg_{CO_2}}{MJ_{C_8H_{18}}} \quad (2.4)$$

Energy density

Ethanol has a much lower energy density than gasoline or iso-octane. In order to have the same energy in the cylinder, 66% more ethanol

needs to be injected compared to iso-octane.

$$\frac{H_{u,Eth}}{H_{u,C_8H_{18}}} = \frac{26.75 MJ/kg}{44.42 MJ/kg} = 0.6022 \qquad (2.5)$$

Ethanol however has a higher density at the same conditions. The necessary volume of ethanol to be injected in order to obtain the same energy in the cylinder is almost 45% higher than for iso-octane.

$$\frac{H_{u,Eth} * \rho_{Eth}}{H_{u,C_8H_{18}} * \rho_{C_8H_{18}}} = 0.6022 * \frac{0.794 kg/m^3}{0.692 kg/m^3} = 0.691 \qquad (2.6)$$

This has a significant influence on e.g. the fuel injectors to be installed. They need to be designed for the increased volume flow. In particular for flex fuel vehicles, where both gasoline and ethanol operation is possible, this is a requirement [67].

Because ethanol is an oxygenated fuel, the stoichiometric air-to-fuel ratio is lower compared to gasoline or iso-octane. This means that on a mass basis, for the same amount of air less fuel is required to obtain a stoichiometric mixture. In this light the considerations from equations 2.5 and 2.6 have to be reevaluated. If an engine is operated with same amount of air in the cylinder after IVC for both ethanol and iso-octane and the mixture in both cases is stoichiometric, the difference in energy contained in the cylinder can be calculated. Equation 2.7 shows that even though the mass of ethanol required is higher, the energy content is the same.

$$\frac{14.7\frac{kg_{Air}}{kg_{C_8H_{18}}}}{9.0\frac{kg_{Air}}{kg_{Eth}}} \rightarrow 1.633\frac{kg_{Eth}}{kg_{C_8H_{18}}} \cdot \frac{26.75\frac{MJ_{Eth}}{kg_{Eth}}}{44.42\frac{MJ_{C_8H_{18}}}{kg_{C_8H_{18}}}} = 0.9836\frac{MJ_{Eth}}{MJ_{C_8H_{18}}} \qquad (2.7)$$

Even though the energy content within the cylinder stays approximately the same for the same volumetric efficiency, the volumetric fuel consumption of ethanol increases. Assuming that the operation of both fuels yields the same efficiency map, the volumetric fuel consumption of ethanol increases by 44.7 %. Assuming the same price for one liter gasoline and one liter ethanol the cost of driving would increase by this amount. For the same fuel tank this results in a reduction of the range with one filling by 30.9%.

Latent heat of vaporization

The latent heat of vaporization, L, of ethanol is three time higher than that of iso-octane. This means that the heat required to evaporate the same fuel mass is much higher for ethanol compared to iso-octane. The use of ethanol in spark ignition engines is therefore often associated with cold start problems and mixing difficulties. On the other hand the high latent heat of evaporation has great advantages in terms of filling and efficiency. During ethanol evaporation, the incoming air is cooled down, leading to overall lower temperatures during the combustion cycle. Cooler charge air means higher density and a higher volumetric efficiency. The heat required to evaporate a certain fuel mass, m_f, can be calculated as in equation 2.8.

$$Q_L = m_f L \tag{2.8}$$

Due to the lower energy density of ethanol the amount of fuel for the same amount of air is 1.63 (= 14.7/9) times higher. In order to evaporate a stoichiometric mixture with the same air mass is 4.89 times more energy is required for ethanol compared to iso-octane, as shown in equation 2.9.

$$\frac{Q_{L,Eth}}{Q_{L,\mathrm{C_8H_{18}}}} = \frac{14.7}{9} \cdot \frac{L_{Eth}}{L_{\mathrm{C_8H_{18}}}} = 4.89 \tag{2.9}$$

The heat required for the evaporation can come from the incoming air, but also from the piping, the cylinder walls, etc. For port fuel injection relatively more heat is taken from the piping. Depending on how the injection system is designed, a larger or lower fraction of the injected fuel is impinged on the intake piping. Fuel evaporating from the fuel puddle in the intake, takes its heat by cooling down the walls rather than the incoming air. With a direct injection system, the heat taken from the incoming air is typically higher [47]. However these observations are similar for the design of the fuel spray. Depending on how much of the fuel is impinged on the piston and the liner walls, the heat taken from the charge air can vary. Assuming all heat for the evaporation of the fuel is taken from the charge air, the reduction in temperature for complete evaporation of the fuel of a stoichiometric mixture can be calculated. The heat to evaporate the fuel equals the heat for the reduction in temperature of the charge air, ΔT, as in equation 2.10, where AF_{ST} is the stoichiometric air-to-fuel ratio, and c_p the specific heat capacity.
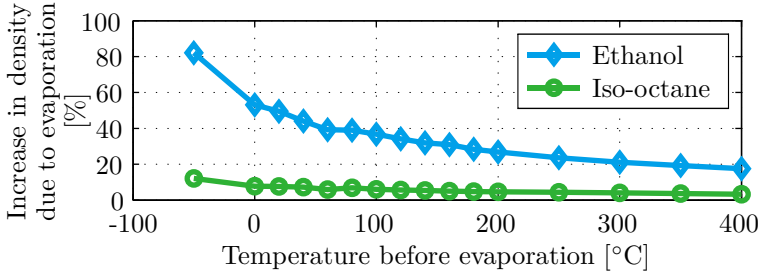
Figure 2.1: *Increase in charge density due to evaporation of the fuel as a function of the temperature before evaporation when all the required heat is taken from the charge air.*

$$\frac{m_{air}}{AF_{st}} \cdot L = c_p m_{air} \Delta T \tag{2.10}$$

The reduction in temperature under this assumption is independent of the operating point (speed, load, spark angle, etc.) for stoichiometric mixtures and is given in equation 2.11 for ethanol and in equation 2.12 for iso-octane.

$$\Delta T_{Eth} = \frac{L_{Eth}}{9c_p} = 101.7°C \tag{2.11}$$

$$\Delta T_{C_8 H_{18}} = \frac{L_{C_8 H_{18}}}{14.7c_p} = 20.78°C \tag{2.12}$$

A reduction of over $100°C$ in the intake air temperature for ethanol explains the difficulties during cold start and the necessity of a direct injection system to fully benefit of the increase in charge density and lower temperatures at the beginning of the compression. Figure 2.1 shows the increase in charge density due to evaporative cooling. The horizontal axis shows the temperature before the evaporation. When the liquid fuel in a stoichiometric mixture of $150°C$ evaporates the density of the mixture is increased by 31% for ethanol and by only 5% for iso-octane.

The vapor pressures of gasoline and iso-octane are much higher than that of ethanol. The volatility of ethanol is low which contributes as well to its cold start problems. Low ethanol blends around E20 increase the vapor pressure over regular gasoline [75]. There is also a

local maximum in the latent heat of vaporization due to the formation of a positive azeotope.

Flame speed

For a premixed fuel/air mixture, the flame speed is defined as the speed with which the flame front propagates in a homogeneous mixture and the fuel is consumed. The heat release rate, dQ_b/dt, during combustion can be connected to the flame speed as written in equation 2.13, with $\dot{m}_u$ the consumption rate of air, ρ_u the unburned density and λ the air-to-fuel ratio.

$$\frac{dQ_b}{dt} = \frac{\dot{m}_u}{1 + \lambda \cdot AF_{ST}} \cdot H_u = \frac{\rho_u}{1 + \lambda \cdot AF_{ST}} S_T \cdot A_F \cdot Ex \cdot H_u \quad (2.13)$$

The flame front moves faster than the fuel is consumed, due to the expansion of the burned gases. An expansion factor, Ex, as a function of the density ratio and the mass fraction burned, x_b is defined in equation 2.14 to capture this behavior [76].

$$Ex = \frac{\rho_u/\rho_b}{(\rho_u/\rho_b - 1) \cdot x_b + 1} \quad (2.14)$$

The flame speed in equation 2.13 is the turbulent flame speed, S_T. The turbulence is considered in the turbulent flame speed and the flame area is that of a smooth flame. The turbulent flame speed is mainly governed by the turbulence in the cylinder and is about one order of magnitude higher than the laminar flame speed [76]. The laminar flame speed, S_L is a property of a combustible mixture and is typically measured in dedicated experiments. Modeling the turbulence intensity is required to obtain a relation between the laminar and the turbulent flame speed, as given in equation 2.15 [77], with u' the turbulence intensity, Re the Reynolds number and A_G, m_{ST} and n_{ST} parameters (although attempts to measure the turbulent flame speed directly have been made [78]).

$$\frac{S_T}{S_L} = 1 + A_G \cdot \left(\frac{u'}{S_L}\right)^{n_{ST}} \cdot Re_T^{m_{ST}} \quad (2.15)$$

The laminar flame speed of a combustible mixture depends on the pressure, temperature, air-to-fuel ratio and dilution and is, at a given condition, the speed with which the flame front propagates in a quiescent mixture. Many attempts at measuring the laminar flame speed have been undertaken for a wide variety of fuels and operating conditions. Figure 2.2 shows a summary of the laminar flame speed correlations and measurements for ethanol, available in literature, and compares those to two correlations for iso-octane at atmospheric pressure and temperatures 298 and 358 K.
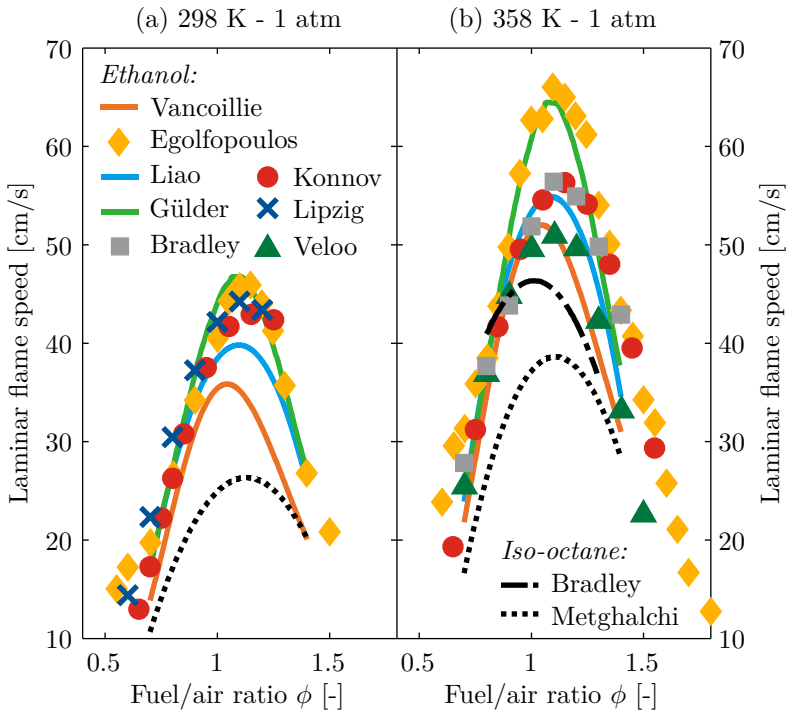

Figure 2.2: *Summary of laminar flame speed correlations and measurements for ethanol and iso-octane for (a) 298 and (b) 358 K at atmospheric pressure. Ethanol in colors: Vancoillie et al.[79], Egolfopoulos et al. [80], Liao et al. [81], Konnov et al. [82], Gülder [83], Lipzig et al. [84], Bradley et al. [85], Veloo et al. [86]. Iso-octane in black: Metghalchi et al. [87], Bradley et al. [88].*

For ethanol three correlations for laminar flame speeds can be found, typically as a function of the laminar flame speed at reference conditions and corrections for the influence of temperature and pressure. Gülder [83] proposed the first correlation for ethanol in the form usually applied for laminar flame speeds (without dilution) as shown in equation 2.16.

$$S_L = S_{L,ref} \left(\frac{T}{T_{ref}} \right)^\alpha \left(\frac{p}{p_{ref}} \right)^\beta \tag{2.16}$$

In this correlation (eq. 2.16) the temperature coefficient, α is constant and the reference flame speed, $S_{L,ref}$, is a second degree polynomial as a function of the air-to-fuel ratio. Liao et al. [81] extended the flame speed correlation with a linear dependency of the temperature coefficient on the air-to-fuel ratio (pressure coefficient, β, as in [83]). Vancoillie et al. [79] present a laminar flame speed correlation for ethanol combustion at engine-like operating conditions using chemical kinetics calculations. The correlation for the laminar flame speed is similar to equation 2.16 and is presented in equation 2.17. The correlation contains cross products for the pressure and the fuel-to-air ratio.

$$S_L = S_{L,ref}(\phi, p) \left(\frac{T}{T_{ref}} \right)^{\alpha(\phi,p)} \tag{2.17}$$

Next to the presented correlations, other researchers have published experimental results for ethanol/air mixtures at ambient pressure and different temperatures using either counter-flow measurements (Egolfopoulos et al. [80] and Veloo et al. [86]) or flat flame heat flux methods (Konnov et al. [82] and van Lipzig et al. [84]). Bradley et al. [85] (1 to 14 bar) and Beeckmann et al. [89] (10 bar) have reported experimental results for pressures higher than atmospheric using the closed vessel Schlieren technique.

For iso-octane the most common correlation is proposed by Metghalchi et al. [87] and is based on closed vessel measurements using equation 2.16. Huang et al. [90] reports primary reference fuel (PRF) flame speed measurements using a counter-flow configuration and Bradley et al. [88] presents results for iso-octane using a closed vessel. Jerzembeck et al. [91] reports flame speed measurements for iso-octane and PRFs at even higher pressures (10 to 25 bar).

It can be seen from figure 2.2 that ethanol has a significantly higher laminar flame speed compared to iso-octane, even though the results

presented in literature are not uniform. Higher flame speeds increase the rate of temperature and pressure build up and can therefore increase the indicated efficiency of the engine. Higher flame speeds raise the ignition limits and increase the resistance against dilution. This can be useful when dealing with high rates of exhaust gas recirculation [51] or very lean combustion. Even though the laminar flame speed for ethanol is higher than that for iso-octane, it must be noted that the turbulent flame speed is dominant for the combustion in an ICE. Differences in turbulent intensity can more than offset the differences in the laminar flame speed. The laminar flame speed has a high positive temperature coefficient (compared to the lower negative coefficient for pressure). The lower burning temperatures in ethanol operated engines reduce the laminar flame speed and can cancel out the original advantage [21]. The peak flame speed for both ethanol and PRFs occur in the slightly rich operating area with ethanol peaking a little richer than the PRFs, possibly due to the oxygen content in ethanol [80].

Early experiments with ethanol/iso-octane blends (up to 20 vol% ethanol) show that ethanol addition increases the laminar flame speed [92]. More recent work by Broustail et al. [93] examines laminar flame speeds for ethanol/iso-octane blends and proposes a correlation to determine the flame speed of any blending fraction, $S_{L,blend}$. The correlation is given in equation 2.18 with the resulting flame speed being an exponential function of the blending fraction, f_{va}.

$$S_{L,blend} = S_{L,\mathrm{C_8H_{18}}} \left(\frac{S_{L,\mathrm{C_2H_5OH}}}{S_{L,\mathrm{C_8H_{18}}}} \right)^{f_{va}} \tag{2.18}$$

Next to a higher laminar flame speed, ethanol has a lower adiabatic flame temperature. The flame thickness of an ethanol flame is smaller than that of iso-octane for the rich and slightly lean mixtures, but a higher flame thickness for leaner mixtures [92].

2.2   Test engine

The research engine used for this work is a single cylinder 4-stroke spark ignition engine manufactured by Swissauto Wenko AG with the specifications given in table 2.2. Originally the engine burns gasoline, which is injected in the intake manifold. With these settings the engine produces 13.67 kW at 6000 rpm and 22.31 Nm at 5000 rpm.

Table 2.2: *Test Engine Data.*

Displaced volume	250 cc
Stroke	56.5 mm
Bore	75 mm
Connecting rod	95 mm
Compression ratio	12.5:1
Number of valves	4
Number of cylinders	1
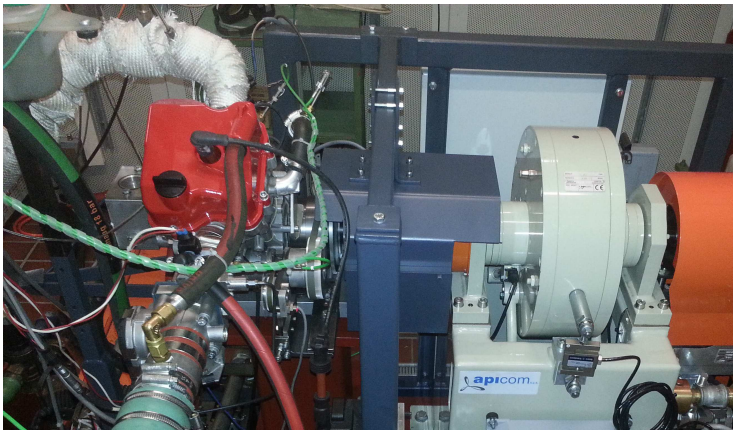
Figure 2.3: *Picture of the engine test bench as built up at LAV.*

The test engine is connected to an eddy current brake via a curved teeth coupling. The brake of the type APIcom FP75 is used to control the speed of the engine and record the load. A picture of the setup used for all experiments can be seen in figure 2.3. The geometry of the combustion chamber can be seen in figure 2.4. The figure shows the view on the symmetry plane containing the intake and exhaust ports. The engine has a pent roof with the spark plug located in between the valves. The spark plug is located slightly off-center because the intake valves are larger than the exhaust valves. The piston has pockets for the valves (not visible in the figure) and a compression dome in line with the pent roof.
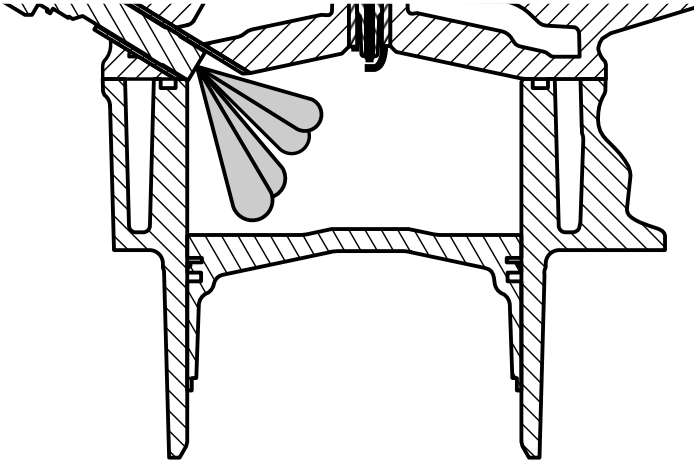
Figure 2.4: *Combustion chamber geometry for the symmetry plane containing the intake and exhaust ports. The position of the injector in the DI system is shown on the top left, in between the intake valves. The direction of the spray is included in gray.*

2.3 Injection modes

The original engine uses a port fuel injection system with an injection pressure of 4 bar. Additionally, a high pressure direct injection system is fitted to the engine in order to avoid problems during cold start with ethanol and to benefit from its cooling effect during steady state operation. The location of the injector within the engine head as well as the direction of the spray beams can be seen in figure 2.4. The spray is aimed towards the piston in order to minimize wall wetting of the liner on the opposite exhaust side. A Bosch type HDEV5 six-hole injector is used and the injector is positioned between the intake valves and the fuel is injected at 110 bar.

The idealized injection rate profiles for both PFI and DI can be seen, relative to the valve lift profiles, in figure 2.5. The start of injection for the direct injection system is set at the timing of exhaust valve closing, to avoid losing fuel directly into the exhaust and maximize the time available for mixing and evaporation. Additionally during this time the intake valves are open and the incoming air interacts with the fuel
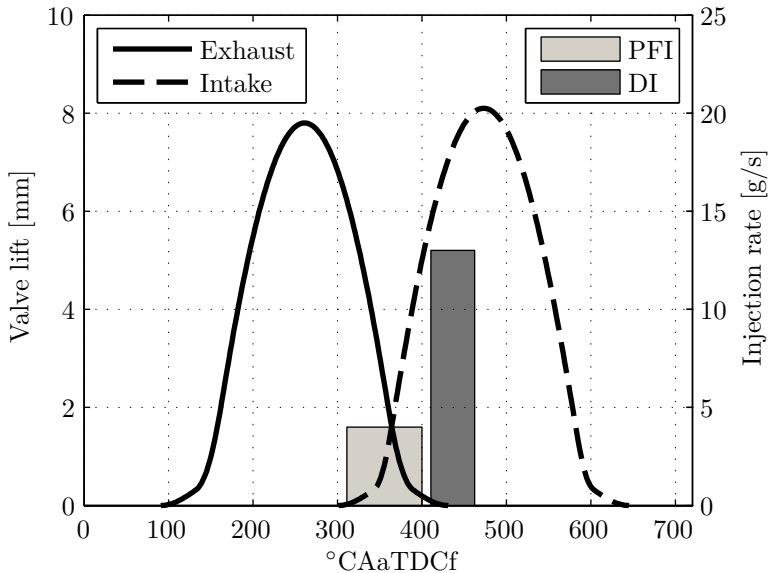
Figure 2.5: *Valve lift and typical idealized injection profiles for DI and PFI. DI for ethanol and PFI for iso-octane.*

spray. The PFI injector is located well before the intake valves and the end of injection in this mode is fixed to 320°CAbTDCf for all operating points. The injection rates in figure 2.5 are for iso-octane in PFI and ethanol in DI mode for the same load and speed. The injection rate for DI is higher and therefore shorter. However the total area under the DI profile is larger than that for PFI, due to the lower energy density of ethanol. The PFI system uses a Bosch FP100 fuel pump, the DI system a three cylinder radial piston pump, whose pumping frequency equals the injection frequency. The power for both pumps is supplied externally.

2.4 Test bench design and measurement signals

All the required equipment for this investigation of knock is installed on the engine test bench. A summary of all the sensors, measured signal

Table 2.3: *Measured signals, sensor equipment and sample frequency.*

Signal	Sensor equipment	Sample rate
Intake pressure	Kistler 4075A	0.2 °CA
Exhaust pressure	Kistler 4049A	0.2 °CA
In-cylinder pressure	Kistler 6052	0.2 °CA
Fuel pressure	Kistler 4065A	0.2 °CA
Speed	Apicom brake speed sensor	1 s
Torque	Apicom brake load cell	0.2 °CA
Air/Fuel ratio	λ-probe Bosch LSU 4.9	0.2 °CA
Injection/Ignition	Bosch ECU MS4 Sport	0.2 °CA
Fuel consumption	Coriolis mass flow meter E+H Cubemass	0.2 °CA

Temperatures:
• Intake
  − Before intake
  − After throttle
  − Before valves
• Exhaust
  − Before TWC
  − After TWC
• Cooling water
  − Before engine
  − After engine
	Thermocouple	1 s

and corresponding sampling rates is given in table 2.3. A schematic of the test bench setup including the main sensor and component positions is shown in figure 2.6.

Piezo-resistive pressure sensors are used to record the intake (Kistler 4075A) and exhaust (water-cooled Kistler 4049A) absolute pressure profiles. The in-cylinder pressure trace is measured using the piezo-electric Kistler 6052 pressure sensor, which is located between the intake and exhaust valves on the chain side of the cylinder head. The fuel pressure in the direct injection line is recorded with a Kistler 4065A. The different pressure profiles as well as the piston position are recorded at a rate of 0.2°CA in order to allow an accurate thermodynamic analysis of the engine cycle.

A Bosch MS4 Sport engine control unit (ECU) is used to trigger the injection and ignition events. The stoichiometry of the mixture is
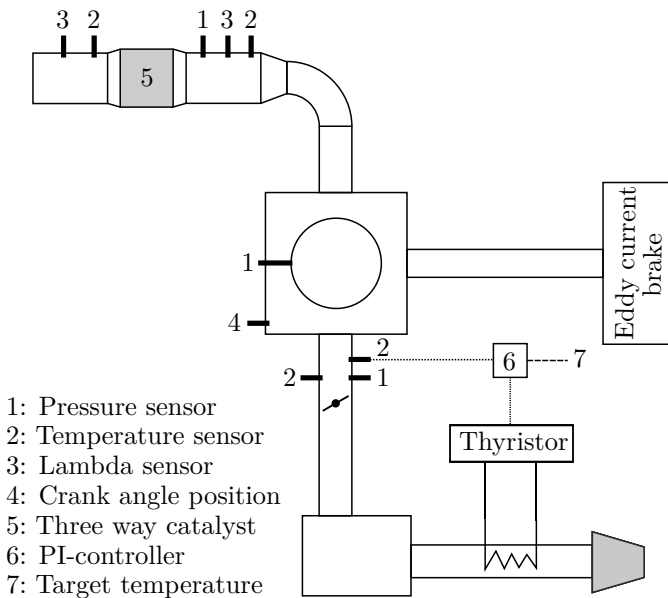
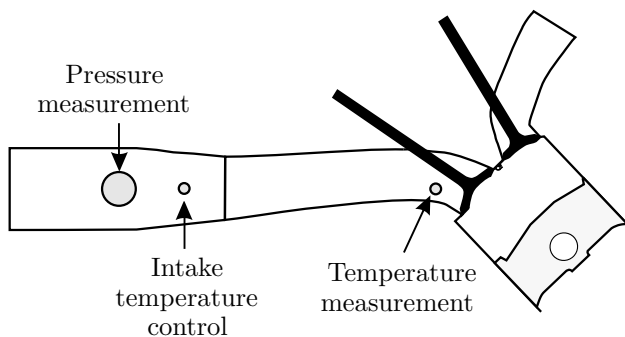**Figure 2.6:** *Schematics of the test bench and main sensor positions.*

1: Pressure sensor
2: Temperature sensor
3: Lambda sensor
4: Crank angle position
5: Three way catalyst
6: PI-controller
7: Target temperature

Figure 2.7: *Location of the temperature and pressure sensors in the intake path.*

controlled in closed loop by a Bosch LSU 4.9 λ-probe. A second λ-sensor is installed further downstream the exhaust pipe and is used for recording. A muffler reduces the exhaust noise and a three way catalyst (TWC) reduces the pollutant exhaust emissions. A coriolis mass flow meter is used to measure the fuel consumption. The fuel consumption data is recorded at the same rate as the pressure profiles, but the data are averaged since no transient behavior can or should be observed.

Temperature measurements are taken using thermocouples along the intake and exhaust paths as well as in the cooling water circuit. A 1D engine simulation model is built up based on the test engine setup. The accuracy of the model calibration relies heavily on the availability of the temperature profile within the intake and exhaust piping. A more detailed illustration of location of the temperature and pressure sensors in the intake manifold can be seen in figure 2.7.

In order to control the temperature of the incoming air, a heater and air-box are installed in the intake path. The resistive heater is supplied with singe phase 400V and has a maximum power of 2.5 kW, reaching temperatures up to 120°C. The control loop for the temperature control, using a PI-controller and a thyristor to set the temperature after the throttle body, is shown in figure 2.6.

2.5 Operating points

Measurements are carried out at a large set of operating conditions in order to obtain an extensive data set of different knock intensities. A list of all the operating points for both ethanol and iso-octane is given in table 2.4. Spark timing variations are carried out at different engine speeds and intake temperatures ranging from late non-knocking conditions up to early spark timing and strong knock. At ambient intake conditions no knock is observed for ethanol, even with very early spark timings. For these operating points no measurements are carried out. All measurements are conducted at wide open throttle stoichiometric air-to-fuel ratios. The engine oil and cooling water are brought up to their operating temperatures and only steady-state conditions are recorded. For each operating point 288 consecutive cycles are recorded. The injection strategy is as shown in figure 2.5 with PFI for iso-octane and DI for ethanol. The engine was designed by the manufacturer for operation at high speeds. Below 3000 rpm the torque of the engine drops and large cycle-to-cycle variations lead to unstable operation.

Table 2.4: *Operating conditions for the experiments.*

Speed [rpm]	T_{in} [°C]	Spark advance [°CAbTDCf]	
		Ethanol	*Isooctane*
3000	35	-	41.25 - 54.75
	80	45.00 - 60.00	36.75 - 50.25
	100	35.25 - 60.00	35.25 - 48.00
	120	30.00 - 50.25	30.75 - 42.00
4000	35	-	39.00 - 52.50
	80	33.75 - 44.25	25.50 - 39.00
	100	30.00 - 43.50	26.25 - 37.50
	120	33.75 - 47.25	26.25 - 37.50
4500	35	-	33.00 - 46.50
	80	35.25 - 53.25	32.25 - 47.25
	100	33.75 - 44.25	29.25 - 42.75
	120	31.00 - 41.25	24.00 - 37.50
5000	35	-	38.25 - 51.75
	80	33.75 - 41.25	24.75 - 38.25
	100	33.75 - 43.50	26.25 - 37.50
	120	33.75 - 41.25	27.00 - 36.00
5500	35	-	46.50 - 60.00
	80	30.00 - 47.25	32.25 - 45.75
	100	30.00 - 41.25	27.00 - 40.50
	120	28.75 - 33.75	24.75 - 36.00

3 Thermodynamic analysis of the combustion process

For the evaluation of the measurements described in chapter 2 a thermodynamic analysis of the combustion process is carried out. Based on the measurement data, the heat release rate and the two zone temperatures for both the mean cycle (averaged over one operating point) and each of the single cycles can be calculated. The accuracy of these calculations is of crucial importance for the further study of knock, because of the sensitivity to the temperature of the unburned gases.

This chapter introduces the software that is selected for the calculations and lists the assumptions and models that are used. The difference in the calculations for the mean engine cycle and the single cycles are pointed out and a sensitivity analysis for the model parameters is presented.

3.1 1D Simulation model in GT-Power

Based on the engine measurements a 1D simulation model in the software GT-Power, a part of the GT-Suite[1] package developed by Gamma Technologies, is built up. This model also forms the basis for the thermodynamic analysis of the combustion process. A reduced model ranging from the position of the intake pressure sensor to the exhaust pressure is used in a so-called three pressure analysis. The measured intake and exhaust pressure traces for each measurement are set as boundary conditions for the calculation. The geometry of the combustion chamber, the intake and exhaust piping, the cylinder head as well

---

[1]www.gtisoft.com

as the valve lift profiles and the flow coefficients are contained in the model. Two calculations are carried out in each iteration: a forward and a backward run. During the backward calculation only the high pressure phase between IVC and EVO is considered. The heat release rate is calculated using the measured cylinder pressure as an input. This heat release rate is used as an input for the forward calculation, which considers the complete engine cycle including the gas exchange phase. The forward calculation has the composition at IVC and the in-cylinder pressure trace as results. These conditions at IVC are again used as an input for the next backward run. When the simulated temperatures, the in-cylinder pressure profile and the mass flow rate match with the measured values, convergence is reached and the calculation is terminated. The main advantage of this method over conventional calculation methods is that it includes a 1D simulation of the gas exchange phase and more accurate values for the conditions at IVC as well as the residual gas fraction are obtained. Figure 3.1 shows an illustration of the algorithm of the thermodynamic analysis of the engine cycle.

3.2 Assumptions and models

Whereas the geometry of the engine and the test bench is known, the heat transfer and the component temperatures must be modeled and calculated. The heat transfer coefficient from the combustion chamber gases to the cylinder walls (i.e. cylinder head, piston, liner and valves) is modeled using the Woschni [94] equation. In order to calculate the wall temperatures, the heat transfer coefficient on the outside of the components, at the interaction with the coolant or the oil, is modeled as well. Four interfaces are defined: cylinder head - coolant, liner - coolant, piston - oil and liner - oil. The values of the heat transfer coefficients at these interfaces are estimated. The speed of the pump driving the coolant circuit is not related to the engine speed, leading to a relatively constant coolant mass flow rate. A constant value for the coolant heat transfer coefficients can therefore be assumed. The oil and coolant temperatures are measurement results and with the estimated heat transfer coefficients on both the inside and the outside of the components, the temperatures of the cylinder walls as well as the heat losses can be calculated. In a similar way, using convection and conduction models, the heat transfer in the intake and the exhaust path is modeled.
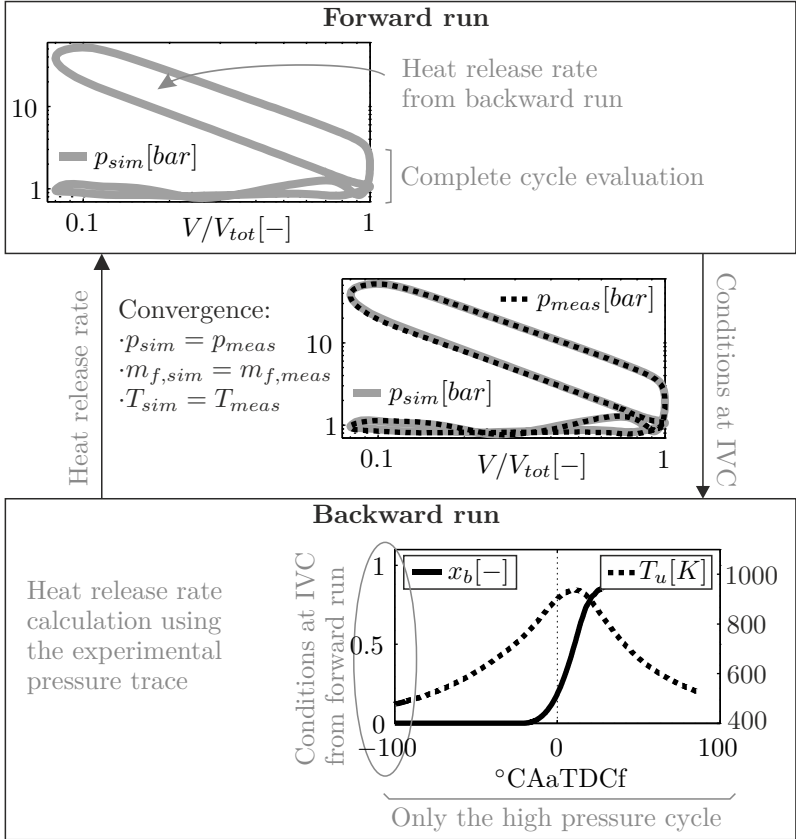
Figure 3.1: *Summary of the algorithm for the calculation of the heat release rate and the two zone temperatures in GT-Power.*

The injection of ethanol occurs during the intake process. The evaporation of the fuel has an important impact on the temperature of the gases in the cylinder, as illustrated in section 2.1. The injection and evaporation for the DI mode must thus be modeled in more detail. In order to model the injection, the injection rate profile as in figure 2.5 is imposed. The evaporation of the fuel after injection is however unknown. The evaporation rate is modeled using an equation proposed in the GT-Power software based on the 50 % evaporation time, CA_{50}. The evaporation rate increases with temperature and speed and is shown in
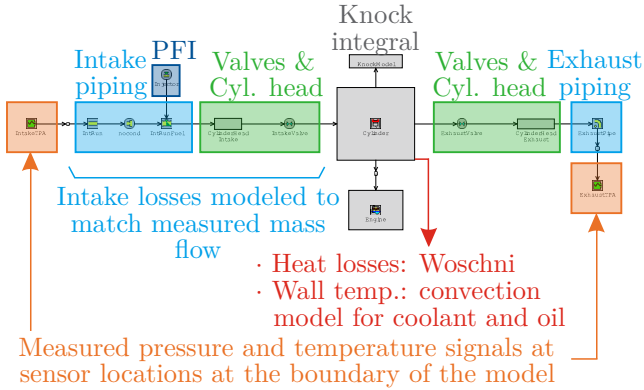
Figure 3.2: *Outline of the 1D GT-Power model for the PFI injection mode.*

equation 3.1.

$$\dot{m}_{evap} = \frac{4.16 \cdot 4000rpm}{CA_{50}} \left(\frac{T}{600K} \right) \left(\frac{N}{4000rpm} \right) \qquad (3.1)$$

An overview of the 1D model in GT-Power and the used assumptions can be seen in figure 3.2.

3.3 Single and mean cycles

For each of the measurement operating points 288 consecutive cycles are recorded. Due to the cycle-to-cycle variations, all of these single cycles are different. The average of all these single cycle is referred to as the mean cycle for that operating point. The parameters of the GT-Power model, as described in the previous sections, are calibrated against the mean cycles of all operating points in the measurement campaign. All of the models require parameter values that are valid independent of the operating point. The parameters are calibrated in such a way that the calculations for all the mean engine cycles converge. Table 3.1 lists the final parameter values for the external heat transfer coefficients and the evaporation rate. The thermodynamic analysis is then carried out for both the mean engine cycles as well as all the single

cycles. Between each single cycle the gas exchange phase calculation is carried out thus including the cyclic differences in volumetric efficiency.

Table 3.1: *Values of parameters for the GT-Power model.*

	Parameter	Unit	Value
Heat transfer coefficient	Coolant - Head		3500
	Coolant - Liner		3500
	Oil - Piston	W/m^2K	3000
	Oil - Liner		3000
	Intake port		1000
	Exhaust port		1000
	CA_{50}	$^\circ$CA	10

Before the heat release rate calculation, the measured pressure traces are filtered using a low-pass filter with a cut-off frequency of 5 kHz. In this way noise from the pressure sensor, vibrations caused by valve events and pressure oscillations as a result of auto-ignition in the end-gas are eliminated. The algorithm for knock detection, based on the heat release rate calculation and the oscillations of the in-cylinder pressure, is described in chapter 4.

3.4 Parameter value sensitivity in the GT-Power model

The accuracy of the results of the thermodynamic analysis is of crucial importance for the further knock detection and modeling study. Knock models often rely on correlations for the auto-ignition delay time. These are typically Arrhenius-type equations with a high sensitivity on temperature. A sensitivity analysis of the estimated parameters of table 3.1 on the peak unburned temperature, $T_{u,peak}$, and the temperature at IVC, T_{IVC} is carried out and the results for a representative operating point are shown in figure 3.3. The sensitivity analysis assesses the impact of an incorrect estimate of these unknown parameters.

Figure 3.3 shows $T_{u,peak}$ and T_{IVC} for the reference case denoted by the black vertical line and the results when a parameter is varied over a wide range of values, while keeping all other parameters at the reference value. An increase of the heat transfer coefficients promotes higher heat losses and leads to overall lower temperatures. The oil cooling on the
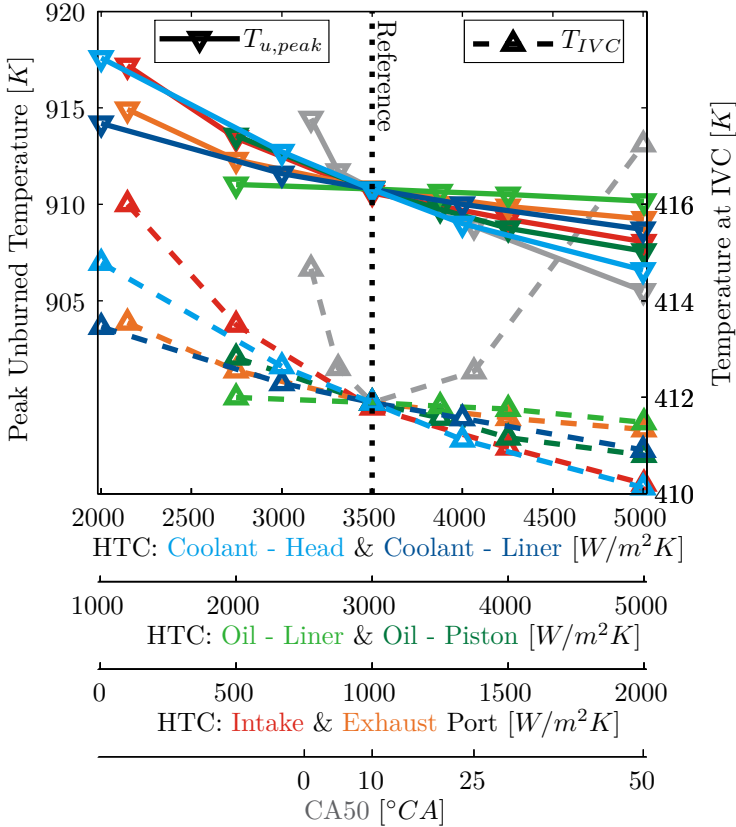
Figure 3.3: *Sensitivity of the GT-Power model parameters (different x-axes) - heat transfer coefficients (HTC) and evaporation profile (CA_{50}) - on the peak unburned temperature (left y-axis, full line, $\triangledown$) and the temperature at IVC (right y-axis, dashed line, $\triangle$) for a representative operating point: 4000rpm, T_{in}=100° C, 36.75° CA SA, Ethanol, WOT, $\lambda = 1$.*

liner has the lowest effect on the investigated temperatures. The effect of oil cooling on the piston accounts for a maximum deviation of 0.9°C on T_{IVC} and 3.2 °C on $T_{u,peak}$ for the investigated parameter range. The heat transfer coefficients of the coolant have a stronger influence on temperature than those for the oil. The heat losses to the cylinder head are more sensitive than those through the liner. Maximum deviations from the reference case of 6.8°C for $T_{u,peak}$ and 2.9°C for T_{IVC} are observed for the coolant - head interface. The heat transfer coefficient in the intake port has a higher influence on the temperatures in the cylinder compared to the exhaust port. The heat transfer in the intake affects the temperature of the fresh charge and thus also the volumetric efficiency. A strong reduction of the heat transfer coefficient in the intake, which corresponds to neglecting the effect of the coolant on the piping in the cylinder head, leads to a maximum increase in $T_{u,peak}$ of 6.4°C and 4.1°C in T_{IVC}.

The influence of the fuel evaporation rate on the investigated temperature is not uniform. An increase in the evaporation rate and thus a decrease of CA_{50} leads to an increase in both $T_{u,peak}$ and T_{IVC}. As discussed extensively in chapter 2 the evaporation of the fuel cools down the mixture. With a low value for CA_{50} the evaporation is finished much before IVC and the hot walls heat up the mixture, leading to an increase in T_{IVC} and therefore also in $T_{u,peak}$. For a high value of CA_{50} not all the fuel is evaporated at IVC, leading to an increase in T_{IVC}. The evaporation continues during the compression stroke leading to a decrease in $T_{u,peak}$.

4 Knock detection methods

Knocking combustion is characterized by high frequency pressure oscillations resulting from pressures waves traveling through the combustion chamber after auto-ignition of the unburned mixture. For the experimental study of knock in spark ignition engines, solid knock detection criteria are needed. This chapter first gives an overview of the state of the art and secondly of the definition of the knock detection criterion used in this work. The knock criterion differentiates between the detection of knocking cycles and the determination of the timing for the onset of knock. In a last section the difference between single cycles and the mean cycle for a single operating point is discussed.

4.1 State of the art

Auto-ignition of the unburned mixture in the end-gas leading to knocking combustion occurs when the temperature and pressure in the unburned zone in front of the flame are sufficiently high and enough time is available to cover the auto-ignition delay time. Knock is therefore often related with high compression ratios, high charge densities (e.g. caused by turbo charging) or early spark timings. The auto-ignition is typically initiated at so-called hot spots in the combustion chamber. Inhomogeneities in the temperature and mixture distribution cause favorable auto-ignition spots, where the reaction is initiated first. The chemical reaction rates during auto-ignition are very high, causing the typical pressure oscillations. The maximum amplitude of the oscillations is related to the initial boundary conditions at the moment of auto-ignition and the consequent reaction rate [95]. The pressure waves can cause a reduction of the auto-ignition delay time in the region nearby, resulting in multiple auto-ignition spots, which can lead to a detonation.

The waves propagate through the combustion chamber at the speed of sound until they are reflected at the walls. The frequency of the oscillations is therefore closely related to the combustion chamber geometry. Equation 4.1 relates the frequency, f, of the pressure oscillations to the bore, B, the speed of sound, c and the wave number, ν [96].

$$f = \frac{c}{\nu \cdot B} \tag{4.1}$$

The pressure amplitude recorded with a pressure sensor is a local measure. During knocking combustion, the pressure recorded with the in-cylinder pressure sensor is no longer representative for the entire combustion chamber. Resonating pressure waves of various frequencies travel through the combustion chamber and the recorded amplitude is local.

Knock detection can be done using:

- A vibration sensor mounted on the outside of the engine, typically used in commercial engines to retard the spark timing when high-frequency vibrations are measured.

- Optical access to see the location of the auto-ignition as for example in [97], where the knock locations are detected using multiple cylinder pressure sensors and optical fiber probes. The relation between the local hot spots and the turbulence flow field and local mixture gradients is discussed. Higher turbulence and better mixture formation reduce the knocking tendency of an engine.

- Acoustic sensor to determine audible knock as for example in [98], where the frequency content of an acoustic sensor is compared that of the in-cylinder pressure trace for knocking cycles. Depending on the cylinder geometry and which resonant mode is excited, knock is audible or not.

- The pressure signal trace using a piezo-electric in-cylinder pressure sensor, as typically installed on research engine test benches.

For a single operating point the cycle-to-cycle variations cause some cycles to knock and others to proceed with normal combustion. The intensity of knock between these cycles varies strongly as well. A knock detection method proposed in [99] uses the standard deviation of the peak pressure or the maximum rate of pressure rise. The coefficient

of variation (CoV) on the indicated mean effective pressure (IMEP) however does not vary strongly between knocking and non-knocking operating points.

4.1.1 Knock indices

Many different methods for knock detection in a SI engine have been proposed. Most of them try to quantify the knocking events through the evaluation of a certain knock index that increases from regular combustion over the onset of knock to strongly knocking conditions. Typically a threshold value is used as the knock limit, thus distinguishing knocking cycles from regular cycles. However the transition between the different regimes is continuous. A difference can be made between the knock limit (KL) and the damage limit (DL) [97]. The damage limit is the severity of knock at which the engine starts to suffer damage from the pressure oscillations. This limit depends on the engine manufacturer and is difficult to determine in advance.

Without optical access to the combustion chamber, knock detection using the in-cylinder pressure trace is the most reliable method. Using the in-cylinder pressure sensor, the knock indices can be based on either the pressure signal itself or the heat release rate. The heat release rate is the result of calculations with the pressure signal as an input. Both signals are therefore related; in this description they are however treated separately.

Based on the in-cylinder pressure signal

Knock is characterized by the typical pressure oscillations caused by the auto-ignition of the unburned mixture in front of the flame. These oscillations have high frequencies compared to the frequency content of normal combustion. Often a high-pass or band-pass filter in the region of about $4 - 25kHz$ is applied to the in-cylinder pressure signal, obtaining just the knock induced oscillations in the signal p_{filt} or $\tilde{p}$. Applying equation 4.1 to the engine in this work yields about 7 kHz for the first oscillation mode with an air temperature of 2000 K.

The most straight-forward approach is to select the maximum amplitude of the pressure oscillations (MAPO) as a measure for knock intensity (equation 4.2) [100].

$$MAPO = max\left(|\tilde{p}|\right) \tag{4.2}$$

Next to the maximum amplitude, the integral of the modulus of pressure oscillations (IMPO) can be used (equation 4.3). This index considers both the amplitude and the length of the oscillations. The parameter ζ denotes the crank angle interval over which the oscillations are considered.

$$IMPO = \int_{\theta_0}^{\theta_0+\zeta} |\tilde{p}| d\theta \tag{4.3}$$

In a similar way the integral of the modulus of the pressure gradient (IMPG) can be used as a knock indicator as well (equation 4.4).

$$IMPG = \int_{\theta_0}^{\theta_0+\zeta} \left|\frac{d\tilde{p}}{d\theta}\right| d\theta \tag{4.4}$$

The method used by Wayne et al. [101] is the value of the third derivative of the pressure signal. The crank angle for the onset of knock is determined as the first point where the third derivative has a value lower than -70 kPa/°CA. The knock intensity, in this case, is determined by the amount of energy left in the cylinder (as in equation 4.5).

$$KI_{xb} = (1 - x_b) \cdot 100 \tag{4.5}$$

In [102] the signal energy of the pressure oscillations (SEPO) or the resonance energy, E_{res} (equation 4.6), is used to compute an experimental knock indicator.

$$SEPO = E_{res} = \int_{\theta_0}^{\theta_0+\zeta} \tilde{p}^2 d\theta \tag{4.6}$$

The low pass filtered pressure curve is split into a motored and combustion pressure signal. The knock index, I_2, is then calculated as the logarithm of the ratio of the signal energy of the motored, E_{mot} and the knocking, E_{res} pressure as in equation 4.7, with S as a scaling factor.

$$I_2 = log_{10}\left[S\left(\frac{E_{res}}{E_{mot}}\right)\right] \tag{4.7}$$

Another way is to integrate the power density spectrum of the Fourier transform over a chosen frequency band [98]. As an alternative to the Fourier transform also the discrete wavelet transform can be used to determine knock [103].

No matter what knock index is used, it should be independent of the operating point. In [104] it is found that the MAPO and IMPO values for non-knocking cycles increase with speed. It is therefore proposed to reference the MAPO or IMPO values to the non-knocking value. The relative value increases in this case with higher spark advance values.

Based on the heat release rate

A knock detection method or knock index can also be defined using the heat release rate profile. In this case the heat release rate for each single cycle is evaluated. A distinction needs to be made between the heat release rate based on the filtered or the unfiltered in-cylinder pressure. In the latter case the heat release rate contains the frequencies of the pressure oscillations. The heat release rate during knocking combustion can even become negative losing its physical meaning. The pressure oscillations are a result of pressure waves in the cylinder. In this case the pressure is not uniform throughout the combustion chamber and the heat release rate does not describe the actual release of heat.

A high pass filter can then be applied to the previously unfiltered heat release rate and knock indices, similar to the ones defined for the in-cylinder pressure signal, can be computed. In [105], for example, the high frequency content of the heat release rate, $d\tilde{Q}^2/d\theta$, is evaluated and a value similar to SEPO is computed as shown in equation 4.8. In this case it can be called the signal energy of the heat release rate oscillations (SEHRRO).

$$SEHRRO = \int_{\theta_0}^{\theta_0+\zeta} \frac{d\tilde{Q}^2}{d\theta} d\theta \qquad (4.8)$$

Corti et al. [106] find that the pressure oscillations are the 'mechanical signature' of the knocking combustion. The underlying cause of the pressure oscillations is the heat release in front of the mean flame front. Non-knocking cycles are approximated using two Wiebe functions. When large oscillations in the heat release rate exist, a Wiebe

function is fitted to model the knocking combustion. The knock intensity is related to either the maximum value or the integral of the third Wiebe function.

Also in [107] it is found that the high frequency content is characteristic for knocking combustion. It is however the result of the rapid heat release and dependent on cylinder geometry. The authors propose a new knock detection method based on the frequency content of the unfiltered heat release rate of the single cycles trying to identify the knocking heat release causing knocking combustion. The frequency band between 30 and 200 osc/cycle is found to have a good indication of knock intensity and is used as the knock detection method.

4.1.2   Onset of knock detection

Often omitted in the definition of a knock criterion is the timing for the onset of knock. For knock modeling purposes however it is important to know exactly when during the cycle the auto-ignition is initiated.

The onset of knock can be defined as the first time a certain threshold value is exceeded. For example the first time the $MAPO$ value crosses 1 bar or, as mentioned earlier, the first time the third derivative of the pressure trace is lower than -70 kPa/$°$CA. Another possibility is to use the maximum value of a knock index, for example the timing of the maximum pressure peak, i.e. the timing of $MAPO$. In [105] the onset of knock is determined by the ratio of the SEPO before and after the onset of knock.

The overview of the literature on knock detection methods show, that many authors have used many different approaches to distinguish a knocking cycle from a regular cycle. The selection of the knock index and the detection of a knocking cycle as well as the decision on the definition of the timing for the onset of knock should be determined by the purpose to which it should be used.

4.2   Definition of a knock criterion

In order to study knock in a systematic way, a clear and precise definition of knocking conditions is needed. This section lays out the definitions used further in this work. First the definition of a knocking cycle is given, then the timing for the onset of knock is described. In
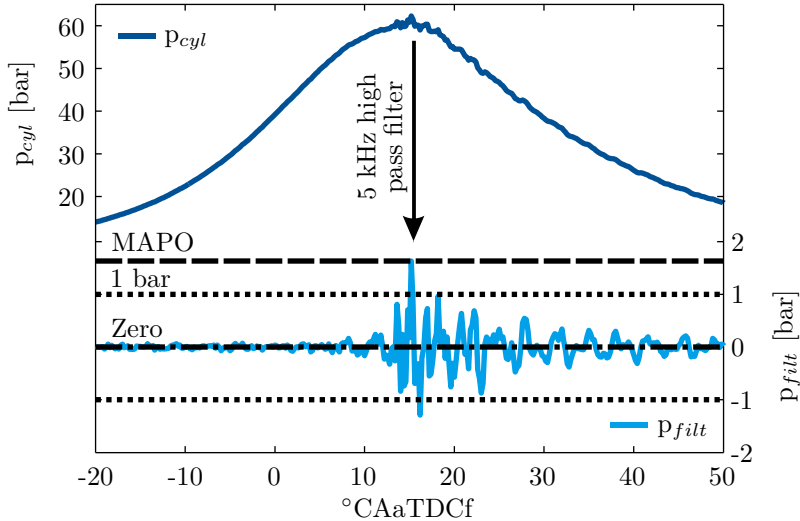
Figure 4.1: *In-cylinder pressure trace and high pass filtered signal for an example cycle at operating point 4000 rpm, T_{in}=120° C, 33.00° CA SA, iso-octane.*

a last part the difference between the single and overall mean cycle is given.

4.2.1 Knock detection

Typical for knocking combustion are the pressure oscillations induced by the very fast chemical reactions that occur, when the unburned mixture auto-ignites. These oscillations can be captured with an in-cylinder pressure sensor. When applying a high pass filter to the data, only the high frequency oscillations remain. Figure 4.1 shows the in-cylinder pressure profile for an example measured cycle. The data recorded with the pressure sensor are filtered using a 5kHz high pass filter. The values for 1 bar and MAPO are indicated.

Knock is a stochastic process. Each individual cycle for the same operating point has a different combustion progress and the knock intensity changes from cycle to cycle. Figure 4.2 shows the MAPO values of each single cycle for three operating points at the same speed and intake temperature, but with different spark timings (early, intermediate

and late). The operating point with early spark timing has overall high
MAPO values and almost all cycles knock. The oscillation peaks reach
up to 20 bar and this operating point should be avoided for continuous
operation. The operating point with a spark advance of 33°CA has
some high values of the MAPO index, but most cycles do not knock.
In the operating point with late spark timing all MAPO values are low,
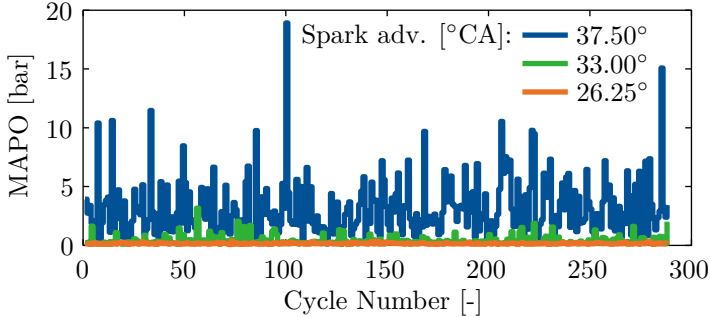corresponding to an operating point with regular combustion.

Figure 4.2: *MAPO values for all cycles for three different spark tim-
ings: late, medium and early at 4000 rpm, T_{in}=120° C, iso-octane.*

The MAPO value at the later spark timing is however not zero. Vi-
brations of the engine block and noise on the measurement signal cause
high frequency perturbations on the measurement signal. The MAPO
value for late spark timings is dependent on the speed and load operat-
ing point of the engine. The value of the knock index used to identify a
knocking cycle should be independent of the operating conditions [104].
To this extent the MAPO value at late, non-knocking, spark timings
is taken as a reference, $MAPO_{ref}$. Figure 4.3 shows how the MAPO
values are speed and load dependent. In each operating point spe-
cific vibrations can cause additional noise on the signal. Especially to
distinguish between knocking and non-knocking conditions this effect
has an influence. Therefore a knock index relative to the non-knocking
conditions can be defined. The knock index, $MAPO_{rel}$, then represents
the maximum amplitude of the pressure oscillations relative to the vi-
brations at non-knocking conditions, as shown in equation 4.9. Using
this knock index only oscillations caused by auto-ignition are detected.

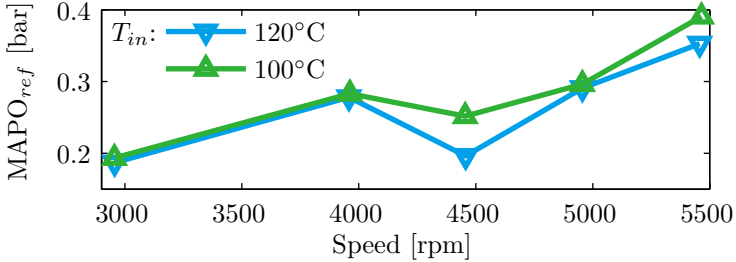$$MAPO_{rel} = \frac{MAPO}{MAPO_{ref}} \tag{4.9}$$

Figure 4.3: *Average MAPO values at late timings ($MAPO_{ref}$) for different speeds and intake temperatures.*

In order to be able to distinguish between a knocking and a non-knocking cycle, a threshold value for the knock index is required. The transition from a regular cycle to a knocking cycle is however not discrete. The flame propagation changes from cycle to cycle and it is e.g. possible that auto-ignition occurs in a region where only a small fraction of the fuel is consumed through the process. Even though auto-ignition occurs, the pressure oscillations are very small and in the heat release rate profile no clear auto-ignition can be distinguished. It is difficult to detect such a cycle as a knocking cycle. However these cycles do not damage the engine and should not necessarily be avoided. After thorough inspection of the data, a value of 4 is selected as the threshold value for the knock index, $MAPO_{rel}$, and the knock criterion for this work is given in equation 4.10.

$$MAPO_{rel} > 4 \tag{4.10}$$

Strong pressure oscillations due to knock and their vibrations damage the engine. They are therefore used as the criterion for the detection of a knocking cycle. Knock detection based on the frequency content of the heat release rate has proven unreliable for the available data.

Figure 4.4 shows, as an example, the filtered pressure profiles of 4 cycles within the same operating point with different $MAPO_{rel}$ values. For the gray curve the maximum amplitude is almost the same as for the operating point at late timing. There is no knock for this cycle. The blue curve has an increased amplitude of the oscillations during the combustion. The orange curve represents a knocking cycle for the criterion in equation 4.10. There is a clear difference between the oscillations before and after knock. The green curve shows the pressure oscillations for a clearly knocking cycle.
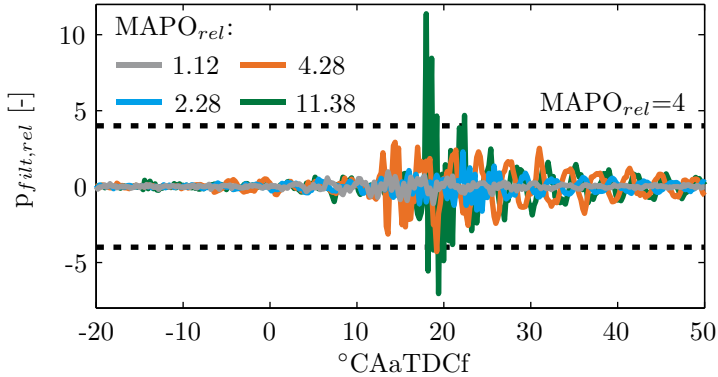
Figure 4.4: *Filtered pressure traces for four cycles with different MAPO$_{rel}$ values for the same operating point at 4000 rpm, T_{in}=120° C, 33.00° CA SA, iso-octane.*

4.2.2 Onset of knock timing

With the definition of the detection algorithm of a knocking cycle, it is now of interest to know when exactly in the knocking cycle the auto-ignition occurs. For the development of an accurate knock model, the timing for the onset of knock or the start of knock (SOK) must be determined. Based on the pressure oscillations, criteria for the start of knock can be defined (as presented in section 4.1.2) for the first crossing of the critical value, SOK p$_{crit}$ or at the timing of the maximum pressure oscillation, SOK p$_{max}$. However when looking at the corresponding heat release rate profile, it can be seen that the auto-ignition takes place before the start of the pressure oscillations. The upper graph of figure 4.5 shows the heat release rate and the pressure oscillations for a strongly knocking cycle on the same axis as well as three possible criteria for the onset of knock timing. It is obvious from the figure that the auto-ignition takes place before the start of the pressure oscillations. For a strongly knocking cycle there is an increase in the heat release rate at the timing of auto-ignition. For a cycle at borderline knock this increase is not necessarily observed, as shown on the bottom graph of the figure. A deviation in the heat release profile can however be seen. The timing for the onset of knock is therefore defined as the local maxima in the second derivative of the mass fraction burned.

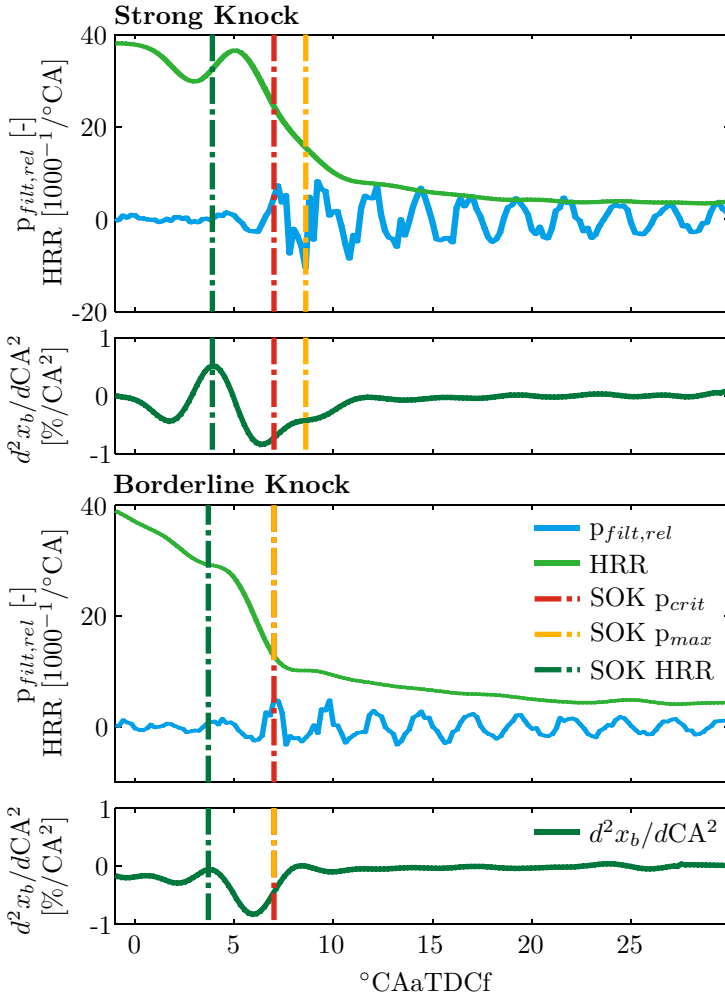The timing for the onset of knock is thus defined based on the heat

Figure 4.5: *Heat release rate and first derivative, pressure fluctuation amplitude and different start of knock criteria: Strong (up) and borderline (down) knocking case. Measurement operating point: 4500 rpm, T_{in}=80° C, 45.00° CA SA.*

release rate, being the cause of knock. The detection of knock is based on the pressure oscillations, being the resulting phenomenon of knock.

4.2.3   Mean versus single cycles

Sections 4.2.1 and 4.2.2 define a knock criterion for a single cycle. As shown in figure 4.2 the knock intensity changes strongly cycle by cycle within the same operating point. It is of interest to define, also for the mean cycle, a criterion which detects whether an operating point can be considered a knocking operating point. In this way the knock limited spark advance, $KLSA$, which is the earliest spark timing without knock, can be found. Earlier spark timings should then be avoided during normal operation.

Figure 4.6 shows for two operating points the cumulative distribution of the $MAPO_{rel}$ values. In this way the fraction of the cycles that knock, i.e. with a $MAPO_{rel}$ value higher than 4, is visible. A fraction of 5% knocking is seen [108] as a significant amount to define the operating point as knocking. The $MAPO_{rel}$ value below which 95% of the cycles are situated is called the $MAPO_{95}$ value. When this value is higher than 4, the mean cycle is counted as knocking. In a similar way, using the actual MAPO value instead of the relative, a knock index for the mean cycle can be defined. 95% of the cycles then have a maximum pressure oscillation amplitude of Δp_{95}.
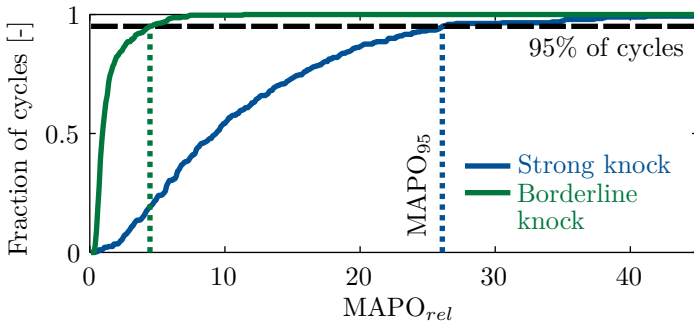

Figure 4.6: *Cumulative distribution of the $MAPO_{rel}$ values for a cycle at borderline knock and at strong knock. 95% line and $MAPO_{95}$ values. Measurement operating points: 4000 rpm, T_{in}=120° C, 33.00 and 37.50° CA SA.*

$$MAPO_{95} > 4 \qquad\qquad (4.11)$$

On the other hand, the percentage of the cycles within one operating point that have a $MAPO_{rel}$ value higher than 4, thus those that knock, can be calculated. This parameter is called the knocking tendency, $KnTd$. An operating point with $MAPO_{95}$=4 has a $KnTd = 5\%$.

5   Auto-ignition delay times

The differences between ethanol and iso-octane as fuels are discussed in section 2.1. Due to the importance of the auto-ignition delay time in modeling knock, a separate chapter is dedicated to an overview of the literature available on this subject for both fuels. The definition of ignition delay time (IDT), in this work, always relates to auto-ignition, associated with knock. For both iso-octane and ethanol the published experimental results for the ignition delay times, followed by the chemical kinetic models are presented. The most detailed chemical kinetic model for each fuel is selected and a correlation has been fit to the ignition delay time data. Finally those correlations are compared to the ones available in literature.

5.1   Definition and importance of the ignition delay time

Mainly the chemical kinetics control the knock mechanism. During the combustion cycle the gases in front of the flame are compressed and heated. When the temperature and pressure in the end gas are high enough, the mixture can auto-ignite. The ignition delay time of a combustible mixture is a function of the composition, the temperature and the pressure. A chemical kinetic analysis of the ignition at a wide range of operating conditions can explain the reaction paths that are followed and can lead to the definition of ignition delay time correlations.

Most hydrocarbons have three modes: low temperature, intermediate temperature and high temperature. In the lower temperature range chain branching reactions build up the radical pool and increase the temperature. At higher temperatures, in the intermediate range, the radicals decompose back to their reactants because of their instability,

causing a negative temperature dependency for the ignition delay time. Only at temperatures higher than the intermediate regime the high temperature reactions dominate and the final combustion is initiated [109]. Measurements for ethanol have shown that it does not exhibit a negative temperature coefficient (NTC) at knock relevant temperatures. The ignition delay time in the low temperature range is high, resulting in excellent knock resistance. For ethanol blends the radical pool created at lower temperatures by gasoline initiates low temperature chemistry also for ethanol. For decreasing ethanol content in gasoline the negative temperature coefficient increases [110]. The ignition delay times for different ethanol blends in gasoline can be seen in figure 5.1. The increasing importance of the low temperature chain branching with decreasing ethanol content can be observed. The figure explains why fuels with a high sensitivity (RON - MON), such as ethanol, are more resistant to auto-ignition at low temperature and high pressure, but relatively less resistant at high temperatures and low pressure [111]. At high temperatures (above the NTC region for gasoline) the ignition delay time of ethanol is even slightly lower than that of gasoline.

5.2 State of the art - Ignition delay time measurements

Many researchers have tried to determine the ignition delay times of different fuels at a wide range of operating parameters experimentally. This section gives an overview of the published results for both ethanol and iso-octane.

5.2.1 Measurement methods

Ignition delay times are typically measured using either a shock tube or a rapid compression facility. The latter have longer residence times, but include the compression phase and the corresponding motion of the test gas. Shock tubes have lower residence times, but almost instantly reach the test conditions.
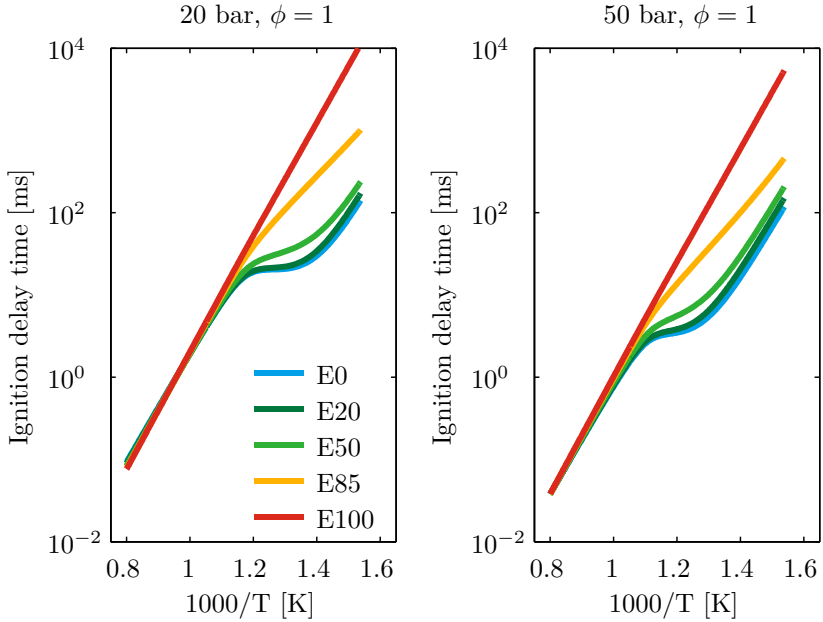
Figure 5.1: *Ignition delay times of ethanol blends (E0 ... E100) in gasoline at 20 bar (left) and 50 (bar) for $\phi = 1$ using the equation proposed in [112] illustrating the two stage behavior for gasoline and single stage behavior for ethanol.*

Shock tubes

A device that is often used to measure the ignition delay time of a fuel-air mixture is a shock tube. Compared to other devices, a shock tube can increase the temperature and pressure of the test gas very quickly thus eliminating the effects of the heating or compression processes. A high pressure driver gas and the low pressure test gas are separated. When the diaphragm breaks, a shock wave is generated and is reflected at the test gas side bringing the test gas under higher pressure and temperature. The residence time for the elevated pressure is typically low and depends on the facility. A typical pressure trace for a shock tube is shown in figure 5.2. The time between the arrival of the reflected shock wave and the ignition is the ignition delay time.
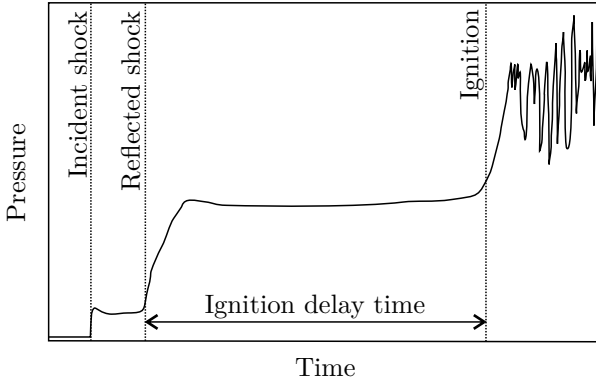
Figure 5.2: *Qualitative pressure trace in the shock tube during ignition delay time measurements.*

Rapid compression machine

Several research groups have rapid compression machines (RCM) installed and use them among others to study the ignition characteristics of fuels. A RCM is typically a piston that is accelerated by compressed gas. The piston can be either free floating or expansion can be prevented in which case pressure and temperatures can be sustained for over 10 ms. The compression ratio can be either fixed or can be set by changing the stroke. Different test gas temperatures can be obtained by changing the diluent and thus the specific heat of the mixture.

5.2.2 Iso-octane

Table 5.1 gives an overview of published data for measurements of ignition delay times for iso-octane using a shock tube. The operating parameters, the oxidizers as well as the year of publication and whether or not a correlation for the ignition delay times is available are given in the table.

Early measurements were carried out at relatively low pressures and high temperatures. Two different modes of ignition were observed: strong and mild ignition. Strong ignition was identified by the shock wave initiated at the back wall of the shock tube. Mild ignition is defined by the chemical reactions at distinct points in the test gas producing essentially constant pressure flames [113].

Table 5.1: *Overview of ignition delay time experiments for iso-octane in a shock tube.*

Author	Ox.	ϕ (-)	T (K)	p (bar)	Corr.	Year	Ref.
Vermeer et al.	O_2,Ar	1	1200 - 1700	1 - 4	No	1972	[113]
Burcat et al.	O_2,Ar	0.25 - 1.0	1100 - 1700		Yes	1993	[114]
Fieweger et al.	air	0.5 - 2.5	700 - 1250	13 - 36	No	1994	[115]
Blumenthal et al.	air	1.0	800 - 1335	5 - 14	No	1996	[116]
Fieweger et al.	air	0.5 - 2.0	700 - 1300	13 - 45	No	1997	[117]
Davidson et al.	O_2,Ar	0.25 - 2.0	1177 - 2009	1.18 - 8.17	Yes	2002	[118]
Oehlschlaeger et al.	O_2,Ar	0.25 - 2.0	1177 - 2009	1.10 - 12.58	Yes	2004	[119]
Davidson et al.	air	0.5 - 1.0	855 - 1269	14 - 59	No	2005	[120]
Kahandawala et al.	air, Ar	1.0	900 - 1400	1.0	No	2006	[121]
Sakai et al.	air, Ar	1.0	1200 - 1600	2.5	No	2007	[122]
Yahyaoui et al.	air, Ar	0.5 - 1.5	1380 - 1880	2 - 10	No	2007	[123]
Shen et al.	air, Ar	0.25 - 1.0	868 - 1300	7 - 58	No	2008	[124]
Hartmann et al.	air	0.5 - 1.0	713 - 1199	38.9 - 43.2	No	2011	[125]
Malewicki et al.	air	0.52 - 1.68	835 - 1757	21 - 65	No	2013	[126]
Li et al.	O_2, Ar	0.5 - 1.0	1313 - 1554	1.5 - 3.0	Yes	2013	[127]

There is a transition from a smooth pressure profile in a mild igni-
tion towards pressure oscillations during a strong ignition. The strong
ignition limit is shifted towards lower temperatures at higher pressures
[115]. In the shock tube experiments different definitions for the igni-
tion delay time can be found. A first ignition delay time is set at the
beginning of an inhomogeneous deflagrative phase starting from differ-
ent hot spots. At high enough temperatures the deflagration may lead
to a secondary explosion of larger volumes of the unburned gas and
transition into a detonation-like process, which is the second ignition
delay time. This second delay time corresponding to the detonation
and strong pressure oscillations and is found to be the best approx-
imation for the chemical ignition delay time. A third delay time is
defined for the cool flame process that occurs during the two-step low-
temperature oxidation of some hydrocarbons. Different from the first
ignition delay time, the cool flame gives only a small increase in pres-
sure. The cool flame proceeds in a relatively homogeneous way with a
velocity almost equal to the reflected shock. In the high temperature
range the auto-ignition proceeds in a detonative way. In the interme-
diate temperature range the deflagration becomes more important. At
low temperatures no secondary detonation is observed. Experiments
at different equivalence ratios show that the NTC is more pronounced
towards richer mixtures [117]. Mild ignition originates at hot spots and
propagates through the combustion chamber with a smooth pressure
profile. Strong ignition leads directly to a detonative mode without
flame fronts and can either occur as a first ignition or after the mild
ignition in a transition from deflagration to detonation. The flame
speed after a strong ignition is one order of magnitude larger than for
a mild ignition. The structure of the deflagration can be either spher-
ical or planar. A spherical deflagration may or may not develop into
a strong ignition; planar deflagrations are always followed by a strong
ignition [116]. Later measurements with more advanced shock tubes
allowed for measurements at higher pressures and lower temperatures
thus expanding the range of measured operating conditions. A visual
representation of the operating ranges for the different experiments can
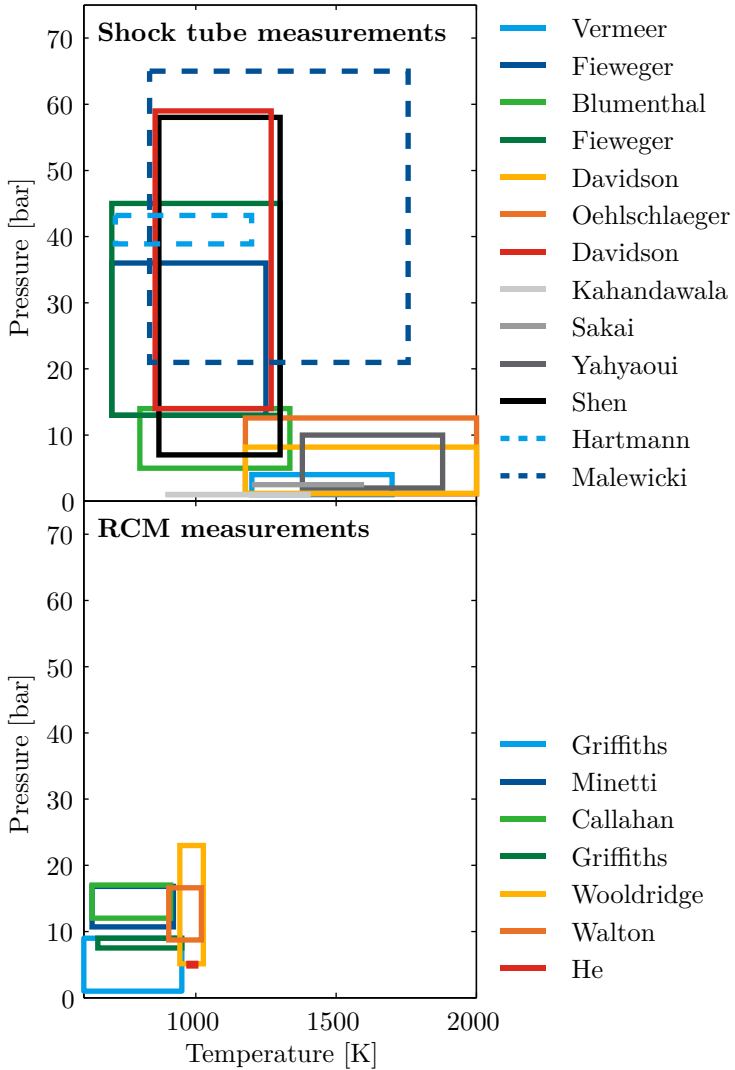be seen in figure 5.3.

Figure 5.3: *Operating ranges for the shock tube (top) and RCM (bottom) ignition delay time experiments for iso-octane (only $\phi = 1$).*

Table 5.2: *Overview of ignition delay time experiments for iso-octane with an RCM.*

Author	Ox.	ϕ (-)	T (K)	p (bar)	Corr.	Year	Ref.
Halstead et al.	air, Ar, CO_2	0.5 - 1.4	600 - 850		No	1977	[128]
Griffiths et al.	air, Ar, CO_2	1	600 - 950	<9	No	1993	[129]
Minetti et al.	air	0.8 - 1.2	630 - 920	10.7 - 16.8	No	1996	[130, 131]
Callahan et al.	air, Ar, CO_2	1	630 - 910	12 - 17	No	1996	[132]
Griffiths et al.	air, Ar, CO_2	1	650 - 950	7.5 - 9.0	No	1997	[133]
Tanaka et al.	air	0.2 - 0.5	798 - 878	40.4 - 44.0	No	2003	[134]
Wooldridge et al.	air, Ar	0.25 - 1.0	943 - 1027	5.12 - 23	Yes	2005	[135]
Walton et al.	air, Ar	0.2 - 1.98	903 - 1020	8.7 - 16.6	Yes	2007	[136]
He et al.	air, Ar	0.4 & 1.2	975 - 1000	4.8 - 5.2	No	2007	[137]
Mittal and Sung	air, Ar, CO_2	0.75	740 - 1060	15 - 45	No	2008	[138]

An overview of the published results for the ignition delay times of iso-octane determined using a rapid compression machine is given in table 5.2. RCM measurements are typically lower in temperature compared to the shock tube measurements. The temperature after compression is often changed by replacing the inert gas (replacing N_2 with Ar for higher temperatures and CO_2 for lower temperatures). The pressure after compression is varied by changing the compression ratio and the initial pressure. Similar to the experiments with shock tubes at low temperatures a two-stage ignition with a cool flame preceding the main ignition is observed. With increasing temperatures the cool flame becomes less and less important and finally disappears. For intermediate temperatures a NTC for the ignition delay time is observed. The air-to-fuel ratio does not seem to influence the cool flames, but its influence is only visible in the main ignition [130]. The cool flame ignition delay times are reduced with increasing temperature until the process is not observed anymore [132]. The NTC region is shifted towards higher temperatures as pressure increases [131]. Recent ignition delay time measurements with RCMs for iso-octane are inspired by the interest in homogeneous charge compression ignition combustion and cover also very lean operating conditions. The operating ranges for the published results that include stoichiometric combustion are shown in figure 5.3 and are compared to the shock tube measurements.

5.2.3 Ethanol

An overview of the published experiments on the ignition delay times of ethanol is given in table 5.3. Early work on the study of ethanol combustion started in the 1950s [139, 140]. Cooke et al. [141] are the first to publish shock tube measurement results for the ignition delay time of ethanol. Natarajan and Bhaskaran [142] also carried out low pressure, high temperature IDT shock tube measurements, but for different stoichiometries. This became one of the standard data sets to which kinetic models are tested. Borisov [143] performed shock tube measurements for acetaldehyde and ethanol mixtures with oxygen (dilution with both Ar and He) also including low temperatures as well as pressures up to 6 bar. Dunphy et al. [144] and Curran et al. [145] added measurements for medium to high temperatures at relatively low pressures for lean up to rich mixtures.

Table 5.3: *Overview of ignition delay time experiments for ethanol in a shock tube.*

Author	Ox.	ϕ (-)	T (K)	p (bar)	Corr.	Year	Ref.
Cooke	O_2,Ar	1	1570 - 1870	1.27 - 1.4	No	1971	[141]
Natarajan	O_2,Ar	0.5, 1, 2	1300 - 1700	1, 2	Yes	1981	[142]
Borisov	O_2,Ar, He	0.25 - 1	700 - 1570	0.5 - 6	Yes	1989	[143]
Dunphy	O_2,Ar	0.25 - 2	1080 - 1660	1.8 - 4.6	Yes (3)	1991	[144]
Curran	O_2,Ar	0.25 - 1.5	1100 - 1900	2, 3, 4.5	Yes	1992	[145]
Heufer	air	1	800 - 1400	13, 19, 40	Yes	2010	[146]
Cancino	air	0.3, 1	650 - 1220	10, 30, 50	No	2010	[147]
Lee [1]	air	1	705 - 1300	40, 80	No	2011	[148]

[1] Also RCM experiments
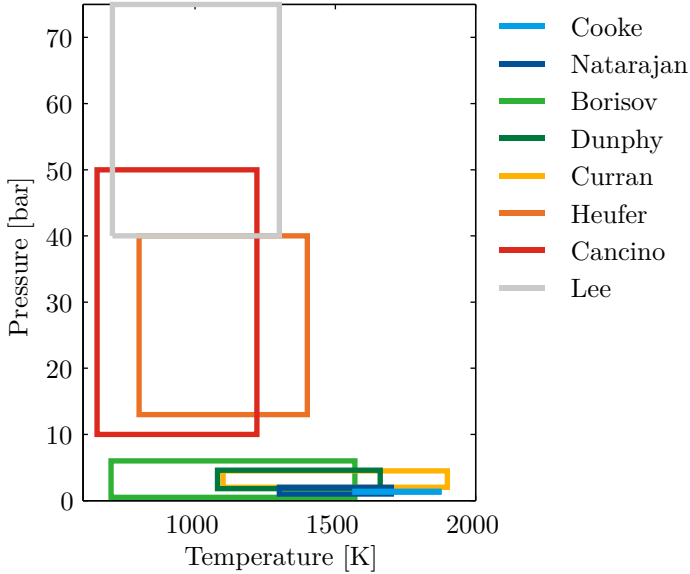
Figure 5.4: *Operating ranges for the ignition delay time experiments for ethanol (only $\phi = 1$).*

More recent work by Haas et al. [110] presents species profile measurements for the low and intermediate temperature range (525 - 900 K) at 12.5 atm and equivalence ratios of 0.43 and 0.91 using a variable pressure flow reactor facility. The experiments show that ethanol does not have a NTC for the tested conditions. At low temperatures, ethanol is consumed primarily through H-atom abstraction to form one of three isomeric C_2H_5O radicals. Only at temperatures higher than 900K the uni-molecular homogeneous decomposition of ethanol becomes important. In the experiments heterogeneous decomposition of ethanol to ethylene and water can be observed. The model proposed by Li et al. [149] is updated for and extended to ethanol/PRF blends. The reaction mechanism agrees well with the existing IDT shock tube measurements presented in [150].

Cancino et al. [147] present IDT measurements in a shock tube at intermediate temperatures and high pressures. The experiments show a flattening (non-log-linear) of the ignition delay time for ethanol towards low temperatures ($T < 1000K$). Similar behavior is seen in the

experiments carried out by Heufer et al. [146] in their high pressure shock tube. It is suggested that the low temperature behavior can be explained by a NTC region for ethanol. Recent experiments with both shock tubes and RCM cover pressures of up to 80 bar [148]. An overview of the operating ranges of the published results can be seen in figure 5.4.

5.3 State of the art - Chemical kinetic models

Many chemical kinetic mechanisms have been developed to be included in combustion simulations. These mechanisms have different levels of detail and are often a trade-off between computational burden and accuracy. The number of included reaction steps and species are a measure for the level of detail. These mechanisms are typically calibrated against ignition delay time, flame speed and species measurements. They can then be used for example to predict the ignition delay time within the operating range the mechanism is validated.

5.3.1 Iso-octane

For iso-octane, as a PRF, many chemical kinetic models have been developed. Table 5.4 gives an overview of the available mechanisms for iso-octane oxidation, the number of species and steps and the experiments to which they are validated as well as the year of publication.

Based on the Shell ignition model and the principles introduced by Halstead et al. [151], Cox and Cole [152] developed a skeletal reaction mechanism with 10 species and 15 generalized reactions for the auto-ignition of alkane based hydrocarbon fuels. The temperature, fuel, and air-to-fuel ratio dependence of experiments in an RCM [128] could more or less be explained.

Axelsson et al. [153] published one of the first detailed kinetic reaction mechanisms for iso-octane and n-octane. The mechanism includes 70 species and 500 reactions and is based on mechanisms for smaller fuel molecules. They focus on the difference between the oxidation of n-octane and iso-octane trying to determine the specific reaction paths for both fuels. The mechanism for each fuel contains around 60-62 species and 350 reactions.

Table 5.4: *Chemical kinetic models for iso-octane oxidation.*

| Author | Steps | Species | Validation Measurements | | | Year | Ref. |
			IDT	S_L	Species		
Cox and Cole	15	10	[128]			1985	[152]
Axelsson et al.	500	70		[154]	[155]	1988	[153]
Westbrook et al.	765	212	[113]		[155, 156]	1988	[157]
Schreiber et al.	6	5	[115]			1994	[158]
Côme et al.	2820	463			[159, 160]	1996	[161]
Pitsch et al.	47	25		[162]		1996	[163]
Ranzi et al.	2500	145	[115, 129]		[160, 164, 165]	1997	[166]
Davis and Law	406	69		own	[167]	1998	[168]
Curran et al.	4060	990	[117]		own	1998	[169]
Ogink and Golovitchev	479	101	[117, 170]	[83, 87, 88, 168, 171]		2001	[172]
Curran et al.	3606	859	[113, 115, 117]		[132, 160, 167, 173]	2002	[174]
Soyhan et al.	386	63	[117]			2002	[175]
Tanaka et al.	55	32	[134]			2003	[176]
Buda et al.	1684	351	[117, 130, 131]			2005	[177]
Machrafi et al.	29	27	own			2005	[178]
Jia and Xie	69	38	[117, 120, 134]		[160]	2006	[179]
Lu and Law	959	233			own	2006	[180]

Continued on next page

Table 5.4: *Chemical kinetic models for iso-octane oxidation (Continued from previous page).*

Chaos et al.	723	107	[113, 114, 119, 157]	[90, 168, 181]	[167]	2007	[182]
Ra and Reitz	130	41	[117]			2008	[183]
Mehl et al.	5300	1250	[117, 120, 130, 131, 170, 184, 185]			2009	[186]
Tsurushima	38	33	[117, 170]			2009	[187]
Voglsam et al.	19	18	[117, 120, 184]		[169]	2012	[188]
Liu et al.	111	32	[117]	[91, 189, 190]	[160]	2013	[191]

Table 5.5: *Chemical kinetic models for ethanol oxidation.*

Author	Steps	Species	Validation Measurements			Year	Ref.
			IDT	S_L	**Species**		
Natarajan	56	26	own			1981	[142]
Dunphy	97	30	own			1991	[192]
Curran	>400		own			1992	[145]
Borisov	94				own	1992	[193]
Norton	142				own	1992	[194]
Egolfopoulos	196	35	[141, 142]	own	[194, 195]	1992	[80]
Marinov	383	57	[142, 144, 145]	[80, 83]	[196]	1999	[197]
Saxena	192	36	[142, 144, 145]	[80]		2007	[198]
Li	238	39	[142, 144, 145]	[80, 83]	own	2007	[149]
Dagaud	1866	235			own	2008	[199]
Röhl	228	38	[142, 144]	[80, 83]		2009	[200]
Röhl	374	107		own, [80, 83]		2009	[201]
Syed	672	142		[80]		2010	[111, 202]
Cancino	1349	136	own			2010	[147]
Leplat	252	36	[142, 144]	[81, 85]	own	2011	[203]
Lee	279	44	own			2011	[148]

Based on the availability of new experiments chemical kinetic reaction mechanisms are continuously developed. More detailed models [157,161,166,168,169,174,177,186] with a high number of reactions and species aim at capturing correctly all the reaction paths. Reduced and skeletal models aim at computational efficiency while retaining the desired level of accuracy for the chosen purpose [158,163,172,175,176,178–180, 183, 187, 188, 191, 204]. The most widely validated detailed mechanism for the calculation of ignition delay times is proposed by Mehl et al. [186] It is the latest update of the LLNL model developed at the Lawrence Livermore National Laboratory [169, 174].

5.3.2 Ethanol

Compared to iso-octane, ethanol has received less attention for chemical kinetic modeling. However, several kinetic models for ethanol combustion have been developed and are listed in table 5.5.

One of the earliest kinetic models for ethanol oxidation was proposed by Natarajan and Bhaskaran [142] and consists of 26 species and 56 reaction steps. Up to Norton et al. [194] different chemical kinetic models are developed mainly for high temperature and low pressure oxidation of ethanol to match their own IDT or species measurements. Egolfopoulos et al. [80] added the information of new laminar flame speed measurements and compared their model to the available other data. Marinov [197] developed the first detailed chemical kinetic model for high temperature ethanol oxidation. The reaction mechanism was tested against IDT, laminar flame speed and species profile measurements with good agreement.

With the availability of new data at high pressures and low temperatures more mechanisms are developed. Especially the models of Cancino et al. [147] and Lee et al. [148] are of interest because they are based on the high pressure ignition delay time results and include the flattening of the ignition delay time towards lower temperatures at elevated pressures.

5.4 Ignition delay time correlations

Using the results from the ignition delay time experiments or the chemical kinetic mechanisms, empirical correlations capturing the behavior of the ignition delay time as function of pressure, temperature and mix-

ture composition can be derived. In the next subsections an overview of the available correlations is given followed by the derivation of a new correlation based on chemical kinetic calculations using the most detailed mechanism for each fuel.

5.4.1 Iso-octane

Three main correlations for the ignition delay time of iso-octane, τ, can be found in literature. The first one is suggested by Yates and Viljoen [205]. They use the LLNL mechanism [174] to carry out around 1500 calculations for the ignition delay times of different PRF blends (from PFR0 to PFR100) and blends of PRF80 with methanol at conditions $p = 12 - 50 bar, T = 600 - 1200K, \phi = 0.25 - 4.0$ and no dilution. A further analysis using different ethanol blends is presented in [112]. For the correlation of the ignition delay time, a distinction is made between the low, τ_l, and high, τ_h, temperature ignition range and a formulation for the cool flame region, τ_{CF}, is presented. The correlation for iso-octane is given in equations 5.1-5.6.

$$\tau = \tau_l + \tau_{CF} \left(1 - \frac{\tau_l}{\tau_h} \right) \tag{5.1}$$

$$\tau_l = exp\left(-17.01\right) \phi^{-0.327} p^{-0.268} \times exp\left(14833/T\right) \tag{5.2}$$

$$\tau_h = exp\left(-11.69\right) \phi^{-0.711} p^{-0.964} \times exp\left(15326/T\right) \tag{5.3}$$

$$\tau_{CF} = exp\left(-11.69\right) \phi^{-0.711} p_{CF}^{-0.964} \times exp\left(\frac{15326}{T + 1.103\left(T_{CF} - T\right)} \right) \tag{5.4}$$

$$T_{CF} = T + 0.5 \left(\Delta T_{CF} + \sqrt{\Delta T_{CF}^2 + 4745} \right) \tag{5.5}$$

$$\Delta T_{CF} = -1.194 \left(T - 720 p^{0.053} \phi^{0.06015} \left(\frac{100}{99 + \phi} \right)^{1.0162} \right) \tag{5.6}$$

A second correlation is proposed by Goldsborough [206]. He calculates the influence of the composition, temperature and pressure on the ignition delay time using the LLNL mechanism [186] in order to define the equations for the correlation (eq. 5.7 - 5.14). An extensive overview of the experimental data gathered in literature is given and the measurement results are used to calibrate the 37 correlation parameters. The correlation is valid for the ranges $\phi = 0.2 - 2.0, p =$

$1 - 60atm, \chi_{O_2} = 0.125 - 21\%, T = 650 - 2000K$. The final correlation (eq. 5.7) has an Arrhenius form with exponents for the air-to-fuel ratio, α, pressure, β and oxygen concentration, γ. The temperature dependency including the two-stage ignition behavior is incorporated in the exponents and the exponential factor.

$$\tau = A\phi^\alpha p^\beta \chi_{O_2}^\gamma \times exp(\lambda) \tag{5.7}$$

$$\alpha = \alpha' + \left(\sum_{i=0}^{3} a_i T^{*i} \right) \times exp\left(-(T^*/T_\alpha^*)^j \right) \tag{5.8}$$

$$\beta = \beta' + \left(\sum_{i=0}^{3} b_i T^{*i} \right) \times exp\left(-(T^*/T_\beta^*)^k \right) \tag{5.9}$$

$$\gamma = \gamma' + \left(\sum_{i=0}^{3} c_i T^{*i} \right) \times exp\left(-(T^*/T_\gamma^*)^l \right) \tag{5.10}$$

$$\lambda = \Omega \left(1 - \Xi \right) \tag{5.11}$$

$$\Omega = \sum_{i=0}^{2} d_i T^{*i} - \left[\sum_{i=0}^{2} d_i T^{*i} - \sum_{i=0}^{2} e_i T^{*i} \right] \times exp\left(-(T^*/T_\Omega^*)^m \right) \tag{5.12}$$

$$\Xi = C exp\left[-(T^* - T_\Xi^*)^2 / 2\sigma^2 \right] / \sqrt{2\pi\sigma^2} \tag{5.13}$$

$$C = C_1 \left\{ 1 - exp\left[-a \left(p - p_{low} \right)^n / \left(p_{high} - p_{low} \right)^n \right] \right\} \tag{5.14}$$

A third and last correlation is proposed by Douaud and Eyzat [207] and is often used in knock modeling. The parameters of a single step Arrhenius equation are derived from engine measurements yielding the results in equation 5.15. The analysis is carried out for different PRF fuels and the effect of the octane number is included in the correlation.

$$\tau = 17.68 \left(\frac{ON}{100} \right)^{3.402} p^{-1.7} exp\left(\frac{3800}{T} \right) \tag{5.15}$$

The LLNL mechanism is selected as the most detailed and accurate chemical kinetic mechanism for iso-octane oxidation. The CHEMKIN toolbox is used in combination with SENKIN to computed ignition delay times in a closed adiabatic reactor for a fixed initial pressure and varying initial temperatures. The temperatures are varied between 600 and 1050 K and the pressures between 1 and 80 bar for stoichiometric

Table 5.6: *Parameter values for the 3-Arrhenius type correlation for the ignition delay time of iso-octane.*

i	A	γ	E_a
1	3.997×10^{-3}	-1.254	4458
2	4.075	-19.63	5146
3	1.280×10^{-8}	-1.327	1.699×10^4

mixtures, thus reflecting the conditions for the knock measurements as conducted on the engine test bench. The parameters of a 3-Arrhenius type correlation (equations 5.16 and 5.17) are fit to the obtained simulation results for the ignition delay time in the same way as has been done in [208]. The parameter values of the fit with $R^2 = 0.9638$ are given in table 5.6.

$$\frac{1}{\tau_{fit}} = \frac{1}{\tau_1} + \frac{1}{\tau_2 + \tau_3} \tag{5.16}$$

$$\tau_i = A_i p^{\gamma_i} exp\left(\frac{E_{a,i}}{T}\right), i = 1 \ldots 3 \tag{5.17}$$

A comparison of the different ignition delay time correlations can be seen in figure 5.5. Yates equation and the 3-Arrhenius fit are quite similar due to the fact that they are both based solely on the same mechanism. The Yates equation captures the negative temperature coefficient region better. For low pressures the Goldsborough equation is similar to the equations based on the LLNL mechanism. At higher pressures the ignition delay times predicted by the Goldsborough equation are much shorter. The Douaud equation neglects the negative temperature coefficient region and acts as an average value over the lower and intermediate temperature range.

5.4.2 Ethanol

For ethanol no extensive study for a correlation of the ignition delay time exists, as it is the case for iso-octane. Several authors have fit their experimental results to an Arrhenius equation as indicated in table 5.3. The only correlation also valid for higher pressures is the one presented by Heufer et al. [146]. Equation 5.18 shows the single step Arrhenius correlation based on their shock tube measurements.
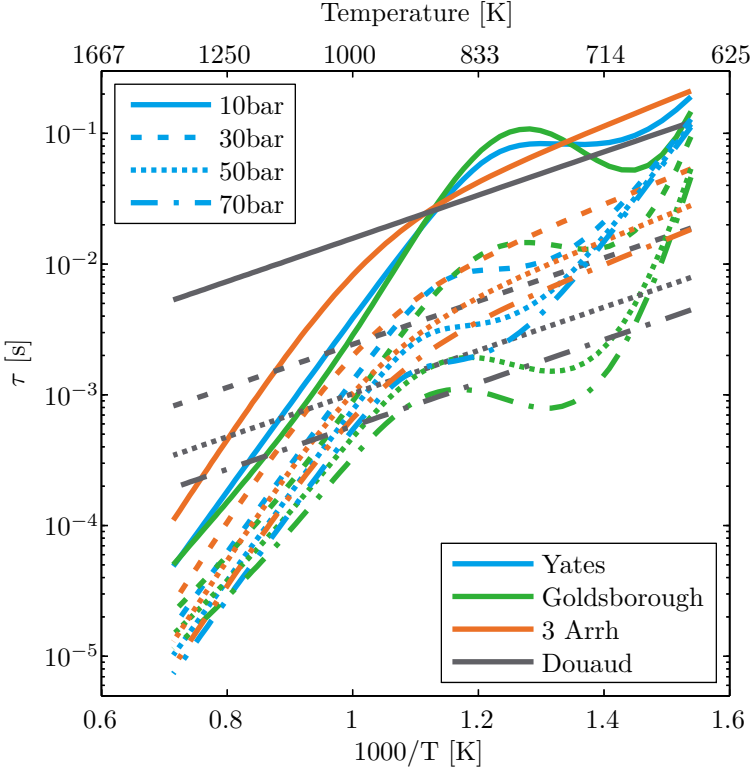
Figure 5.5: *Comparison of the ignition delay time correlations for iso-octane at $\phi = 1$: Yates (eq. 5.1), Goldsborough (eq. 5.7), 3-Arrhenius (eq. 5.16) and Douaud (eq. 5.15).*

$$\tau = 7.5 \times 10^{-9} p^{-0.77} exp\left(\frac{14000K}{T}\right) \quad (5.18)$$

The correlation proposed by Douaud and Eyzat (equation 5.15) can also be used for ethanol by adapting the octane number.

The Cancino mechanism is selected as the most detailed mechanism. Chemical kinetic calculations are carried out for the ignition delay time of ethanol using the Cancino mechanism in the same way as has been done for iso-octane. The results are also fit to a 3-Arrhenius type equation. The resulting parameters can be seen in table 5.7. The

quality of the fit for ethanol is $R^2 = 0.9773$.

Table 5.7: *Parameter values for the 3-Arrhenius type correlation for the ignition delay time of ethanol.*

i	A	γ	E_a
1	4.023×10^{-8}	-1.003	1.305×10^4
2	0.9691	-0.8299	-1985
3	9.755×10^{-11}	-0.6883	1.433×10^4
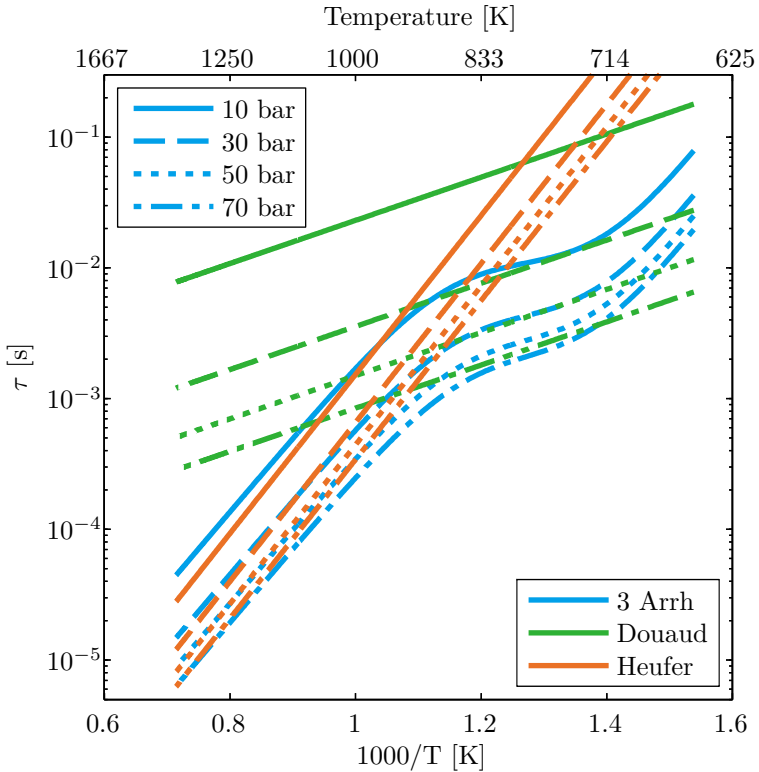
Figure 5.6: *Comparison of the ignition delay time correlations for ethanol at $\phi = 1$: 3-Arrhenius (eq. 5.16), Douaud (eq. 5.15) and Heufer (eq. 5.18).*

A comparison of the three correlations for the ignition delay time of stoichiometric ethanol can be seen in figure 5.6. The 3-Arrhenius fit and the Heufer equation are very similar in the high temperature area. The 3-Arrhenius fit also captures the flattening of the ignition delay time towards lower temperatures, which is also observed in the Heufer experiments (but not in the correlation). The three Arrhenius fit and the Douaud equation are similar for high pressures and low temperatures. At high temperatures and low pressures the Douaud equation overestimates the ignition delay time.

6 Knock modeling

In design phase of a spark ignition engine it is of great importance to know under what operating conditions knock will occur. To this extent many researchers have attempted to model knock using different approaches. This chapter first gives an overview of the models available in literature. In a second part the selected models for this work are discussed. A method of assessing the performance of the different models is introduced as well.

6.1 State of the art

This section presents are literature review on the knock modeling approaches. They can be roughly classified into these categories:

- Empirical formulations based on Arrhenius functions

- Chemical kinetic models, detailed or reduced, following the thermodynamic conditions in the unburned zone and calculating the radical pool build up during the time before auto-ignition. A significant heat release rate predicts the onset of knock.

In a first part the models based on empirical formulations are discussed. In a second part a brief overview of the application of chemical kinetic models is presented.

6.1.1 Empirical formulations based on Arrhenius functions

Most of the empirical models are based on the assumption that the auto-ignition chemistry for knock is cumulative. This is called the

Livengood and Wu [209] assumption and says that the time to the onset of knock, t_{knock}, can be predicted by integrating the inverse of the ignition delay time, τ, as in equation 6.1. When the value of the knock integral, KI, becomes one, knock occurs.

$$KI = \int\limits_{0}^{t_{knock}} \frac{dt}{\tau} = 1 \qquad (6.1)$$

The ignition delay time can be taken from detailed chemical models, derived from shock-tube measurements or using fitted experimental engine data. A very commonly used formulation (e.g. [210]) for the latter is the correlation proposed by Douaud and Eyzat [207] as presented in equation 5.15. Some authors have used engine experiments to adapt the coefficients of the Douaud and Eyzat correlation. For example in Wayne et al. [101] the parameters are fit for their measurements with CNG and the obtained model is then used to design a new cam shaft [211].

Lafossas et al. [212] also use the Douaud and Eyzat correlation for the ignition delay time in their knock model. They state however that the thermodynamic conditions in the compression and combustion strokes evolve strongly and quickly and therefore the Douaud model cannot predict the knock delay directly. Instead the estimated ignition delay time creates a 'precursor' species, Y_p, that is transported with the flow in the combustion chamber. When a limiting value of this precursor, $Y_p = Y^0_{fuel}$ with $Y^0_{fuel} = m^0_{fuel}/m^0_{fg}$, is reached, auto-ignition occurs. The evolution of this precursor is given in equations 6.2 and 6.3 with $\alpha = 1 \left[s^{-1}\right]$, a constant.

$$\frac{dY_p}{dt} = Y^0_{fuel} F\left(\tau\right) \qquad (6.2)$$

$$F\left(\tau\right) = \frac{\sqrt{\alpha^2 \tau^2 + 4\left(1 - \alpha\tau\right)\frac{Y_p}{Y^0_{fuel}}}}{\tau} \qquad (6.3)$$

Corrections to the model have to be made to take the air-to-fuel ratio and dilution of mixtures into account. The effect of air-to-fuel ratio is accounted for by manipulating the octane number in the expression for the ignition delay time as shown in equation 6.4. The effect of dilution is considered by manipulating the pressure in the expression for

the ignition delay time as in equation 6.5, with Y_r being the mass fraction of the residual gases. It is assumed that the presence of residual gas decreases the partial pressure of the reacting components.

$$ON_{eff} = ONexp\left(0.1\left(\phi - 1\right)^2\right) \tag{6.4}$$

$$p_{eff} = \frac{p}{1 + Y_r} \tag{6.5}$$

The model by Lafossas is developed to work in 3D CFD simulations enabling the model to predict also the location of knock onset. A potential application can be to learn from this information for modifications to the combustion chamber. Richard et al. [213] reduced the model to work in 0D engine simulations. The formulation of the equations stays the same, only being integrated over the entire combustion chamber. Equation 6.2 predicts the timing for the onset of knock. For modeling purposes it can however be of interest to know the intensity of knock. A knock intensity parameter, K_n, is proposed and can be calculated as shown in equation 6.6, with x_b being the mass fraction burned, ϕ, the fuel-to-air ratio, θ_{knock}, the crank angle at knock onset and n, the engine speed. K_1 and K_2 are tuning parameters.

$$K_n = K_1\left(1 - x_b \cdot max\left(1, \phi\right)\right)\left(CR - 1\right)\sqrt{1 - \frac{\theta_{knock}}{K_2}}\,N \tag{6.6}$$

Four levels of knock intensity can be distinguished:

- $K_n < 0.5$: no knock

- $0.5 \leq K_n < 1$: trace knock

- $1 \leq K_n < 1.5$: medium knock

- $1.5 \leq K_n$: severe knock

The knock prediction model described by Richard et al. is calibrated for gasoline. Bougrine and Richard [214] validated the model for gasoline/ethanol blends with the only modification to the knock model to account for ethanol as a fuel the octane number in the ignition delay time prediction. In a later publication Richard et al. [33] extended the simulation model for the use with a highly downsized DISI engine burning E20 and E85. Operating maps are created using the

simulation software for the use in a vehicle simulation package in order to calculate the effect of the operating map on the fuel consumption in the Artemis driving cycle. The IFP model is also used in [215] in a multi-dimensional simulation effort for methanol combustion to study the effect of engine parameters on knock.

Yates et al. [216] address the octane number testing in CFR engine for different fuels and the often observed difference with knock limited spark advance tests. An engine model able to simulate the RON and MON tests is used together with a two stage ignition delay model derived from detailed chemistry schemes [217]. It is observed that the RON tests fall in the low temperature regime for most fuels and the MON tests in the high temperature regime, which corresponds well to the experience that RON accounts for low speed knock and MON for high speed knock. Ethanol however has no explicit negative temperature coefficient with respect to ignition delay time and is thus very knock resistant in the area for RON tests.

6.1.2 Chemical kinetic models for knock prediction

By solving a chemical kinetic model for the unburned zone, knock is predicted using the heat release rate in this zone (equation 6.7). In [218] a mass fraction burned in front of the flame, x_{Qu}, of 0.4% is taken as a threshold value for the knock criterion.

$$x_{Qu} = \frac{1}{m_f H_u} \int \frac{dQ_u}{dt} dt \cdot 100 \qquad (6.7)$$

A model that is often used to predict knock is the so-called Shell model. The Shell model is a lumped chemical kinetic model to compute the ignition delay time of hydrocarbons [151]. It consists of an eight-step chain branching reaction scheme with 5 species and it captures the low temperature auto-ignition behavior of hydrocarbons. A mathematical formulation and application for a gasoline and Diesel engines can be found in [219] and [220] respectively. In [221] a modified Shell model is used to predict knock in a 3D code for several engine and fuel combinations. Nakama et al. [222] also uses an extended Shell model to predict knock in 3D numerical simulations. The study focuses on the influence of the wall temperature on the onset of knock location. Wall temperature and wall heat flux measurements are carried out for validation. A finite elements mesh is used to compute the local temper-

atures. The model is then used to suggest improvements to the engine design in order to avoid knock.

Other reduced kinetic models have been developed to predict knock. For example for iso-octane, n-heptane and toluene mixtures in a CFR engine [223]. In [224] Knock prediction is done using homogeneous 2-zone model and solving a detailed chemical kinetic scheme for the ignition delay time of hydrocarbons in the unburned mixture. In principle, any of the chemical kinetic models presented in chapter 5 can be solved in the unburned zone to predict auto-ignition.

6.2   Selected models for evaluation

This work focuses on the application of fast 1D simulation tools using empirical knock models, without 3D CFD calculations. The presented empirical knock models are combined with the different correlations for the ignition delay times of both ethanol and iso-octane. The results are then compared to the measurements. As a knock model formulation both the integral of the ignition delay time (Livengood and Wu) and the IFP model are used. They are combined with the Douaud, Heufer and 3-Arrhenius fit for ethanol and the Douaud, Yates, Goldsborough and 3-Arrhenius fit for iso-octane. Tables 6.1 and 6.2 list the names for the knock models used in this work with the knock integral and the ignition delay time correlation for iso-octane and ethanol respectively. The IFP knock model has been rearranged as a function of a knock integral KI, for comparison with the Livengood and Wu model.

6.3   Fitness evaluation functions

In order to evaluate the accuracy of a knock model compared to the measurements, two fitness functions are introduced. Equation 6.8 takes into account all cycles; equation 6.9 evaluates only the knocking cycles as determined by the experiments ($MAPO_{rel} \geq 4$). The formulations can be used for either the mean cycles or all the single cycles.

$$
f_{fit} = \frac{1}{n} \cdot \left(\sum_{MAPO_{rel}<4\&KI>1} (KI_{end} - 1) + \sum_{MAPO_{rel}\geq4} |KI_{SOK} - 1| \right)
$$
$$(6.8)$$

Table 6.1: *Selected knock models for iso-octane.*

Name	Knock integral	Eq.	IDT corr.	Eq.
Douaud	$KI = \int\limits_{0}^{t_{knock}} \frac{dt}{\tau}$	6.1	Douaud	5.15
IFP	$\frac{dKI}{dt} = \frac{\sqrt{\alpha^2 \tau^2 + 4(1-\alpha\tau)KI}}{\tau}$	6.3	Douaud	5.15
Yates	$KI = \int\limits_{0}^{t_{knock}} \frac{dt}{\tau}$	6.1	Yates	5.1
Golds-borough	$KI = \int\limits_{0}^{t_{knock}} \frac{dt}{\tau}$	6.1	Golds-borough	5.7
3 Arrh.	$KI = \int\limits_{0}^{t_{knock}} \frac{dt}{\tau}$	6.1	3 Arrh.	5.16

Table 6.2: *Selected knock models for ethanol.*

Name	Knock integral	Eq.	IDT corr.	Eq.
Douaud	$KI = \int\limits_{0}^{t_{knock}} \frac{dt}{\tau}$	6.1	Douaud	5.15
IFP	$\frac{dKI}{dt} = \frac{\sqrt{\alpha^2 \tau^2 + 4(1-\alpha\tau)KI}}{\tau}$	6.3	Douaud	5.15
Heufer	$KI = \int\limits_{0}^{t_{knock}} \frac{dt}{\tau}$	6.1	Heufer	5.18
3 Arrh.	$KI = \int\limits_{0}^{t_{knock}} \frac{dt}{\tau}$	6.1	3 Arrh.	5.16

$$f_{fit,knock} = \frac{1}{n_{MAPO_{rel}\geq 4}} \cdot \sum_{MAPO_{rel}\geq 4} |KI_{SOK} - 1| \qquad (6.9)$$

In equation 6.9 $f_{fit,knock}$ is the mean error on the KI value at the timing for the onset of knock. At the timing for the onset of knock, as determined by the experiment, the KI value of the knock model should be equal one. A value higher than one predicts knock too early. When KI_{SOK} is lower than one, knock is predicted too late in the cycle or not at all. In f_{fit} all cycles and/or operating points are con-

sidered, also those that do not knock. In the case that the experiment does not detect knock and the knock model does not predict knock, there is no contribution to the fitness function, since the prediction is correct. When there is no knock detected in the experiment, but the model predicts knock (i.e. KI at the end of the cycles, KI_{end}, is larger than one) the difference between KI_{end} and one is considered as the error on the prediction. Averaging over the number of cycles and/or operating points, n, the fitness function yields the average error on the knock prediction. For an ideal knock model both f_{fit} and $f_{fit,knock}$ are zero, in which case the prediction of knock is perfect. The aim is to differentiate between knocking and regular cycles. The knock intensity is not further considered as a parameter.

7 Combustion chamber geometry and thermal boundary layer

The specific geometry of the combustion chamber and the location of the spark plug play a major role in the occurrence of knock. This chapter discusses the combustion chamber of the engine used in the experiments in more detail. The second part of this chapter deals with the influence of the walls and the thermal boundary layer on the on auto-ignition for knocking operating points. Extensions to the knock modeling approaches are presented to take into account these effects.

7.1 Cylinder geometry

The test bench configuration and the engine used for this work are first presented in chapter 2. In this section the shape of the combustion chamber is discussed in more detail. Figure 7.1 shows the combustion chamber with the piston in the TDC position. The bottom image contains a cut through the symmetry plane that includes the intake and exhaust paths. The piston has a compression dome in the middle with valve pockets on either side. The spark plug is located between the valves slightly off-center. The top image shows a view from the top on one half of the combustion chamber with the intake valve on the left hand side. A squish area where the cylinder head is flat is located on the intake side.

To illustrate the typical flame propagation in this combustion chamber, a spherically propagating flame is drawn on the image. The propagation speed of the flame changes from cycle to cycle and the flame
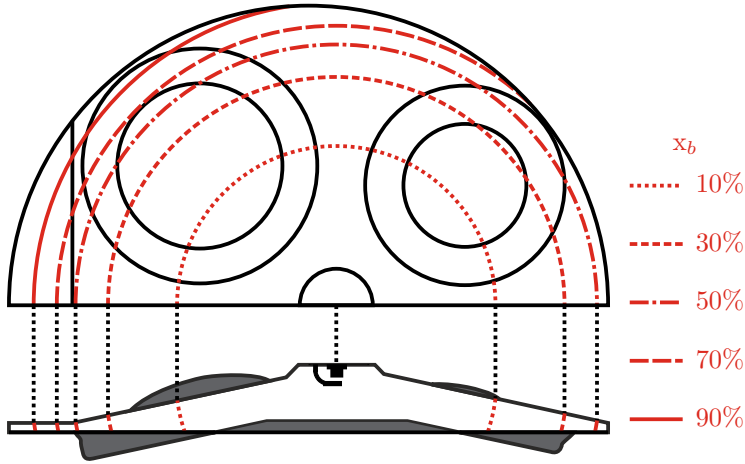
Figure 7.1: *Cylinder geometry with the piston at TDC. Flame location at different mass fractions burned under the assumption of a smooth spherically propagating flame.*

surface in reality is never a smooth sphere. The assumption of a spherical flame can nonetheless give some insight as to where in the combustion chamber knock is typically initiated and where the flame is at the time of auto-ignition. Each of the red lines corresponds to a given percentage of fuel mass burned. They are constructed taking into account the density ratio between the burned and the unburned zones. The combustion chamber is first divided into a burned and an unburned zone by imposing spheres of different diameters. In this way the two volumes are given as a function of the flame radius. Then, the density ratio is applied to the volumes to obtain the mass fraction burned as a function of the flame radius. Because the density of the burned zone is much higher than that of the unburned, the volume occupied by the burned mass is proportionally large. At first the flame radius increases quickly for relatively little mass burned. At the end of the cycle much fuel is enclosed in the volume close to the cylinder walls. The relation between the volume and mass fractions burned is given in equation 7.1.

$$V_b = \frac{\frac{\rho_u}{\rho_b}}{\frac{1}{x_b} - 1 + \frac{\rho_u}{\rho_b}} \tag{7.1}$$
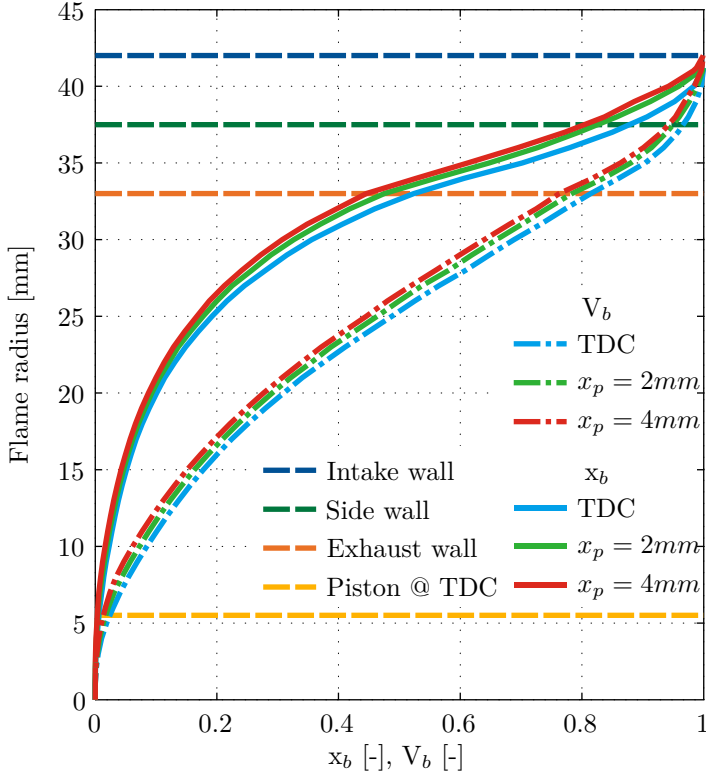
Figure 7.2: *Flame radius as a function of mass and volume fraction burned at different piston positions assuming a spherically propagating flame.*

Figure 7.2 shows the flame radius as a function of the mass, x_b, and volume, V_b, fractions burned under the previously mentioned assumptions. The locations of the intake, exhaust and side walls as well as the distance from the spark plug to the piston in the TDC position are given. The flame radius as a function of the mass fraction burned is always higher than the flame radius as a function of the volume fraction burned due to the difference in density between the burned and unburned zones. The flame reaches the piston dome very quickly. After the initial phase the flame propagates in a mainly cylindrical way until the exhaust side is reached. This happens when approximately 50% of

fuel mass is burned. At this point the distance to the intake side is still around 9 mm, but the flame moves into the squish zone located at the intake side. Here, the space between the cylinder head and the piston is small. When over 90% of the volume is burned, the flame arrives at the side wall. The intake wall is located furthest away from the spark plug. The same function is constructed for the piston in the TDC position as well as 2 and 4 mm down from TDC. These piston positions, x_p correspond to 19 and 27°CA relative to TDC respectively. For the same mass fraction burned the flame radius is larger when the piston is further away. However for the operating range of interest the differences remain small.

7.2 Thermal boundary layer influence

For knock to occur, two parameters are crucial: time and high temperature/pressure. For this reason cycles with, for example, a higher volumetric efficiency or a lower speed are more prone to knock. The shape of the combustion chamber can influence the knock behavior of an engine. When the flame travels large distances, much time is needed for the combustion and knock can be initiated in the end zone. The engine cooling system cools down the combustion chamber walls and reduces its surface temperature. This leads to a temperature gradient in the gases close to the walls, called the thermal boundary layer. The temperature of the gases in the thermal boundary layer is much lower than in the bulk unburned zone. The ignition delay time of the gases in the boundary layer is thus much higher. The occurrence of auto-ignition in this zone leading to knock is thus very improbable. Exceptions on this are local hot spots that can trigger ignition events. In crevices or other geometric shapes where the influence of the cold walls is strong, auto-ignition almost never occurs.

For knock modeling purposes the impact of the boundary layer needs to be quantified. In this section first a sensitivity study is performed to the amount of unburned fuel in the boundary layer zone, taking into account the geometry of the combustion chamber. In a second part a model for the thickness of the thermal boundary layer is introduced and in a last part different approaches to include the effect of the boundary layer into the knock model are presented.

7.2.1 Fraction of the unburned fuel in the boundary layer

Since the thermal boundary layer has an important influence on the knock behavior of an engine, it is of interest how much of the remaining fuel is enclosed in this boundary layer. Figure 7.3 shows the volume fraction of the unburned fuel within the boundary layer as a function of flame radius and mass fraction burned for different boundary layer thicknesses and piston positions. A fraction of 0.5, for example, means that of all the unburned gas, 50% is contained within the thermal boundary layer. Up to a flame radius of around 30 mm the fraction of the unburned gas in the boundary layer increases only slowly. This is before the flame reaches the exhaust side. During this time the flame propagates in a mainly cylindrical way. The boundary layers on the cylinder head and the piston are consumed at the same rate as the bulk mixture. The flame then moves close to the wall and the volume fraction contained within the boundary layer zone becomes significant and increases rapidly. Figure 7.3 gives an idea of the different boundary layer thicknesses. For a thickness of 3 mm almost all of the unburned gas is contained with the boundary. A boundary layer of 0.5 mm has around 20% of the unburned volume in the beginning of the combustion. The figure takes into consideration a two zone (burned and unburned) model for the temperature. As mentioned, the temperature within the boundary is lower than the bulk temperature. The effective mass fraction in the boundary layer is therefore higher than the volume fraction shown in the figure. The piston position has the highest influence for a thick boundary and reduces the unburned fraction in the boundary by removing the interaction of the piston and cylinder head layers. The most significant increase in the boundary layer mass fraction takes place when the flame moves into the squish area located at the intake side.

7.2.2 Thickness of the boundary layer

The thickness of the thermal boundary layer depends on the gas flow within the cylinder, the time available for the boundary layer to develop as well as the specific gas properties. Higher gas velocities promote the convective heat transfer and increase the boundary layer effect. When a long time range is available the thermal boundary layer can develop completely and is thicker.
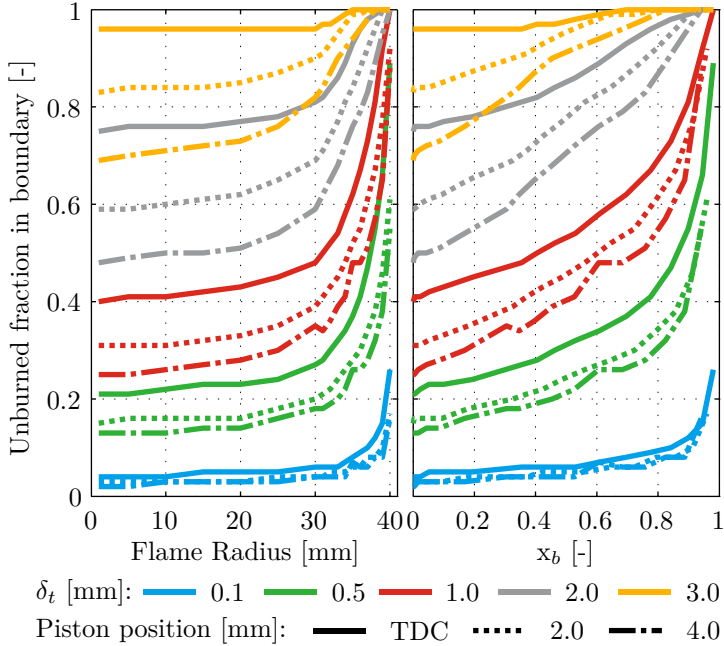
Figure 7.3: *Unburned volume fraction in the boundary as a function of flame radius, mass fraction burned, piston position and boundary layer thickness.*

Schlieren measurements for the thickness of the thermal boundary layer in an engine with optical access were performed by Lyford-Pike et al. [225]. They observed a growing boundary layer throughout the high pressure cycle. The boundary layer at the liner grows from the piston towards the cylinder head. The boundary layer is larger on the cylinder head and the piston compared to the liner. A model for the thermal boundary layer is derived based on the experiments, described by equations 7.2, 7.3 and 7.4, with a, the thermal diffusivity, ρ, the density, Re, the Reynolds number, μ, the viscosity, v_p, the piston velocity, v, the gas velocity, x, the distance between the piston and the cylinder head and x_0, the distance to the cylinder head.

$$\delta_T = 0.6Re^{0.2}\sqrt{at} \qquad (7.2)$$

$$Re = \frac{\rho v x_0}{\mu} \tag{7.3}$$

$$v = v_p \left(\frac{x_0}{x}\right) \tag{7.4}$$

7.2.3 Correction functions modeling the influence of the cylinder wall

In order to model the reducing probability of knock towards the end of combustion several correction functions can be applied to the knock integral as shown in equation 7.5. The correction function can have a value between 0 and 1, representing the conditions in which knock is impossible and the boundary layer has no influence respectively.

$$KI = \int \frac{f_{corr}}{\tau} dt \tag{7.5}$$

The knock integral method, presented in chapter 6, does not take into account the reducing probability of knock towards the end of the cycle. In this case the correction function takes the value of 1 at all time.

$$f_{corr} = 1 \tag{7.6}$$

A equation proposed by Laemmle [108] is given in equation 7.7. The idea of this equation is that with advancing combustion progress the remaining energy is reducing and thus the chances of auto-ignition are diminishing. The parameter β can shift the focus earlier of later in the cycle.

$$f_{corr} = (1 - x_b)^\beta \tag{7.7}$$

An equation based on the same idea, but inspired on the Wiebe combustion model [226] is given in equation 7.8. The equation has two shape parameters. Parameter b shifts the function earlier or later in the cycle; parameter m_v determines the steepness of the function.

$$f_{corr} = exp\left(-6.9 \cdot (b \cdot x_b)^{m_v}\right) \tag{7.8}$$

Both equations include the same concept introduced by Franzke [227], who also observed the reducing probability of knock towards the end of combustion. An application of the concept is presented in [105]

in which existing auto-ignition delay time correlations are implemented in a predictive knock model. The knock criterion is an Arrhenius type integral with the knock probability zero after a certain crank angle window. However the chosen window is hardly linked to the physical process.

A last option under consideration to model the reducing probability of knock due to the growing influence of the colder walls is to formulate a correction function based on the fraction of unburned fuel in the thermal boundary layer zone. Figure 7.3 shows the volume fraction of the unburned fuel in the thermal boundary layer, $V_{u,th}$. To obtain the mass fraction of the unburned gas within the boundary layer, $x_{u,th}$ the temperature of the boundary layer, T_{bound}, needs to be determined. As an approximation the mean temperature of the wall and the bulk unburned gas can be used. The temperature of the walls is available as results from the thermodynamic analysis. The mass fraction of the unburned gas in the boundary is a function of the temperature ratio and $V_{u,th}$, as shown in equation 7.9.

$$x_{u,th} = \left(\frac{T_{bound}}{T_u} \cdot \left(\frac{1}{V_{u,th}} - 1 \right) + 1 \right)^{-1} \tag{7.9}$$

Due to the much lower temperature in the thermal boundary layer, auto-ignition in this area is highly unlikely. Once the mass fraction of the unburned fuel in the thermal boundary is high enough, the probability of auto-ignition of the unburned fuel not in the boundary becomes small as well. A correction function can be based on this assumption. When the mass fraction in the boundary is higher than a certain threshold value, $x_{u,th,thr}$, the correction function becomes zero, as shown in equation 7.10.

$$f_{corr} = \begin{cases} 1 & \text{if} \quad x_{u,th} < x_{u,th,thr} \\ 0 & \text{if} \quad x_{u,th} \geq x_{u,th,thr} \end{cases} \tag{7.10}$$

8 Results and discussion

Chapters 2 to 7 describe the test bench setup, the measurements and the methodologies to study and model knock. In this chapter the methodologies are applied to the obtained data and the impact of the results are discussed. The first section shows the results of the measurement campaign and the thermodynamic analysis. The second section discusses the differences in the knock behavior between the two fuels and a cycle-statistical analysis. In the third and fourth section the comparison of the knock models for iso-octane and ethanol respectively are presented. A last section deals with the influence of the cylinder walls on the knock tendency and how to include this behavior in the knock model.

8.1 Results of the measurements

As mentioned in section 2.5, knock measurements are carried out for ethanol and iso-octane. The same set of measurements is carried out for both fuels, with the difference that the injection for ethanol is DI and for iso-octane PFI is used. Spark angle variations for constant intake temperatures and speeds are recorded. The measured torque for all operating points can be seen in figure 8.1 as a function of speed, intake temperature and spark timing. The dashed lines correspond to the ethanol measurements and the full lines are for iso-octane. The torque results show the typical parabolic shape related to spark time variations. However the measured torque for ethanol is much higher compared to that of iso-octane at nominally the same operating point. The difference can mainly be attributed to the latent heat of vaporization. As explained in section 2.1, the evaporation of ethanol cools down the mixture much more than is the case for iso-octane. When all
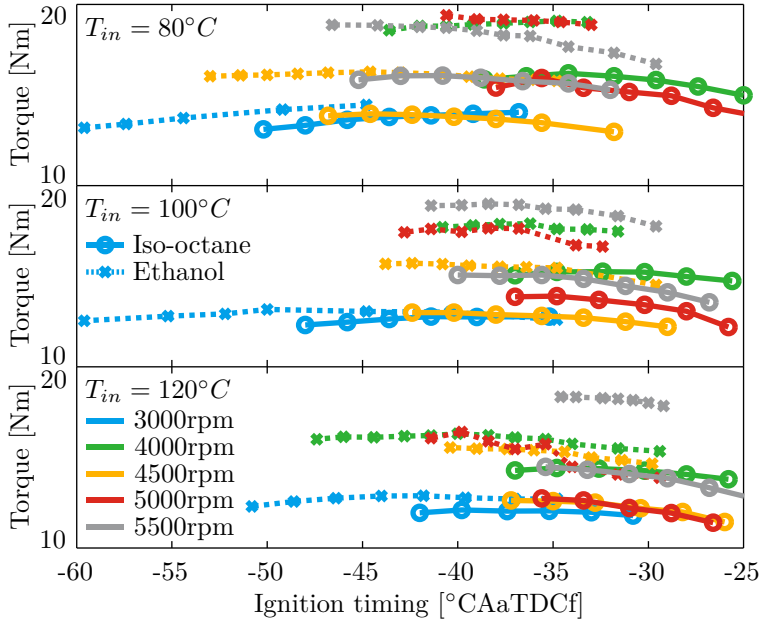
Figure 8.1: *Torque as a function of spark advance for iso-octane (PFI) and ethanol (DI) at different speeds and intake temperatures.*

the required heat is taken from the incoming air, the mixture is cooled by more than 100 °C. This effect is much stronger for direct injection than for PFI. The PFI injector is installed before the cylinder head, so significant wall wetting can be expected. With increased wall wetting the evaporation heat, taken from the intake piping, is higher, leading to a lower cooling effect. The ethanol measurements benefit from both the higher latent heat of vaporization and the direct injection system. The stronger cooling effect leads to a higher charge density and thus a higher volumetric efficiency and consequently a higher torque production for the same operating point. There is no clear dependency of the charge cooling effect on speed. At 5500 rpm the effect is strong; at 3000 rpm the effect is much lower.

Figure 8.2 shows the air mass flow for the ethanol measurements relative to that of the iso-octane measurements. Only one data point is shown per speed and intake temperature, since the air mass flow does not change significantly for different spark timings. It can be seen
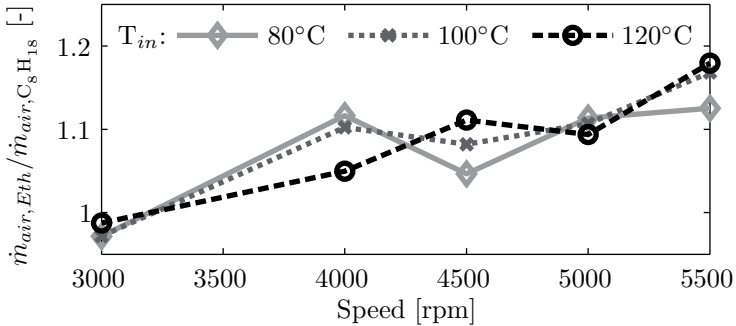
Figure 8.2: *Ratio of air mass flow between ethanol and iso-octane due to evaporative cooling for different speeds and intake temperatures.*

that the air mass flow for the ethanol operating points is higher than for iso-octane and the difference in volumetric efficiency increases with increasing speed. This can be attributed to higher turbulence levels and a higher fraction of the energy, needed to evaporate the fuel, is taken from the fresh charge. The intake temperature does not play a large role in this effect.

Due to the large difference in volumetric efficiency between ethanol and iso-octane, a direct comparison of the two sets of measurements can be misleading. As a consequence of the cooling effect of ethanol, the temperatures during the combustion cycle are overall lower for this fuel. Figure 8.3 shows the exhaust temperatures for both fuels for T_{in}=120°C. The exhaust temperatures increase for later spark timings, as can be expected. The overall exhaust temperatures are lower for ethanol compared to those for iso-octane.

Section 2.1 compares the laminar flame speeds of ethanol and iso-octane and suggests that ethanol burns faster. This is however the case for the same thermodynamic conditions and the same level of turbulence. The previous analysis suggests overall lower temperatures for ethanol, which would result in lower flame speeds and consequently slower combustion. The measurement data are used to complete the thermodynamic analysis as described in chapter 3, yielding amongst others the two-zone combustion temperatures and the heat release rates for both the mean and single cycles. This allows for a comparison of the combustion duration between ethanol and iso-octane for the same operating points. Figure 8.4 shows the combustion duration between
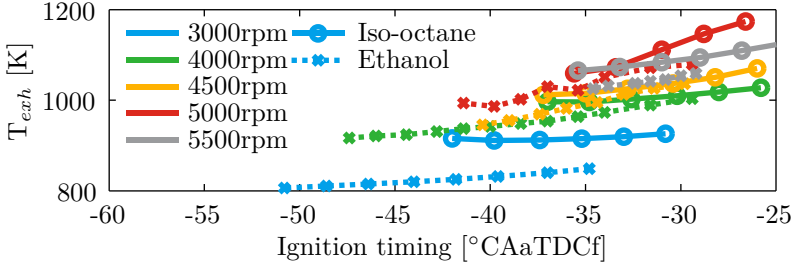
Figure 8.3: *Exhaust temperature as a function of spark advance for iso-octane (PFI) and ethanol (DI) at different speeds and for $T_{in}=120°C$.*
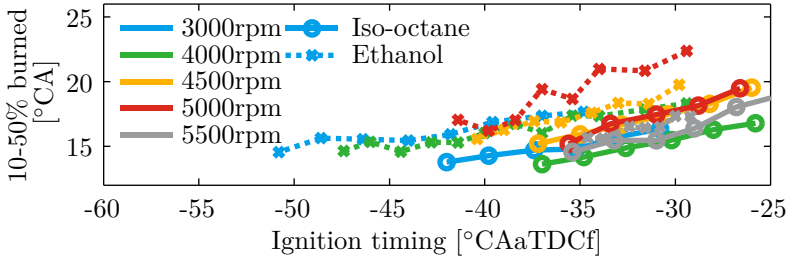
Figure 8.4: *Combustion duration between 10 and 50 % burned mass fraction as a function of spark advance for iso-octane (PFI) and ethanol (DI) at different speeds and for $T_{in}=120°C$.*

10 and 50 % mass fractions burned as a function of speed, intake temperature and spark timing. As expected, later spark timings lead to slower combustion and longer burn durations. For nominally the same operating point the combustion of ethanol is slower than that of iso-octane. This confirms the assumption about the lower flame speed due to lower combustion temperatures.

In order to get a better distinction of the different effects on the combustion speed, the analysis of equation 2.13 is carried out. The signature flame front area is determined based on the measurement data set. The heat release rate and the unburned and burned densities are available from the thermodynamic analysis. The flame front area is that of a smooth flame and is only a function of the piston position and the mass fraction burned (not of the fuel). The turbulence is contained
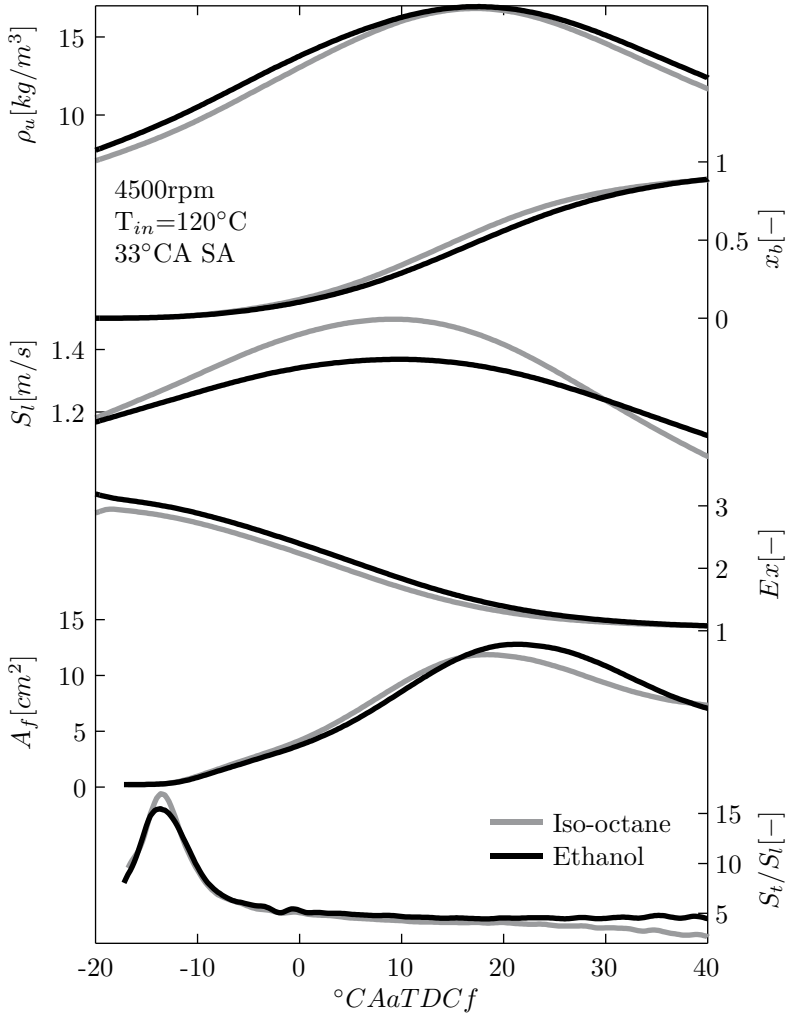
Figure 8.5: *Unburned density, mass fraction burned, laminar flame speed, expansion factor, flame area and turbulent to laminar flame speed ratio of ethanol and iso-octane based on eq. 2.13-2.15 for an example operating point (4500rpm, $T_{in}=120°C$, 33° CA SA).*

in the turbulent flame speed, which can be calculated from the other known values. The laminar flame speed for both fuels can be modeled using the correlations presented in section 2.1: Liao et al. [81] for ethanol and Metghalchi et al. [87] for iso-octane. Figure 8.5 shows exemplarily the results of this analysis for one operating point when comparing ethanol and iso-octane. The density of ethanol is higher over the complete cycle, which is in agreement with the observations in figures 8.2 and 8.3. The mass fraction burned for ethanol lags that of iso-octane, as observed in figure 8.4. The laminar flame speed of iso-octane is higher, due to the higher temperatures. The flame area for iso-octane is larger in the first half of the cycle and smaller in the second half due to the faster combustion. The maximum flame area is higher for ethanol because the maximum flame is reached later in the cycle when the cylinder volume is larger. The expansion factor for ethanol is slightly higher mainly due to the higher density ratio. The bottom plot in figure 8.5 shows the ratio of the turbulent flame speed, as calculated from equation 2.13 to the modeled laminar flame speed, using the correlations, over the cycle for the given operating point. This ratio is a measure for the turbulence. The difference between the fuels is small. Therefore it is valid to assume that there is no significant difference in turbulence resulting from the different injection modes. The slower flame speed for ethanol is effectively due to the cooling effect of the evaporation and the overall lower temperatures. The longer combustion duration is a combination of the higher density and lower flame speed for ethanol compared to iso-octane for the same operating point.

8.2   Knock detection methods

In chapter 4 an overview of knock indices and knock detection methods, available in literature, is given and a criterion for knock detection has been derived. This section presents the results of the application of this knock criterion to the measurement data. In a first subsection the knock detection criterion is applied to all the single and mean cycles. In a further subsection the results for the onset of knock timing are given. Based on this knock criterion a cycle-statistical analysis is presented in a third and last subsection.
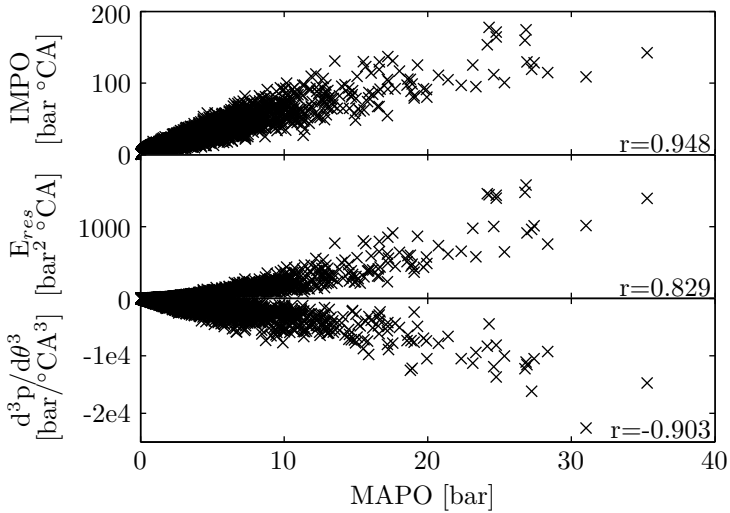
Figure 8.6: *Comparison of knock indices MAPO (eq. 4.2), IMPO (eq. 4.3), E_{res} (eq. 4.6) and 3rd derivative of pressure for all single cycles in all operating points, including the correlation coefficients, r, between the different indices.*

8.2.1   Knock indices and knock detection algorithms

In section 4.1.1 several knock indices, mainly based on the in-cylinder pressure trace, are introduced. Figure 8.6 shows the correlation of the different knock indices for all the single cycles in the measurement set. The correlation coefficients are high, showing a good agreement between the different indices. It suggests that MAPO is a good method as a basis of the knock detection criterion.

The derivation of the knock detection criterion, in which the value of $MAPO_{rel}$ is used as threshold for the knocking cycles, is introduced in section 4.2. The MAPO value of a cycle is compared to the MAPO value of the cycles at late spark timings. For a value higher than 4, the cycle is considered a knocking cycle. When more than 5% of the cycles knock, the operating point is considered a knocking operating point. The results for all operating points can be seen in figure 8.7. The figure shows the $MAPO_{95}$ value as a function of speed, intake temperature and
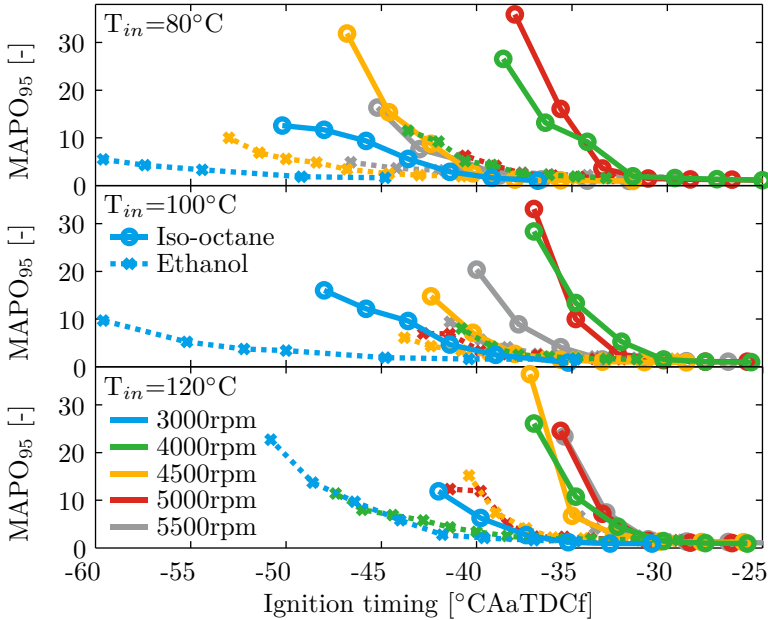
Figure 8.7: *Knock intensity index MAPO$_{95}$ as a function of spark advance for iso-octane (PFI) and ethanol (DI) at different speeds and intake temperatures.*

spark timing for both ethanol and iso-octane. As expected, earlier spark timings lead to an increase of the knock intensity. Due to the much better knock resistance and the overall lower temperatures, as explained in section 8.1, the MAPO$_{95}$ values are consistently lower, in nominally the same operating point, for ethanol compared to iso-octane. The spark timing at which the MAPO$_{95}$ value reaches a value of 4 is referred to as the knock limited spark timing (KLST) and is a measure for the tendency of an operating point to knock. The figure shows a later KLST for higher intake temperatures. Higher intake temperatures increase the overall combustion temperatures and therefore reduce the auto-ignition delay times. The effect of speed on the KLST is not uniform in the figure. For auto-ignition to occur both the availability of time and high pressures and temperatures are required. Lower speeds increase the available time and should lead to a later KLST. Peak temperature and pressure increase with the load, leading to lower ignition delay

times. The volumetric efficiency changes significantly with speed. At the lowest speed, 3000 rpm, the available time is highest, however the volumetric efficiency is very low compared to the other operating points. At this speed the knock indices are lowest. The combination of available time and high volumetric efficiency for this engine is optimal at 4000 and 5000 rpm, which results in the latest KLST and the highest knock tendency.

The MAPO$_{95}$ values for iso-octane in the measurement set are higher than those for ethanol. The total number of knocking operating points is higher for iso-octane. Also within the operating point more knocking cycles are recorded. The relative number of knocking cycles for iso-octane is thus much higher compared to the data set for ethanol.

8.2.2 Onset of knock timing

When an engine cycle is detected as a knocking cycle, based on the relative amplitude of the pressure oscillations, it is of great interest to know when exactly in the cycle knock is initiated. In section 4.2.2 different possible criteria for the determination of the start of knock are introduced: SOK p$_{lim}$, SOK p$_{max}$ and SOK HRR. Figure 4.5 shows the timing for the different criteria for two example cycles: one with strong knock and one with borderline knock. The SOK HRR criterion precedes the SOK p$_{lim}$ and the SOK p$_{max}$ criteria. The results of an application of the three criteria on an example operating point can be seen in figure 8.8. The timing for the onset of knock is given for both the SOK p$_{max}$ and the SOK HRR criteria and are compared to the SOK p$_{lim}$ criterion in terms of degree CA (top) and mass fraction burned (bottom). The dashed black line shows the 1:1 timing. This means that points above this line are later than the SOK p$_{lim}$ timing, points below are earlier. For all knocking points, the SOK p$_{max}$ criterion is later than the SOK p$_{lim}$ criterion. This is per definition the case. In cycles at borderline knock (MAPO$_{rel}$ value close to 4) the location of SOK p$_{max}$ is very close to SOK p$_{lim}$. For stronger knocking cycles the maximum amplitude can occur later in the cycle. The SOK HRR criterion always precedes the SOK p$_{lim}$ criterion. This means that there is a heat release preceding the pressure oscillations corresponding to the auto-ignition of the mixture in front of the flame. The corresponding fast reactions produce the typical pressure oscillations. For the given operating point the mean difference between SOK p$_{max}$ and SOK p$_{lim}$
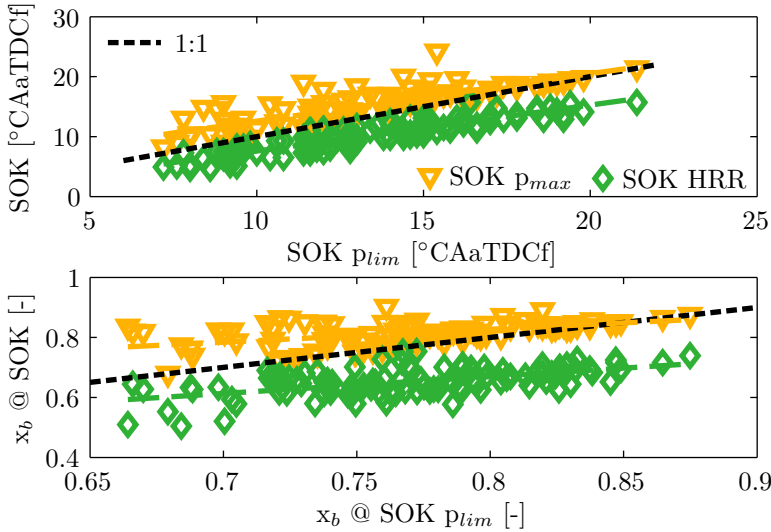
Figure 8.8: *Comparison of three start of knock timing criteria (max, lim and HRR) for one operating point (4500 rpm, T_{in}=80° C, 45.00° CA SA, iso-octane) as a function of degree crank angle (top) and mass fraction burned (bottom).*

is 1.88°CA, which corresponds to 4.43% x_b. The difference between SOK HRR and SOK p_{lim} is 3.21°CA corresponding to 11.69% x_b. The relatively small difference in terms of degree crank angle adds up to a large difference in mass fraction burned. Later SOK p_{lim}typically means also a later SOK HRR, but there is no apparent correlation for the distance between the SOK HRR and SOK p_{lim} criteria. The amplitude of the pressure oscillations and its timing a function of the location of the pressure sensor. Depending on where the auto-ignition is initiated, the timing for the maximum pressure oscillation can be different.

From this analysis it is apparent that the only correct criterion for the timing of the onset of knock is the SOK HRR criterion. This criterion is used for the following results unless explicitly mentioned otherwise. The knock criterion for a single cycle is a combination of the detection based on the relative amplitude of the pressure oscillations and the timing for the onset of knock, determined using the heat release

corresponding to the auto-ignition. In this way the detection is based on the effect of knock (the pressure oscillations) and the timing is set by the cause (the heat release corresponding to the auto-ignition).

8.2.3 Cycle statistical analysis

The question arises which of the cycles, within one operating point, are the ones that knock. The cycle-to-cycle variations play a major role in the knock phenomenon. For the same nominal operating point several cycles have strong pressure oscillations and other cycles show no signs of auto-ignition. This subsection deals with the investigation what parameters are decisive in obtaining a knocking cycle.

Within the same operating point, the spark timing is constant. The crank angle at which 50% of the fuel mass is burned is thus a measure for the combustion speed of the single cycle. Figure 8.9 shows the $MAPO_{rel}$
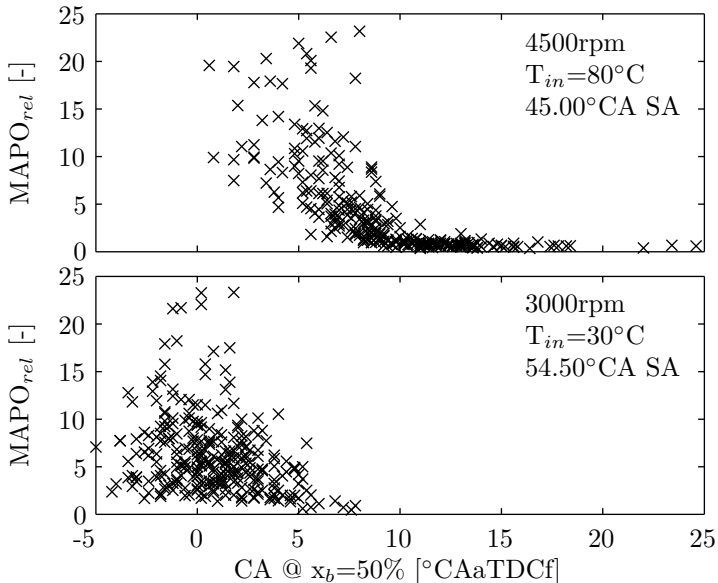
Figure 8.9: *Knock index $MAPO_{rel}$ as a function of the 50% burned angle for all the cycles in two different operating points: 4500 rpm, $T_{in}=80°C$, 45.00° CA SA (upper) and 3000 rpm, $T_{in}=30°C$, 54.50° CA SA (lower), iso-octane.*

value against the crank angle at x_b=50% for two operating points. The operating point in the upper graph has the later ignition timing and stronger knock intensity. For this case the slowest burning cycles have a low knock index and do not knock. With increasing combustion speed, the knock intensity increases. Faster burning cycles reach higher pressures and temperatures leading to lower ignition delay times and stronger knock. The second operating point shows a different behavior. The cycles with the highest knock intensity are not necessarily those with the fastest combustion, but there is a maximum of the knock intensity for cycles with x_b=50% around TDC. Cycles that burn faster than this do not have the time that is required for auto-ignition to occur and no pressure oscillations are produced.

Figure 8.10 shows the effect of spark timing on the onset of knock with a histogram of the mass fraction burned at the timing for the onset of knock. The operating point with the latest spark timing has the lowest knock intensity and thus the lowest number of knocking cycles. As the spark timing is advanced, the knock intensity increases and more cycles knock. The mean value of the mass fraction burned at the onset of knock is shown as a vertical dashed line. As the spark timing is moved forward the pressure rise during the first phase of the combustion becomes steeper, which leads to higher pressures and temperature (and thus low ignition delay times) early in the cycle and
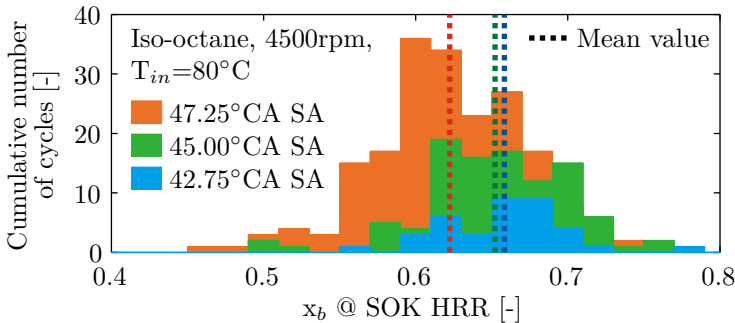
Figure 8.10: *Histogram of the mass fraction burned at the onset of knock for the cycles within three operating points with different spark timings. Operating points: 4500 rpm, T_{in}=80° C, 47.25, 45.00, 42.75 °CA SA, iso-octane. Vertical dashed lines indicating the mean value of all knocking cycles within that operating point.*
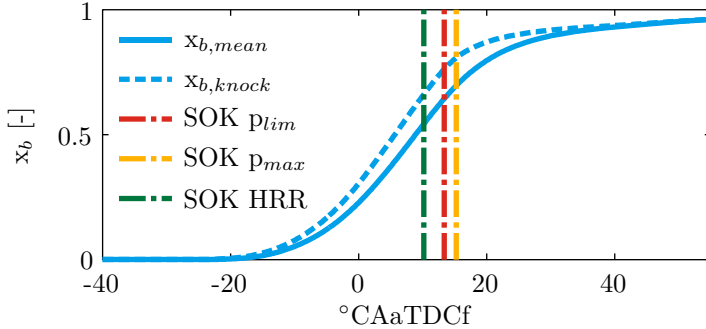
Figure 8.11: *SOK criteria for x_b in the overall mean cycle ($x_{b,mean}$) and the mean of all knocking cycles ($x_{b,knock}$). Operating point: 4500 rpm, T_{in}=80° C, 45.00 °CA SA, iso-octane.*

knock is initiated at a lower mass fraction burned.

Figure 8.11 displays for an example operating point the mass fraction burned for the overall mean cycle, $x_{b,mean}$, and the mean knocking cycle, $x_{b,knock}$ and shows that the average knocking cycle is faster than the overall mean cycle. The timing for the different SOK criteria is obtained by averaging the SOK timing for all knocking operating points. For the SOK HRR criterion the difference between the overall mean cycle and the mean knocking cycle is 11.81 % of fuel mass burned. In the mean knocking cycle the flame is much further advanced compared to the overall mean cycle.

This is true for all recorded operating points: at the timing of the onset of knock the mass fraction burned of the average knocking cycle is higher than that of the overall mean cycle. With lower values of $x_{b,mean}$ at the start of knock, the difference between the overall mean and average knocking cycle increases. This does not necessarily mean that knock is initiated earlier in the knocking cycles. The cycle-to-cycle variations are larger for these operating points and the overall mean cycle is slower.

Figure 8.12 shows the mass fraction burned at the onset of knock in the mean of all knocking cycles for both ethanol and iso-octane. For ethanol knock is initiated earlier in the cycle compared to iso-octane. This is mainly because the operating points at which ethanol knocks are different from those for iso-octane. Ethanol needs much earlier spark timings to obtain a knocking operating point. As discussed in
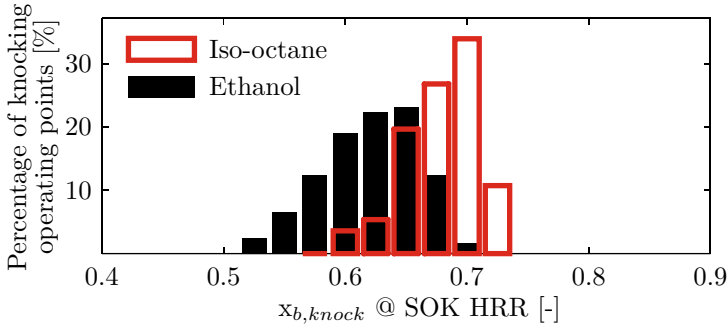
Figure 8.12: *Mass fraction burned at knock onset in the mean of all knocking cycles ($x_{b,knock}$) for all operating points that knock for ethanol and iso-octane.*

figure 8.10, earlier spark timings lead to auto-ignition occurring at much lower mass fractions burned. Almost all of the cycles start to knock at mass fractions burned between 50 and 70 %. Knock is never initiated when less than half of the fuel is burned. During the first half of the combustion, temperature and pressure need to build up and the required time is not available to auto-ignite the mixture. On the other hand, when more than 70 % of the fuel is burned knocking combustion becomes very unlikely, even though the time would be available.

8.3 Knock models for iso-octane

After the analysis of the measurement results, the goal is to derive a knock model that is able to correctly predict the timing for the onset of knock. In a first step the selected knock models, presented in section 6.2, are applied to the measurement data and the fitness functions are computed for iso-octane. The influence of the ignition delay time equation is shown and the results are presented for the mean and the single cycles.

8.3.1 Influence of the ignition delay time equations

Two knock integral formulations and four ignition delay time correlations in all together five knock models are selected for iso-octane (table

6.1). The ignition delay time correlations are a function of composition, pressure and temperature. These parameters are available from the thermodynamic analysis. The ignition delay time in the unburned mixture can be calculated for each of the correlations.

The results for an example operating point are shown in figure 8.13.
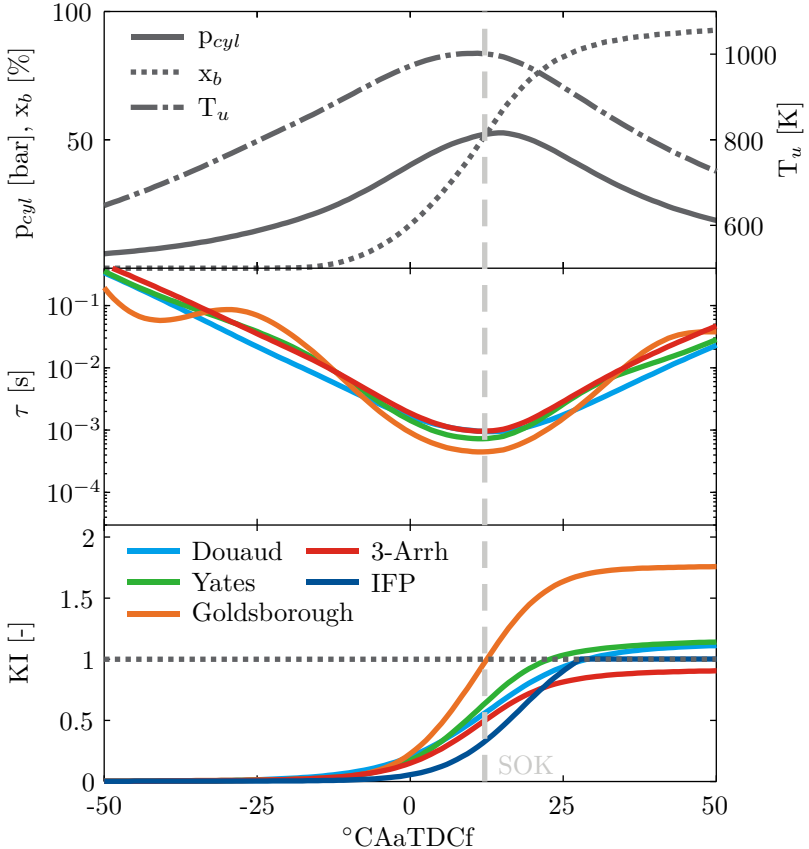
Figure 8.13: *Pressure, unburned temperature, mass fraction burned, ignition delay times and KI for the selected knock models (Douaud, Yates, Goldsborough, 3-Arrh and IFP - see table 6.1) for iso-octane and operating point 5000 rpm, T_{in}=120° C, 36.00 °CA SA including the start of knock (SOK HRR) timing.*

The upper graph shows the measured pressure and the unburned temperature and burned mass fraction from the thermodynamic analysis for the mean cycle. The pressure and temperature data are used to calculate the ignition delay times in the four different correlations and the progress throughout the cycle is shown in the middle graph. The results correspond to the observations made in figure 5.5. The Douaud equation consists of only a single step Arrhenius and thus yields an average value of the ignition delay time with relatively low values at low temperatures and high values at high temperatures. The 3-Arrhenius approach and the Yates correlation are both derived from the same chemical kinetic model and thus produce a similar behavior, with slightly lower values for the Yates correlation. The most pronounced two-stage behavior can be seen for the Goldsborough equation. The pressure coefficient is much higher for the Goldsborough correlation compared to the other correlations, following closer the shock tube measurement data and producing the lowest value of all around peak cylinder pressure.

The graph on the bottom of figure 8.13 shows the values of the knock integral, KI, for the different knock models as a function of degrees crank angle. When the knock integral reaches a value of 1, the knock model predicts the onset of knock at this point. The operating point under consideration is defined as knocking by the criterion derived in chapter 4. The vertical dashed line denotes the timing for the onset of knock. The Goldsborough correlation has the lowest ignition delay time, particularly in the area around peak pressure, integrates KI the fastest and the knock prediction is very accurate for this operating point. The 3-Arrhenius approach has the highest ignition delay time and integrates the slowest. The KI value never reaches a value of 1 and thus the 3-Arrhenius approach does not predict knock. Both the Yates and Douaud correlations predict knock, however too late in the cycle. The IFP model uses the Douaud correlation for the ignition delay time, but has a different integration method. The prediction for the timing of the onset of knock is similar to the Douaud model, however the integration is slower at first.

8.3.2 Evaluation of the knock models for the mean cycles

In figure 8.13 the selected knock models are applied to one example operating point to illustrate the different ignition delay time equations and knock integrals. The knock models can now be applied to all

mean cycles of the gathered data. For the mean cycle the pressure and unburned temperature are averaged over all cycles within one operating point. The SOK timing is the average timing for all knocking cycles. The results of the knock models are evaluated using the fitness functions presented in section 6.3.

Figure 8.14 shows the results of the knock models applied to all mean cycles for iso-octane, one graph per model. On the left side the end value of KI is shown versus the $MAPO_{95}$ value as determined by the experiment. Two dashed lines are drawn. The horizontal line depicts the border of knock as predicted by the model. A KI_{end} value higher than 1 results in knock prediction by the model. A value lower than 1 predicts a non-knocking operating point. The vertical line depicts the border of knock as determined by the experiment. A $MAPO_{95}$ value higher than 4 corresponds to a knocking operating point; a value lower than 4 denotes a regular operating point. Correct predictions lie in the upper right and lower left quadrants and are marked in blue. Incorrect predictions lie in the upper left (knock predicted in a non-knocking operating point) and in the lower right (no knock prediction for a knocking operating point) and are marked in red. On the right hand side of the graph the KI value at SOK is shown versus the $MAPO_{95}$ value from the experiment only for the knocking operating points. This graph shows whether knock prediction comes too early or too late.

The Douaud model yields a good prediction of the knocking operating points. Many of the non-knocking operating points are however predicted incorrectly. Since the KI values at SOK are all lower than 1, the prediction of the timing for the onset of knock is too late for all operating points. A similar observation can be made for the IFP model: a relatively good prediction of the knocking operating points, however too late. Most of the incorrect predictions are non-knocking cycles. The 3-Arrhenius model yields the highest ignition delay times. Many of the knocking operating points are therefore predicted incorrectly, as is the case in the example of figure 8.13. Consequently the KI values at SOK are even lower than for the Douaud and IFP models. The Yates model gives results between the Douaud and 3-Arrhenius models. The Goldsborough model has the lowest ignition delay time, especially for higher pressures, therefore both the KI_{end} and KI_{SOK} values are higher. All knocking cycles are predicted correctly with KI_{SOK} values much closer to 1. Many of the non-knocking cycles are however predicted incorrectly as knocking in the upper left quadrant.

The values for both fitness functions reflect the previous analysis of
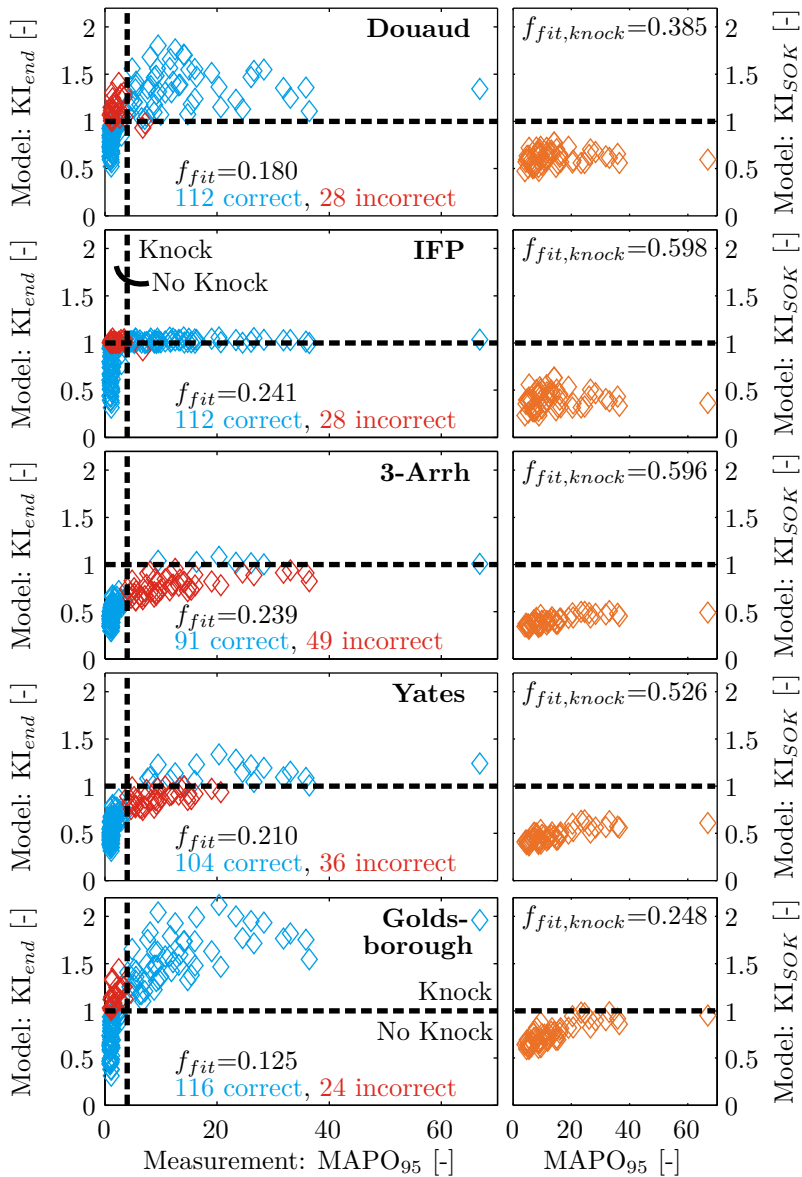
Figure 8.14: *Knock model KI value at end of cycle and at SOK versus MAPO$_{95}$ from measurements for mean cycles with iso-octane.*

the results. The fitness function for the knocking cycles reflects how well the model predicts the timing for the onset of knock. The closer the KI_{SOK} values to 1, the lower the fitness function. The Goldsborough correlation predicts best the timing for the onset of knock and therefore has the lowest value for $f_{fit,knock}$. The overall fitness function, f_{fit}, also takes into account the non-knocking cycles. Not only the number of incorrect predictions is decisive for the fitness function value, also how far the prediction is off. The IFP and 3-Arrhenius models result in the worst fitness function; the Goldsborough equation gives the best results.

8.3.3 Evaluation of the knock models for the single cycles

In the previous subsection the knock models are tested using the mean cycle values. According to the knock detection method, defined in chapter 4, an operating point knocks when at least 5% of the cycles are knocking. Using the mean cycle for the evaluation of a knock models is useful in order to understand the differences between the different models. Each cycle within one operating point has its own pressure and temperature trace and for a correct representation the knock model should be evaluated for each cycle individually. Even though within an operating more than 5% of the cycles knock, it is possible that a cycle with the same temperature and pressure trace as the mean cycle would not be a knocking one. A knock model can only predict for a single cycle whether and when it will knock and does not consider the cycle-to-cycle variations within an operating point.

Figure 8.15 shows the results of the application of the five selected knock models to the complete set of single cycles for the iso-octane measurements. The figure shows histograms for the knocking and non-knocking cycles, as determined by the experiments. The KI values at the timing for the onset of knock are shown in full orange. A knock model should predict a KI value of 1 at the timing for the onset of knock. Similar to the observations made in figure 8.13, the ignition delay time correlations of Douaud and Yates as well as the 3-Arrhenius approach have KI values at the timing of the onset of knock that are too low and either there is no knock prediction for the cycle or the prediction is too late in the cycle. The knock model that uses the Goldsborough correlation has a distribution of KI_{SOK} around 1, which corresponds to more accurate predictions for the timing of knock. This is reflected
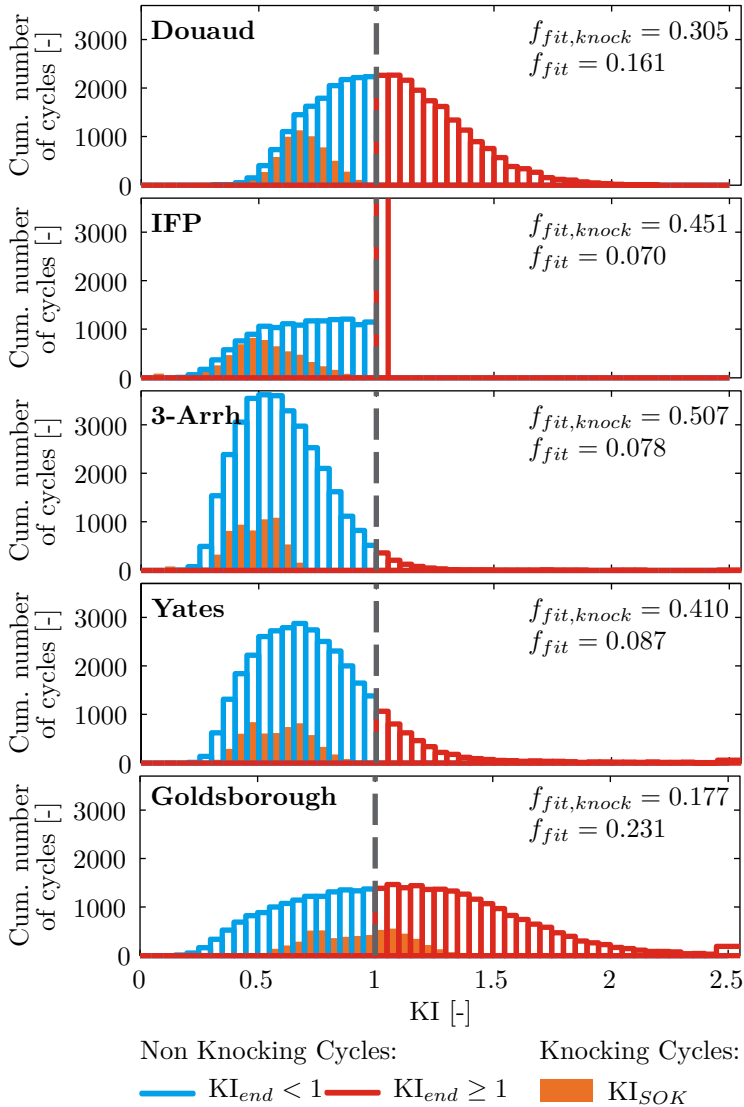
Figure 8.15: *Knock model results for the single cycles. Histogram of knock model KI value at end of cycle for non-knocking cycles: correct predictions in blue, incorrect predictions in red. Histogram of KI value at SOK timing for the knocking cycles.*
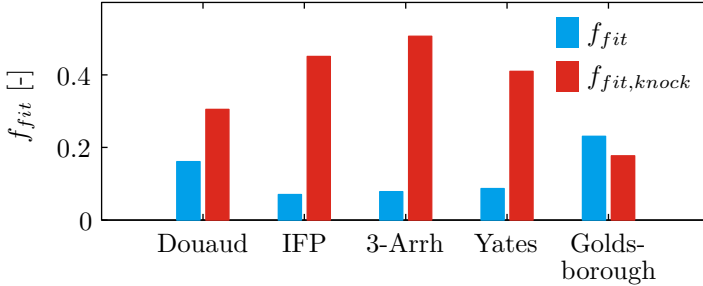
Figure 8.16: *Fitness function values (eq. 6.8 and 6.9) for knock prediction evaluation for all single cycles in the Douaud, IFP, Yates, Goldsborough and 3-Arrhenius knock models (see table 6.1).*

in the lower value for $f_{fit,knock}$. Most of the cycles are however non-knocking cycles. The values for KI at the end of the cycle, KI_{end}, are depicted by the blue and red lines. A cycle is correctly predicted as a non-knocking cycle, when the KI value never reaches 1. These cycles are shown in blue. The Yates correlation and 3-Arrhenius approach have the best predictions for the non-knocking cycles, because they have the highest ignition delay time values. However, as mentioned, the values for KI_{SOK} are too low. The IFP model cannot produce values higher than 1, due to its specific formulation, and has, as well as the Douaud and Goldsborough models, a large number of incorrect predictions of the non-knocking cycles. A summary of the fitness function values is shown in figure 8.16 and corresponds to the observations made: The Goldsborough model yields the best prediction for the timing of the onset of knock, but has a high overall fitness function due to the many incorrectly predicted non-knocking cycles.

8.4 Knock models for ethanol

For ethanol four different knock models are selected using three ignition delay time equations and two knock integral formulations in accordance with section 6.2. An analysis similar to that for iso-octane is presented here for ethanol. In a first subsection the influence of the different ignition delay time equations is discussed. Then the knock models are applied to the mean cycle and in a last subsection to all single cycles.
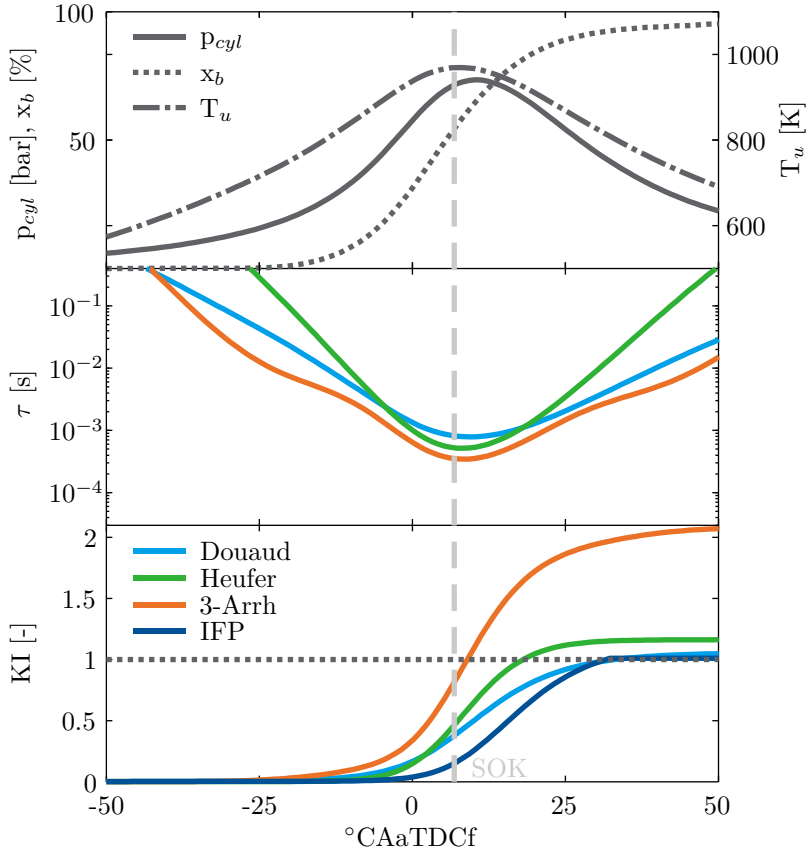
Figure 8.17: *Pressure, unburned temperature, mass fraction burned, ignition delay times and KI for the selected knock models (Douaud, Heufer, 3-Arrh and IFP - see table 6.2) for ethanol and operating point 5500 rpm, T_{in}=80° C, 47.25 ° CA SA including the start of knock (SOK HRR) timing.*

8.4.1 Influence of the ignition delay time equations

For a representative example operating point the pressure, unburned temperature, mass fraction burned, the ignition delay times in the three selected correlations and the KI values for the four knock models for ethanol are shown in figure 8.17. Corresponding to figure 5.6, the

Heufer equation has the highest ignition delay time for the low temperature range i.e. in the beginning and at the end of combustion. The correlation is not validated for this operating area and is therefore unreliable in this range. The other single step Arrhenius equation, the Douaud correlation, computes lower ignition delay times in the low temperature range. The temperature coefficient is however much smaller and the ignition delay time values are higher in the high temperature area, despite the stronger pressure influence. The 3-Arrhenius approach based on the Cancino chemical kinetic mechanism takes into account the lower ignition delay times observed at low temperatures. This correlation produces the lowest ignition delay times over the whole cycle. The unburned temperature for the example stays lower than 1000 K. It is only at temperatures above 1000 K that the Heufer correlation can compute lower ignition delay times than the 3-Arrhenius approach.

All four knock models predict knock for the given operating point. The lowest value for the ignition delay time is often decisive in the knock integral due to the logarithmic scale of the Arrhenius equation. The Douaud correlation integrates to the lowest KI value and predicts knock almost 20°CA too late. Similar to the example for iso-octane, the IFP model also has a slower start in this example for ethanol. The predicted timing for the onset of knock is again very close to that of the Douaud model. The KI profile for the Heufer model starts off slower, but eventually predicts the onset of knock earlier than the Douaud model, in accordance with the ignition delay time profiles. The 3-Arrhenius approach predicts knock very close to the experimentally determined timing for the onset of knock. The orange line crosses the KI=1 line not much after the SOK line.

8.4.2 Evaluation of knock models for mean cycles

In the previous subsection the 3-Arrhenius approach obtained the best knock prediction. The four knock models are now applied to the mean cycle data, in a similar way as has been done in section 8.3.2, to assess the performance of the different models for all operating points. Figure 8.18 shows the KI value at the end of the cycle versus the $MAPO_{95}$ value, as determined by the experiments on the left side and the KI value at SOK on the right side. The tendencies observed in the example operating point in figure 8.17 are confirmed. The KI_{end} values are too low for many of the knocking operating points, when using the Douaud model. Most of the non-knocking cycles are predicted cor-
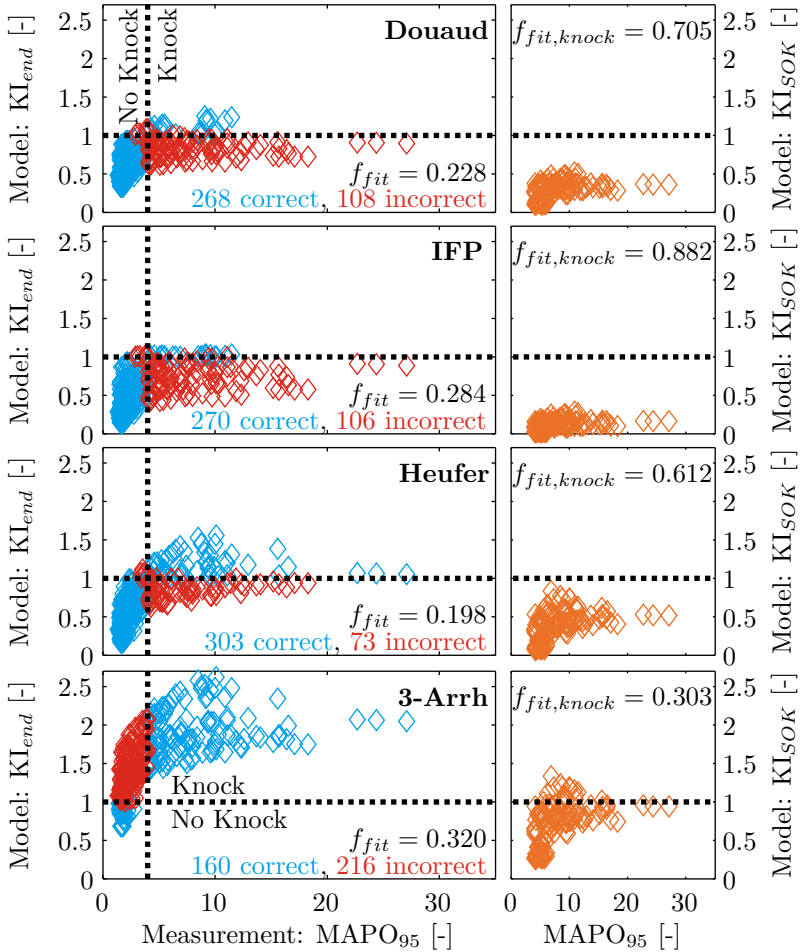
Figure 8.18: *Knock model KI value at end of cycle (left) and at SOK (right) versus MAPO$_{95}$ from measurements for mean cycles with ethanol.*

rectly. In line with these results, the KI values at SOK are too low. This results in a knock prediction too late in the cycle, when there is correct knock prediction. A similar trend is observed for the IFP model with even lower values for KI_{end} and KI_{SOK}. The Heufer correlation computes lower ignition delay times than the Douaud correlation in the intermediate temperature range and therefore yields overall higher KI values. Also correct knock predictions with the Heufer equation are too late in the cycle for all available operating points. The total number of correct predictions is higher compared to the Douaud and IFP models. The 3-Arrhenius approach has the lowest number of correct predictions, because many of the non-knocking cycles have KI values higher than 1 at the end of the cycle. All of the knocking cycles are predicted correctly with KI values at the end of the cycle mostly even higher than 1.5. The KI values at SOK are much better compared to the three other models and are distributed around 1. The timing for the onset of knock is predicted best by the 3-Arrhenius equation. The observed results are reflected in the fitness function values. The overall fitness function, f_{fit}, is lowest for the Heufer model, a bit higher for the IFP and Douaud models and worst for the 3-Arrhenius model. The best fitness function for the knocking operating points, $f_{fit,knock}$, is achieved by the 3-Arrhenius model. In accordance with the computed ignition delay times the results deteriorate in the sequence Heufer, Douaud and IFP.

8.4.3 Evaluation of knock models for single cycles

For a correct application, the knock models should be used for the single cycles only. Figure 8.19 shows the histograms of the KI_{end} values for the non-knocking cycles and the KI_{SOK} values for the knocking cycles, equivalent to figure 8.15 for iso-octane. Compared to iso-octane a much lower fraction of the cycles are knocking. The tendencies observed for the mean cycle analysis are confirmed for the single cycles. The Douaud and IFP models obtain the lowest ignition delay time equations and therefore the highest number of correct predictions of the non-knocking cycles. Since the fraction of non-knocking cycles is very high, the importance in the overall fitness function evaluation is strong. The IFP models has the lowest KI_{SOK} values and therefore the worst $f_{fit,knock}$ value. Due to the lower predicted ignition delay times, the Heufer model obtains a better $f_{fit,knock}$, but a worse f_{fit} result. The 3-Arrhenius approach has the best prediction of the knocking
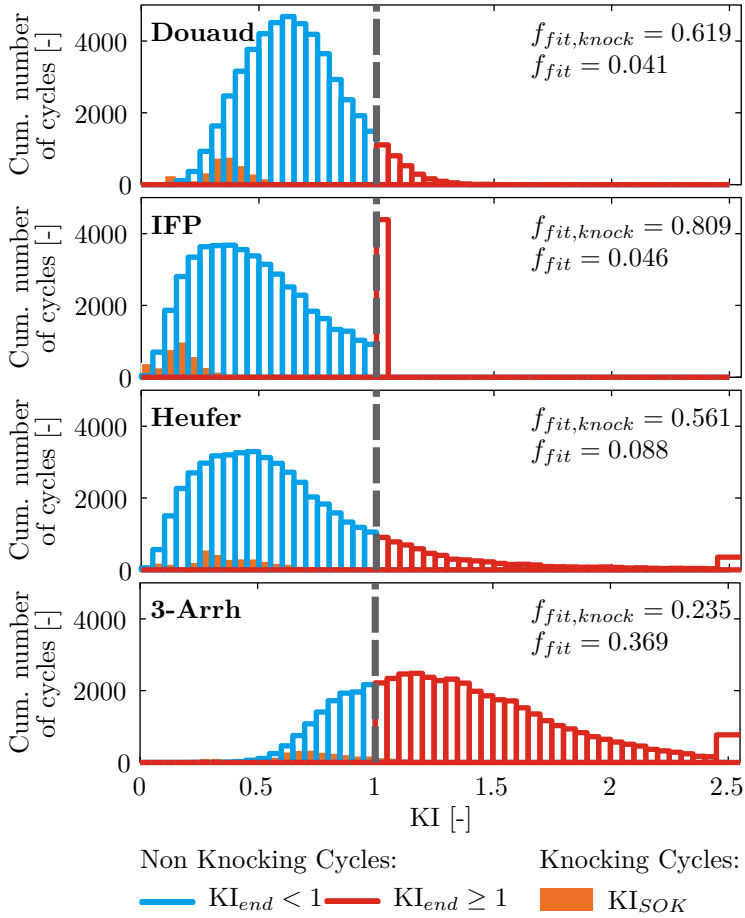
Figure 8.19: *Knock model results for the single cycles. Histogram of knock model KI value at end of cycle for non-knocking cycles: correct predictions in blue, incorrect predictions in red. Histogram of KI value at SOK timing for the knocking cycles.*
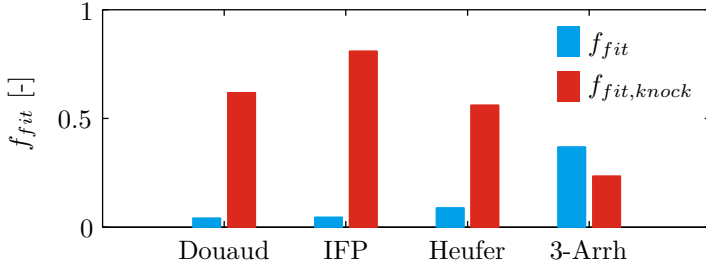
Figure 8.20: *Fitness function values (eq. 6.8 and 6.9) for knock prediction evaluation for all single cycles in the Douaud, IFP, Heufer and 3-Arrhenius knock models (see table 6.2).*

cycles. Many of the non-knocking cycles are however predicted incorrectly, resulting in an overall fitness function value much higher than for the other correlations. The fitness function results for the ethanol single cycles are summarized in figure 8.20.

8.5 Knock model comparison ethanol and iso-octane

After a separate analysis of the knock models for ethanol and iso-octane, a comparison between both fuels can now be made. Figure 8.21 shows the pressures, unburned temperatures, mass fractions burned, ignition delay times and knock integrals for both fuels in the same operating point. Due to evaporative cooling, ethanol has lower temperatures, which leads to slower combustion and a lower peak pressure. Because of the strong sensitivity on the pressure and temperature, ethanol has a higher ignition delay time around peak pressure. The two-stage ignition behavior of iso-octane can clearly be seen in the ignition delay time profile. Out of both fuels only iso-octane knocks under the given conditions. Because of the lower ignition delay time for iso-octane, KI integrates the fastest and obtains an accurate knock prediction. For ethanol in this operating point no knock is detected. However the KI value continues to integrate until late in the cycle and predicts knock around 25°CAaTDCf. This behavior is discussed in figure 8.19.

The good knock resistance of ethanol is typically associated with the absence of a two-stage ignition - and thus high ignition delay times
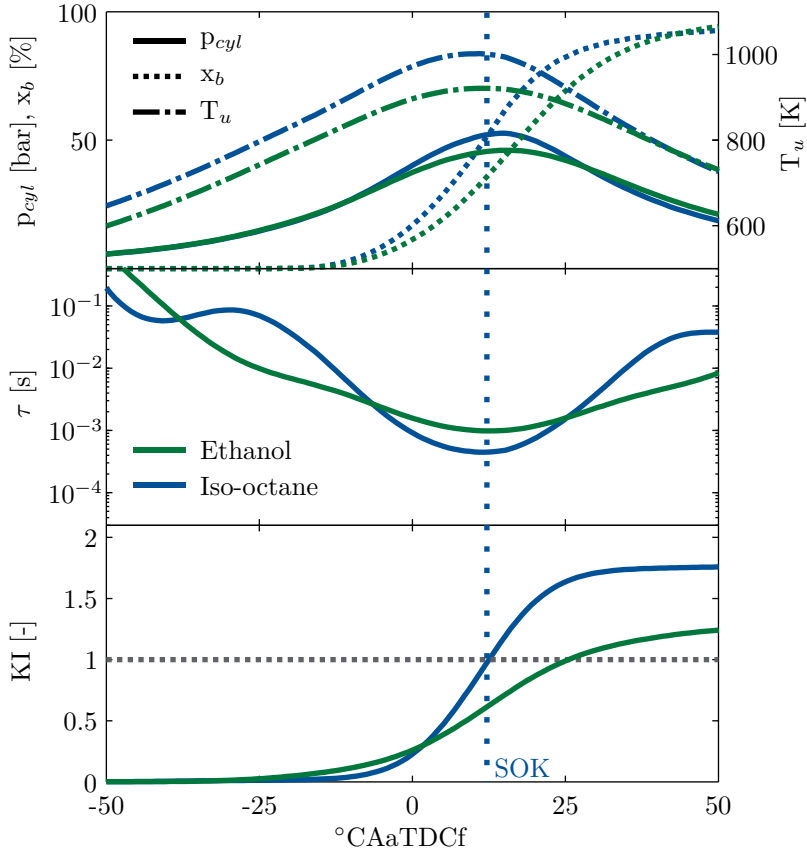
Figure 8.21: *Pressure, unburned temperature, mass fraction burned, ignition delay times and KI for iso-octane and ethanol in the same operating point 5000 rpm, T_{in}=120° C, 36.00° CA SA. Only knock for iso-octane.*

in the low and intermediate temperature range - and the evaporative cooling effect, leading to relatively low temperatures. The chemical and cooling effects on the knock resistance of ethanol can be separated using the knock models. Figure 8.22 shows the results for the ignition delay time and the knock integral when using the same pressure, temperature and mass fraction burned data for both fuels. Under the assumption that the combustion cycles are the same for both ethanol and iso-octane

(same operating point as in figure 8.21), the effect of charge cooling is ruled out. In this case the ignition delay time for ethanol is lower than for iso-octane and knock is predicted by the model earlier in the cycle. Based on the selected ignition delay time correlations, the ignition delay time for ethanol is lower than that of iso-octane in much of the operating range, especially at high temperatures and when the flattening of the
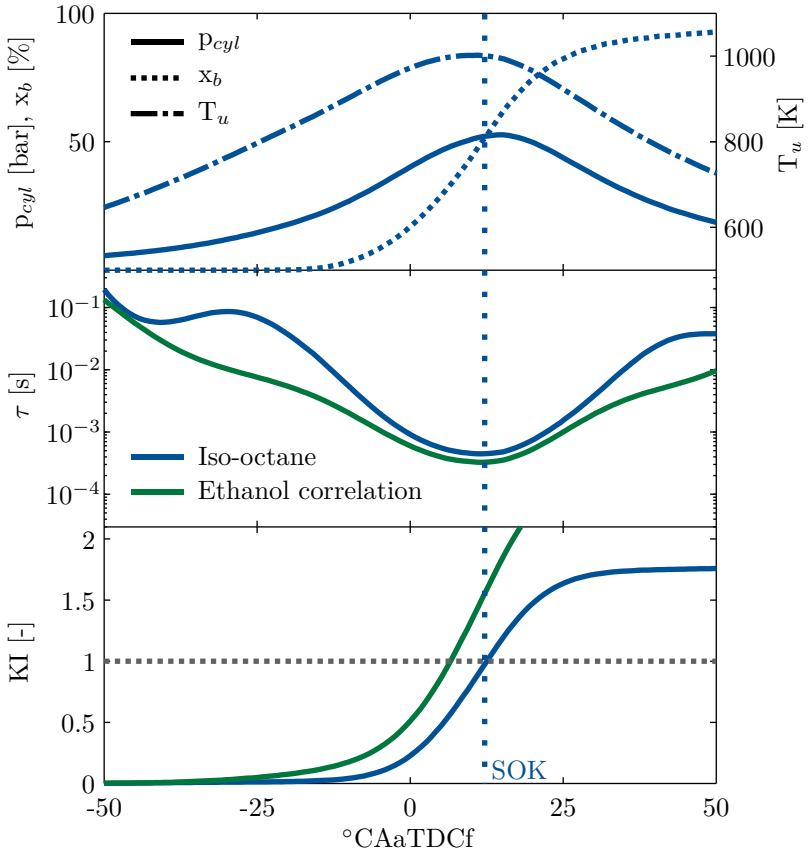
Figure 8.22: *Pressure, unburned temperature, mass fraction burned, ignition delay times and KI for iso-octane in operating point 5000 rpm, T_{in}=120° C, 36.00° CA SA. Ignition delay time and KI for ethanol applied to iso-octane measurement data.*

ignition delay time of ethanol towards lower temperatures is included. It can be concluded that the cooling effect of ethanol has a stronger influence on knock suppression than the chemical effects.

8.6 Correction functions for wall influence

From the evaluation of the different knock models it is apparent that there is a conflict between correct predictions of the onset of knock and the correct predictions of non-knocking cycles. The underlying idea of the knock integral is that the knock phenomenon is cumulative. The integration continues during the expansion and the last part of the combustion. During this time the pressure and temperature remain high and the corresponding ignition delay time contributes to the knock integral. The results of the knock detection algorithm (figure 8.11) show that for both fuels there is no knock after 70% of fuel mass burned. Once this point has passed, even though the temperature remains high, knock is not initiated. In chapter 7 the geometry of the combustion chamber is presented including the position of a spherical flame front at different mass fractions burned. Figure 7.1 shows that when 70% of the fuel mass is burned the flame has reached the exhaust side wall, is very close to the side wall and has moved into the squish zone located at the intake side. At this point the influence of the walls on the unburned mixture are dominating such that knock becomes almost impossible. The cylinder walls act as a heat sink and cool down the gases in its vicinity, thus inhibiting auto-ignition. The knock integral does not take into account this behavior. Another option is to stop the integration of the knock integral at the peak of the low pass filtered pressure. The results show however that many of the cycles have the onset of knock after the peak pressure.

A correction function is needed that models the reducing probability of knock towards the end of the cycle. Several approaches have been introduced in section 7.2.3. A correction function equal to one corresponds to the original knock integral. A first approach is the beta function in equation 7.7. The second function is inspired by the Wiebe form and is given in equation 7.8. The beta function has only one parameter; the Wiebe function has two. These parameters are calibrated to the measurement data set. For further analysis the Goldsborough model is chosen for iso-octane and the Cancino 3-Arrhenius model for ethanol. These two models contain the highest level of accuracy with
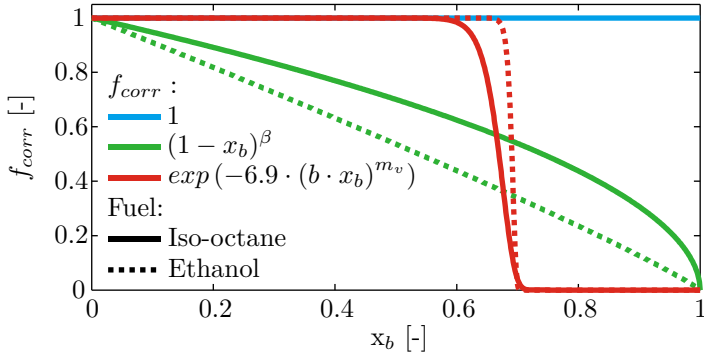
Figure 8.23: *Correction functions (eq. 7.6-7.8) modeling the decreasing probability of knock towards the end of combustion versus mass fraction burned. Best values obtained for ethanol and iso-octane are presented.*

respect to the ignition delay time and yield the best prediction for the SOK for their respective fuels.

The correction functions corresponding to the best solutions for both fuels can be seen in figure 8.23. The beta function decreases gradually as a function of mass fraction burned. The Wiebe functions have a cut-off at 70% mass fraction burned, which corresponds well to the observation that there are almost no knocking cycles after 70% of the fuel mass burned. The histograms of the KI values at the end of the cycle and at SOK for the Goldsborough model with the different correction functions are presented in figure 8.24. The first histogram corresponds to figure 8.16 in which the overall fitness function is high due to the high number of incorrectly predicted non-knocking cycles. The beta function reduces significantly the number of wrong non-knocking cycles by gradually reducing the probability of knock. This correction function however increases artificially the ignition delay time already at the beginning of combustion, resulting in lower KI values at SOK and a deteriorated fitness function for the knocking cycles. The Wiebe function only affects the end of the combustion and improves the prediction of the non-knocking cycles better than the beta function. The fitness function for the knocking cycles increases only slightly compared to the original knock integral. The Wiebe function also better represents the observations made in the cycle statistical analysis.
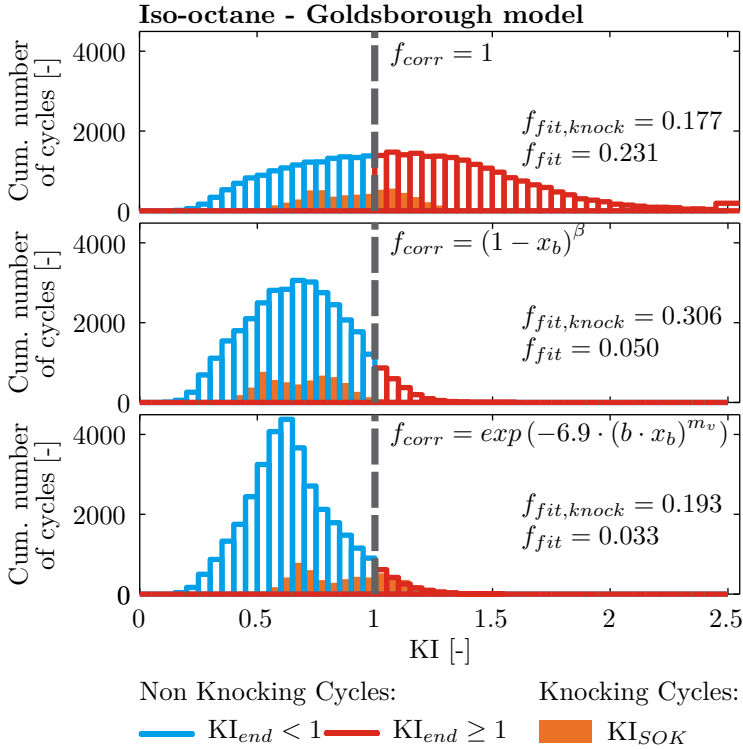
Figure 8.24: *Goldsborough knock model results for the single cycles with different correction functions. Histogram of knock model KI value at end of cycle for non-knocking cycles: correct predictions in blue, incorrect predictions in red. Histogram of KI value at SOK timing for the knocking cycles.*

Figures 8.23 and 8.24 show the best results for the Wiebe correction function (eq. 7.8) with a high m_v value. The reduction in the probability of knock is thus much more sudden than previously expected. For both fuels, the cut-off lies at 70% of fuel mass burned. This agrees well with the given combustion chamber geometry. For a different engine and combustion chamber the best parameters for the correction function may be different. Of most general interest is the formulation of a knock model that can be applied to all engines without much tuning of the specific model parameters. A last way of modeling the influence of
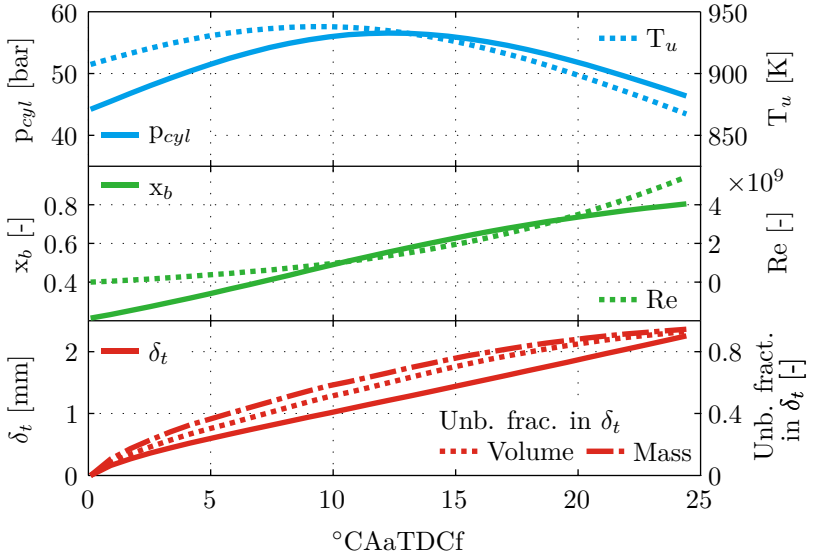
Figure 8.25: *Pressure, unburned temperature, burned mass fraction, Reynolds number, thermal boundary layer thickness and unburned fraction (mass and volume) within the boundary for the operating point 4500rpm, T_{in}=80 °C, 43.50° CA SA, ethanol.*

the cylinder walls, that is considered, is presented at the end of section 7.2.3. The thickness of the thermal boundary layer is modeled as a function of the thermal diffusivity, time and a Reynolds number. The volume fraction of the unburned gas within the thermal boundary is tabulated as a function of mass fraction burned, piston position and thermal boundary layer thickness. The mass fraction of the unburned gas within the boundary is derived from the volume fraction by estimating the temperature of the boundary layer.

The results for a representative operating point are shown in figure 8.25. The thermal boundary layer thickness grows steadily throughout the cycle. At the 70% of fuel mass burned mark, for this case, the thermal boundary layer measures around 1.5 mm. At this point, the volume fraction of the remaining 30% within the boundary layer is almost 80%. Looking at figure 7.1, a spherical flame at x_b=70% has reached the exhaust wall and is very close to the side wall, where the influence of the boundary layer is strong. On the intake side the

flame has moved into the squish area. The distance to the intake wall is still larger than the boundary layer, but distance to piston and cylinder head is small at this point and even at 20°CAaTDC the squish area lies within the thermal boundary. Only above the valve pockets unburned gas not within the boundary layer can be found, making up around 20% of the unburned volume at this point. Due to the difference in temperature between the bulk unburned zone and the thermal boundary layer, the mass fraction of unburned gas in the boundary layer is a few percentages higher than the volume fraction at over 83%. The unburned gas not in the boundary layer then only makes up 5% of the total mass in the cylinder.

A correction function for the influence of the thermal boundary layer on the knock behavior can be defined based on the mass fraction of unburned fuel within the boundary, as given in equation 7.10. The correction function excludes the possibility of knock when a certain threshold mass fraction of unburned fuel in the thermal boundary is reached. Contrary to the Wiebe and beta correction functions the mass fraction burned is not the decisive parameter. The development of the thermal boundary layer changes for different operating points and so does the mass fraction at which knock becomes improbable. Figure 8.26 shows the mass fraction of the unburned gas within the thermal boundary layer and the corresponding correction functions for the spark timing variation of figure 8.10. It was shown in figure 8.10 that earlier
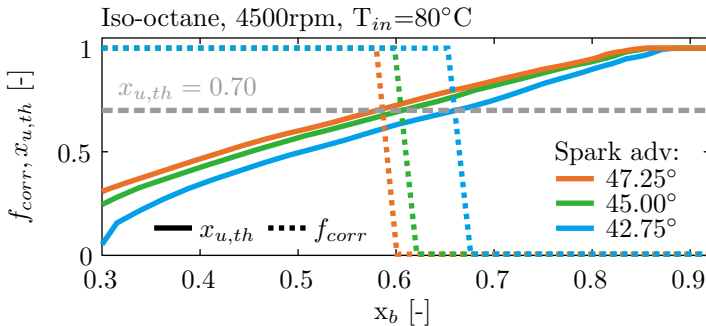
Figure 8.26: *Mass fraction of the unburned gas within the thermal boundary layer and correction function according to eq. 7.10 for $x_{u,th,thr}$=0.70 and operating points 4500rpm, T_{in}=80 °C, 47.25, 45.00, 42.75° CA SA, iso-octane.*
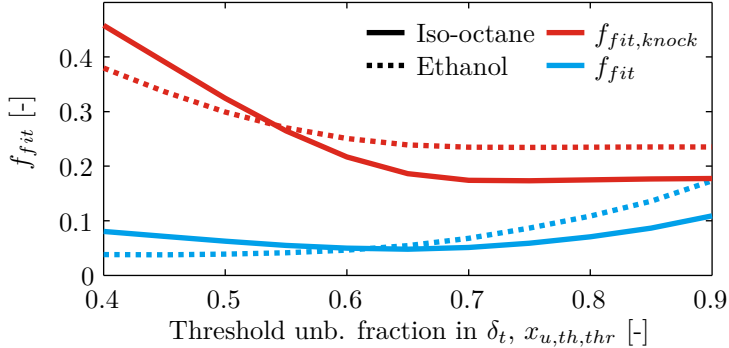
Figure 8.27: *Fitness function values (eq. 6.8 and 6.9) for the single cycles with the correction function based on the thermal boundary layer (eq. 7.10) for iso-octane (Goldsborough) and ethanol (3-Arrh) as a function of the threshold value for the mass fraction of unburned gas in the boundary layer.*

spark timings lead to knock at lower mass fractions. The correction function based on the boundary layer model is able to capture this behavior.

In figure 8.26 a threshold value for the mass fraction of the unburned in the boundary layer of 70% is used. For the correction function based on the thermal boundary layer the threshold value is the only parameter. The knock model fitness functions for all single cycles are evaluated for a variation of the threshold value and the results for both fuels are shown in figure 8.27. The fitness function for the knocking cycles, $f_{fit,knock}$, increases with a lower threshold value for the unburned fraction in the boundary layer. At low threshold values the integration of KI is cut off before SOK and the values of KI at SOK deteriorate, leading to an increase of $f_{fit,knock}$. At high threshold values the fitness function flattens out, because there is no interference of the correction function with the KI values at SOK. An opposite effect can be seen for the overall fitness function, f_{fit}. It increases towards higher threshold values because the cut off from the correction function is too late and many non-knocking cycles are incorrectly predicted as knocking cycles. This effect is stronger for ethanol, because of the higher number of non-knocking cycles. The overall fitness function increases as well towards low fitness function values because of the increase of $f_{fit,knock}$. An
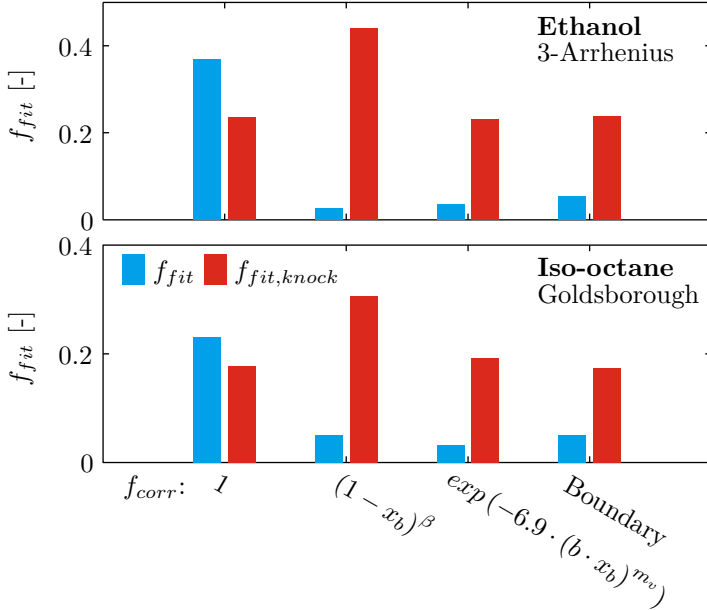
Figure 8.28: *Fitness function values (eq. 6.8 and 6.9) for the single cycles with different correction functions (one (eq. 7.6), beta (eq. 7.7), Wiebe (eq. 7.8) and based on the mass fraction of unburned fuel in the boundary layer (eq. 7.10)) for iso-octane (Goldsborough) and ethanol (3-Arrhenius).*

optimal value for $x_{u,th,thr}$ for both fuels seems to lie between 60 and 70 %, where the correct prediction of the timing for the onset of knock is not inhibited, but the incorrect prediction of non-knocking cycles is stopped by the correction function.

A comparison of the fitness function values for the evaluation of the knock models with the different correction functions for all single cycles and both fuels is shown in figure 8.28. For the threshold value $x_{u,th,thr}$ a mass fraction of 65% is used. When the influence of the boundary layer is not modeled - and the correction function is equal to one - the prediction of the knocking cycles is good and $f_{fit,knock}$ is low. In this case the integration for KI continues until the end of combustion and many of the non-knocking cycles are predicted incorrectly

resulting in a high value for the overall fitness function. Using the beta correction function (eq. 7.7) reduces the number of incorrectly predicted non-knocking cycles and thus the overall fitness function, but the effect of the correction function begins already with the start of combustion and the KI value at SOK is reduced leading to worse predictions for the knocking cycles and a high value for $f_{fit,knock}$. The influence of the boundary layer only comes later in the cycle and much more sudden. This behavior is modeled more accurately by the Wiebe correction function (eq. 7.8). This function leads to a good prediction of both the knocking and the non-knocking cycles. However the accuracy of this correction function depends strongly on the optimization of its parameters. For the measurements in this work 70% of the fuel mass burned marked the tipping point for knock in a cycle. If at this point no auto-ignition in the end gas has taken place, the influence of the boundary layer significantly reduces the probability of still having a knocking cycle. The cycle-statistical analysis has shown that the timing for the onset of knock is strongly dependent on the operating point. A correction function based only on a maximum mass fraction burned cannot capture the complete behavior. Therefore a correction function based on the build up of the thermal boundary layer is introduced (eq. 7.10). This function calculates the mass fraction of the unburned gas within the boundary layer zone and thus takes into account the specific operating point as well as the geometry of the combustion chamber. The analysis has shown that a characteristic fraction of around 65% of fuel mass contained in the boundary layer marks a threshold value for the occurrence of knock. A correction function modeling the influence of the thermal boundary layer can thus be derived from the geometry of the engine alone.

9 Conclusions and outlook

In the current work knock in an ethanol fueled engine is studied and the results are compared to the behavior of iso-octane under the same conditions. The most important results are achieved in two topics. First the analysis of the experimental data, which includes a cycle-statistical approach, shows at which point during the cycle knock is initiated and which cycles are most prone to knock. These results are then linked to the specific geometry of the combustion chamber. Secondly the knock models are tested against the measurement data. The sensitivity of the knock prediction towards the ignition delay time correlations are shown. The need to model the reducing probability of knock towards the end of the cycle is demonstrated. A model approach, that includes the observations towards the geometry of the combustion chamber, is introduced and takes into account the influence of the vicinity of the walls in a thermal boundary layer approach.

9.1 Conclusions

A test bench for a single cylinder spark ignition engine has been built up and fit to the purposes of the study of knock. Spark timing variations are performed at variable speeds and intake temperatures with wide open throttle and stoichiometric, premixed conditions. Two fuels are selected for the study: ethanol and iso-octane. Ethanol is injected with direct injection; for iso-octane port fuel injection is used. The properties of both fuels are compared in detail in order to understand the differences in the measurement results. Ethanol has a higher octane number, higher flame speed, lower energy density and a higher latent heat of vaporization compared to iso-octane. At nominally the same operating point ethanol produces a much higher torque than iso-octane.

This can be attributed to the higher volumetric efficiency, caused by the stronger cooling effect of ethanol. The air mass flow of ethanol is increased by up to 20% compared to iso-octane, with larger differences at higher speeds.

The thermodynamic analysis of the measurement data is carried out using the 0D/1D simulation software GT-Power, which includes calculations for the gas exchange phase. For both the mean cycle of each operating point as well as all the single cycles the heat release rates and two-zone temperatures are calculated. A thermal model for the oil and coolant is included and a sensitivity analysis for the parameters on the unburned gas temperature is carried out. The evaporative cooling effect of ethanol leads to overall lower temperatures, that offset the nominally higher laminar flame speed, and cause slower combustion and longer burn durations compared to iso-octane.

Many researchers have published methods for the detection of knock. A comparison of some of the most common knock indices is given and a good correlation between the results is observed. A knock index should be independent of the operating points. A knock detection criterion is defined based on the maximum amplitude of the pressure oscillations relative to the reference non-knocking conditions at late spark timings. A much better knock resistance is observed for ethanol compared to iso-octane. For ethanol much earlier spark timings are required to obtain knocking conditions. Consequently the total number of recorded knocking cycles for ethanol is lower than for iso-octane. An accurate definition for the timing of the onset of knock is needed when modeling knock. A criterion based on the heat release rate corresponding to the auto-ignition in the end-gas is introduced. This heat release rate always precedes the characteristic pressure oscillations. Different detection criteria lead to a large difference in the mass fraction burned at the start of knock. The average knocking cycle is always faster than the overall mean cycle, however not necessarily the faster burning cycles have the highest knock intensity. A trade-off exists between high pressure and temperature on the one hand and available time on the other. Earlier spark timings lead to knock at lower mass fractions burned. Due to the earlier spark timings required for ethanol to knock, the mass fractions burned at auto-ignition are lower for ethanol compared to iso-octane. Auto-ignition of the end-gas typically occurs between 50 and 70% of the fuel mass burned. After 70% burned the probability of knock is reduced significantly.

An extensive literature review on the ignition characteristics of both

fuels is carried out and an overview of the available ignition delay time measurement data as well as the chemical kinetic models is given. Iso-octane exhibits a so-called two stage ignition behavior with a negative temperature coefficient in the intermediate temperature range. The LLNL kinetic mechanism is selected as the most detailed and widely validated and is used for ignition delay time calculations under the conditions corresponding to the knock measurements on the engine test bench. The results are used to calibrate the parameters of a 3-Arrhenius correlation. Two detailed correlations for the ignition delay time of iso-octane can be found in literature of which the Goldsborough equation is validated against the widest set of experimental data and captures best the two stage behavior of iso-octane. For ethanol much less experimental data and chemical kinetic models are published. Ethanol is considered a fuel with a single stage ignition; however recent experimental work at elevated pressures and low temperatures by Cancino et al. shows a flattening of the linear-log behavior. The Cancino mechanism has been used for chemical kinetic calculations and the data has been fit to a 3-Arrhenius approach. For ethanol only single Arrhenius equations are available for the ignition delay time. The new correlation captures the faster chemistry at low temperatures and high pressure well.

The knock models, proposed by Douaud and by IFP, are selected from the literature review and are compared to the application of the ignition delay time correlations in the knock integral, proposed by Livengood and Wu, for both the mean and the single cycles. An approach to assess the quality of the model is introduced, using fitness evaluation functions. A fitness function for the knocking cycles determines the accuracy of the prediction of the timing for the onset of knock. An overall fitness function also assesses the predictions for the non-knocking cycles. The Douaud and IFP knock models yield good results in predicting a knocking cycle. The timing for the onset of knock is however predicted too late in the cycle. For both fuels the ignition delay time correlation with the highest level of detail produces the best results in predicting the timing for the onset of knock: the 3-Arrhenius correlation based on the Cancino mechanism for the ethanol data and the Goldsborough correlation for iso-octane.

Accurate predictions for the timing of the onset of knock result in a high number of incorrectly predicted non-knocking cycles and vice-verse. It was found that after 70% of fuel mass fraction burned almost none of the cycles start to knock. At this point most of the unburned

gases are very close to the cylinder walls. The flame front has reached the exhaust side, is very close to the side wall and has moved into the squish zone on the intake side. The combustion chamber walls cool down the unburned gases in its vicinity and create a thermal boundary layer. The temperature within the thermal boundary layer zone is much lower compared to the bulk unburned gas. The ignition delay time in the boundary layer is therefore much higher and the occurrence of knock becomes improbable. A new model approach that calculates the unburned mass fraction within the thermal boundary is presented. The model can be derived from the combustion chamber geometry alone and when combined with the knock integral and an accurate ignition delay time correlation yields a reliable and time/cost efficient knock model.

9.2 Outlook

In the current work a knock analysis is performed with standard engine test rig equipment. The results of a knock detection algorithm are linked to the geometry of the engine and good results are achieved for the computationally efficient knock prediction model, with only these limited tools available. Future work would include the further validation of the results. Since the engine under consideration has no optical access, 3D CFD tools can be used to study the spatial distribution of the auto-ignition spots. The ignition delay time correlations can be applied in a knock integral that is solved in the cells of the unburned zone. Alternatively the chemical kinetic models can be solved directly. These simulations can capture the thermal distribution in more detail and predict, next to the timing for the onset of knock, also the location of the auto-ignition. Also the temperature distribution close to the walls as well as the local wall temperatures can be resolved and the thermal boundary layer model, used in this work, can be compared to the simulations. Recent advances in 3D numerical tools for engine simulations allow to resolve part of the turbulence spectrum, thus capturing cyclic variations. Such a simulation model has already been applied to the engine under consideration [228]. When the cyclic variation of the engine can be captured and an auto-ignition model is applied to the unburned zone, the cyclic variation of the knock timing and spatial location can be studied and compared to the results obtained in this work.

An extensive literature review of the published ignition delay time

correlations, chemical kinetic models and ignition delay time measurements is given in this work. The knock model simulations have shown the importance of the accuracy of the ignition delay time correlation. For both fuels in the investigation, the correlation with the highest level of detail has also yielded the best prediction for the timing of the onset of knock. For iso-octane already an extensive set of experimental and modeling data is available. The interest for ethanol has been moderate on this topic so far. Especially the study of the behavior of ethanol at low temperatures and high pressures deserves more attention. For dedicated ethanol engines, the most promising concepts included turbocharging at high compression ratios and the use of EGR. For both fuels the accuracy of the knock model predictions would further benefit of the availability of more ignition delay time measurements and kinetic models validated at higher pressures and for diluted mixtures.

In the current work ethanol and iso-octane are chosen as fuels for the investigation. As explained in the introduction ethanol is used in many different blends throughout the world. The analysis could be repeated for both the low volume and high volume ethanol blends with gasoline. Also in this case the accuracy of the modeling results would be strongly dependent on the availability of reliable ignition delay time correlations for these fuels at the conditions under consideration.

Bibliography

[1] Renewable Fuels Association, "Ethanol Industry Outlook 2008 - 2013."

[2] OECD - FAO, "Agricultural Outlook 2011 - 2020."

[3] J. J. Cheng and G. R. Timilsina, "Status and barriers of advanced biofuel technologies: A review," *Renewable Energy*, vol. 36, pp. 3541–3549, Dec. 2011.

[4] S. Lee and Y. Shah, *Biofuels and bioenergy : processes and technologies*. CRC Press, 2013.

[5] V. Subramani and S. K. Gangwal, "A Review of Recent Literature to Search for an Efficient Catalytic Process for the Conversion of Syngas to Ethanol," *Energy & Fuels*, vol. 22, pp. 814–839, Jan. 2008.

[6] "US Energy Independence and Security Act," 2007.

[7] E. I. Wiloso, R. Heijungs, and G. R. de Snoo, "LCA of second generation bioethanol: A review and some issues to be resolved for good LCA practice," *Renewable and Sustainable Energy Reviews*, vol. 16, pp. 5295–5308, Sept. 2012.

[8] A. L. Borrion, M. C. McManus, and G. P. Hammond, "Environmental life cycle assessment of lignocellulosic conversion to ethanol: A review," *Renewable and Sustainable Energy Reviews*, vol. 16, pp. 4638–4650, Sept. 2012.

[9] "Automotive fuels - Unleaded petrol - Requirements and test methods; EN 228:2012."

[10] U.S. Department of Energy, "http://www.afdc.energy.gov/," 2014.

[11] "Kraftstoff für Kraftfahrzeuge - Ethanolkraftstoff (E85) für Kraftfahrzeuge - Anforderungen und Prüfverfahren; CEN/TS 15293:2011."

[12] "Standard Specification for Ethanol Fuel Blends for Flexible-Fuel Automotive Spark-Ignition Engines; ASTM D5798."

[13] Environment and Health Administration in Stockholm, "http://www.miljofordon.se/tanka," 2014.

[14] E85.biz, "http://www.e85.biz/," 2014.

[15] R. Schmalzried, "http://www.bioe.ch/," 2014.

[16] D. McCullough, "http://www.e85prices.com/," 2014.

[17] H. Pacini and S. Silveira, "Consumer choice between ethanol and gasoline: Lessons from Brazil and Sweden," *Energy Policy*, vol. 39, pp. 6936–6942, Nov. 2011.

[18] M. Brusstar and M. Bakenhus, "Economical, High-Efficiency Engine Technologies for Alcohol Fuels," in *15th Int. Symposium on Alcohol Fuels*, ISAF, 2005.

[19] J. E. Anderson, U. Kramer, S. A. Mueller, and T. J. Wallington, "Octane Numbers of Ethanol- and Methanol- Gasoline Blends Estimated from Molar Concentrations," *Energy & Fuels*, vol. 24, no. 12, pp. 6576–6585, 2010.

[20] N. Jeuland, X. Montagne, and X. Gautrot, "Potentiality of Ethanol as a Fuel for Dedicated Engine," *Oil and Gas Science and Technology*, vol. 59, no. 6, pp. 559–570, 2004.

[21] P. A. Caton, L. J. Hamilton, and J. S. Cowart, "An Experimental and Modelling Investigation Into the Comparative Knock and Performance Characteristics of E85, Gasohol [E10] and Regular Unleaded Gasoline [87 (R+M)/2]," *SAE Technical Paper*, no. 2007-01-0473, 2007.

[22] A. A. Al-Farayedhi, A. M. Al-Dawood, and P. Gandhidasan, "Effects of Blending Crude Ethanol with Unleaded Gasoline on Exhaust Emissions of SI Engine," *SAE Technical Paper*, no. 2000-01-2857, 2000.

[23] M. A.-R. Sadiq Al-Baghdadi, "Performance study of a four-stroke spark ignition engine working with both of hydrogen and ethyl alcohol as supplementary fuel," *International Journal of Hydrogen Energy*, vol. 25, no. 10, pp. 1005–1009, 2000.

[24] L. Li, Z. Liu, H. Wang, B. Deng, Z. Xiao, Z. Wang, C. Gong, and Y. Su, "Combustion and emissions of ethanol fuel (E100) in a small SI engine," *SAE Technical Paper*, no. 2003-01-3262, 2003.

[25] T. Topgül, H. S. Yücesu, C. Çinar, and A. Koca, "The effects of ethanol-unleaded gasoline blends and ignition timing on engine performance and exhaust emissions," *Renewable Energy*, vol. 31, no. 15, pp. 2534–2542, 2006.

[26] K. Nakata, S. Utsumi, A. Ota, K. Kawatake, T. Kawai, and T. Tsunooka, "The Effect of Ethanol Fuel on a Spark Ignition Engine," *SAE Technical Paper*, no. 2006-01-3380, 2006.

[27] F. A. Martínez and A. R. Ganji, "Performance and Exhaust Emissions of a Single-Cylinder Utility Engine Using Ethanol Fuel," *SAE Technical Paper*, no. 2006-32-0078, 2006.

[28] P. E. Kapus, A. Fuerhapter, H. Fuchs, and G. K. Fraidl, "Ethanol Direct Injection on Turbocharged SI Engines - Potential and Challenges," *SAE Technical Paper*, no. 2007-01-1408, 2007.

[29] C. Pana, N. Negurescu, M. G. Popa, A. Cernat, and D. Soare, "Aspects of the use of ethanol in spark ignition engine," *SAE Technical Paper*, no. 2007-01-2040, 2007.

[30] K. Nakama, J. Kusaka, and Y. Daisho, "Effect of Ethanol on Knock in Spark Ignition Gasoline Engines," *SAE Technical Paper*, no. 2008-32-0020, 2008.

[31] A. Kumar, D. S. Khatri, and M. K. G. Babu, "Experimental Investigations on the Performance, Combustion and Emission Characteristics of Alcohol-Blended Gasoline in a Fuel-Injected Spark Ignition Engine," *SAE Technical Paper*, no. 2008-28-0068, 2008.

[32] A. Cairns, A. Todd, P. Aleiferis, N. Fraser, and J. Malcolm, "A Study of Alcohol Blended Fuels in an Unthrottled Single Cylinder Spark Ignition Engine," *SAE Technical Paper*, no. 2010-01-0618, 2010.

[33] S. Richard, G. Font, F. Le Berr, O. Grasset, and M. Fremovici, "On the Use of System Simulation to Explore the Potential of Innovative Combustion Systems: Methodology and Application to Highly Downsized SI Engines Running with Ethanol-Gasoline Blends," *SAE Technical Paper*, no. 2011-01-0408, 2011.

[34] J. A. Caton, "A Thermodynamic Evaluation of the Use of Alcohol Fuels in a Spark-Ignition Engine," *SAE Technical Paper*, no. 2009-01-2621, 2009.

[35] A. A. Abdel-Rahman and M. M. Osman, "Experimental Investigation on Varying the Compression Ratio of SI Engine Working Under Different Ethanol - Gasoline Fuel Blends," *International Journal of Energy Research*, vol. 21, no. 1, pp. 31–40, 1997.

[36] W.-D. Hsieh, R.-H. Chen, T.-L. Wu, and T.-H. Lin, "Engine performance and pollutant emission of an SI engine using ethanol-gasoline blended fuels," *Atmospheric Environment*, vol. 36, no. 3, pp. 403–410, 2002.

[37] M. Al-Hasan, "Effect of ethanol-unleaded gasoline blends on engine performance and exhaust emission," *Energy Conversion and Management*, vol. 44, no. 9, pp. 1547–1561, 2003.

[38] C.-W. Wu, R.-H. Chen, J.-Y. Pu, and T.-H. Lin, "The influence of air-fuel ratio on engine performance and pollutant emission of an SI engine using ethanol-gasoline-blended fuels," *Atmospheric Environment*, vol. 38, no. 40, pp. 7093–7100, 2004.

[39] H. Bayraktar, "Experimental and theoretical investigation of using gasoline-ethanol blends in spark-ignition engines," *Renewable Energy*, vol. 30, no. 11, pp. 1733–1747, 2005.

[40] H. Sandquist, M. Karlsson, and I. Denbratt, "Influence of ethanol content in gasoline on speciated emissions from a direct-injection stratified charge SI engine," *SAE Technical Paper*, no. 2001-01-1206, 2001.

[41] L. G. Dodge, K. Shouse, J. Grogan, D. M. DLeone, K. A. Whitney, and P. M. Merritt, "Development of an Ethanol-Fueled Ultra-Low Emissions Vehicle," *SAE Technical Paper*, no. 981358, 1998.

[42] R. A. Amaral and J. R. Sodré, "Aldehyde emissions from an ethanol-fuelled vehicle as influenced by engine geometric parameters," *SAE Technical Paper*, no. 2001-01-1998, 2001.

[43] S. G. Poulopoulos, D. P. Samaras, and C. J. Philippopoulos, "Regulated and unregulated emissions from an internal combustion engine operating on ethanol-containing fuels," *Atmospheric Environment*, vol. 35, no. 26, pp. 4399–4406, 2001.

[44] E. Zervas, X. Montagne, and J. Lahaye, "Emission of Alcohols and Carbonyl Compounds from a Spark Ignition Engine. Influence of Fuel and Air/Fuel Equivalence Ratio," *Environmental Science & Technology*, vol. 36, no. 11, pp. 2414–2421, 2002.

[45] B.-Q. He, W. Jian-Xin, J.-M. Hao, X.-G. Yan, and J.-H. Xiao, "A study on emission characteristics of an EFI engine with ethanol blended gasoline fuels," *Atmospheric Environment*, vol. 37, no. 7, pp. 949–957, 2003.

[46] L. P. Wyszynski, C. R. Stone, and G. Kalghatgi, "The volumetric efficiency of direct and port injection gasoline engines with different fuels," *SAE Technical Paper*, no. 2002-01-0839, 2002.

[47] E. Kasseris and J. Heywood, "Charge Cooling Effects on Knock Limits in SI DI Engines Using Gasoline/Ethanol Blends: Part 1-Quantifying Charge Cooling," *SAE Technical Paper*, no. 2012-01-1275, 2012.

[48] J. D. Smith and V. Sick, "The Prospects of Using Alcohol-Based Fuels in Stratified-Charge, Spark-Ignition Engines," *SAE Technical Paper*, no. 2007-01-4034, 2007.

[49] S. Taniguchi, K. Yoshida, and Y. Tsukasaki, "Feasibility Study of Ethanol Applications to A Direct Injection Gasoline Engine," *SAE Technical Paper*, no. 2007-01-2037, 2007.

[50] S. Brewster, "Initial Development of a Turbo-charged Direct Injection E100 Combustion System," *SAE Technical Paper*, no. 2007-01-3625, 2007.

[51] C. D. Marriott, M. A. Wiles, J. M. Gwidt, and S. E. Parrish, "Development of a Naturally Aspirated Spark Ignition Direct-Injection, Flex-Fuel Engine," *SAE Technical Paper*, no. 2008-01-0319, 2008.

[52] P. Whitaker, Y. Shen, C. Spanner, H. Fuchs, A. Agarwal, and K. Byrd, "Development of the Combustion System for a Flexible Fuel Turbocharged Direct Injection Engine," *SAE Technical Paper*, no. 2010-01-0585, 2010.

[53] P. Grabner, H. Eichlseder, and G. Eckhard, "Potential of E85 Direct Injection for Passenger Car Application," *SAE Technical Paper*, no. 2010-01-2086, 2010.

[54] A. Cairns, P. Stansfield, N. Fraser, H. Blaxill, M. Gold, J. Rogerson, and C. Goodfellow, "A Study of Gasoline-Alcohol Blended

Fuels in an Advanced Turbocharged DISI Engine," *SAE Technical Paper*, no. 2009-01-0138, 2009.

[55] K. S. Hoyer, W. R. Moore, and K. Confer, "A Simulation Method to Guide DISI Engine Redesign for Increased Efficiency using Alcohol Fuel Blends," *SAE Int. J. Engines*, vol. 3, no. 1, pp. 889–902, 2010.

[56] P. G. Aleiferis, J. Serras-Pereira, Z. van Romunde, J. Caine, and M. Wirth, "Mechanisms of spray formation and combustion from a multi-hole injector with E85 and gasoline," *Combustion and Flame*, vol. 157, no. 4, pp. 735–756, 2010.

[57] D. Turner, H. Xu, R. F. Cracknell, V. Natarajan, and X. Chen, "Combustion performance of bio-ethanol at various blend ratios in a gasoline direct injection engine," *Fuel*, vol. 90, no. 5, pp. 1999–2006, 2011.

[58] P. Sementa, B. M. Vaglieco, and F. Catapano, "Non-Intrusive Investigation in a Small GDI Optical Engine Fuelled with Gasoline and Ethanol," *SAE Int. J. Engines*, vol. 4, no. 1, pp. 50–66, 2011.

[59] L. Chen, R. Stone, and D. Richardson, "A study of mixture preparation and PM emissions using a direct injection engine fuelled with stoichiometric gasoline/ethanol blends," *Fuel*, vol. 96, no. 0, pp. 120–130, 2012.

[60] M. Brusstar and C. L. Gray, "High Efiiciency with Future Alcohol Fuels in a Stoichiometric Medium Duty Spark Ignition Engine," *SAE Technical Paper*, no. 2007-01-3993, 2007.

[61] J. Gingrich, T. Alger, and B. Sullivan, "Ethanol Flex-fuel Engine Improvements with Exhaust Gas Recirculation and Hydrogen Enrichment," *SAE Technical Paper*, no. 2009-01-0140, pp. 58–65, 2009.

[62] J. Ritzinger, T. Koch, J. Lehmann, and K. Boulouchos, "Influence of Fuel Composition and Combustion Process on Thermodynamic Parameters of SI Engines," *SAE Technical Paper*, no. 2012-01-1633, 2012.

[63] F. Yüksel and B. Yüksel, "The use of ethanol-gasoline blend as a fuel in an SI engine," *Renewable Energy*, vol. 29, no. 7, pp. 1181–1191, 2004.

[64] D. R. Cohn, L. Bromberg, and J. B. Heywood, "Direct Injection Ethanol Boosted Gasoline Engines: Biofuel Leveraging For

Cost Effective Reduction of Oil Dependence and CO2 Emissions," *Massachusetts Institute of Technology*, 2005.

[65] L. Bromberg, D. R. Cohn, and J. B. Heywood, "Calculations of knock suppression in highly turbocharged gasoline/ethanol engines using direct ethanol injection," *LFEE*, no. 2006-01 RP, 2006.

[66] P. N. Blumberg, L. Bromberg, H. Kang, and C. Tai, "Simulation of High-Efficiency, Heavy-Duty SI Engines Using Direct Injection of Alcohol for Knock Avoidance," *SAE Technical Paper*, no. 2008-01-2447, 2008.

[67] R. A. Stein, C. J. House, and T. G. Leone, "Optimal Use of E85 in a turbocharged Direct Injection Engine," *SAE Technical Paper*, no. 2009-01-1490, 2009.

[68] A. Kumar, D. S. Khatri, and M. K. G. Babu, "An Investigation of Potential and Challenges with Higher Ethanol-gasoline Blend on a Single Cylinder Spark Ignition Research Engine," *SAE Technical Paper*, no. 2009-01-0137, 2009.

[69] M. Pontopiddan, C. F. Damasceno, G. Montanari, and S. Bonfiglioli, "Detailed Study of Ethanol In-cylinder Combustion Behavior by means of a Numerical Virtual Engine model Approach," *SAE Technical Paper*, no. 2005-01-3989, 2005.

[70] F. Jehlik, M. Jones, P. Shepherd, J. M. Norbeck, K. Johnson, and M. McClanahan, "Development of a Low-Emission, Dedicated Ethanol-Fuel Vehicle with Cold-Start Distillation System," *SAE Technical Paper*, no. 1999-01-0611, 1999.

[71] R. C. Clemente, E. Werninghaus, E. P. D. Coelho, and L. A. S. Ferraz, "Development of an Internal Combustion Alcohol Fueled Engine," *SAE Technical Paper*, no. 2001-01-3917, 2001.

[72] G. W. Davis and E. T. Heil, "The Development and Performance of a High Blend Ethanol Fueled Vehicle," *SAE Technical Paper*, no. 2000-01-1602, 2000.

[73] T. Tsunooka, H. Y., S. Utsumi, T. Kawai, and Y. Sonoda, "High Concentration Ethanol Effect on SI Engine Cold Startability," *SAE Technical Paper*, no. 2007-01-2036, 2007.

[74] K. Owen, T. Coley, and C. S. Weaver, *Automotive fuels reference book*. Society of Automotive Engineers, 1995.

[75] K. Kar, T. Last, C. Haywood, and R. Raine, "Measurement of Vapor Pressures and Enthalpies of Vaporization of Gasoline and

Ethanol Blends and Their Effects on Mixture Preparation in an SI Engine," *SAE Technical Paper*, no. 2008-01-0317, 2008.

[76] J. B. Heywood, *Internal combustion engine fundamentals*. McGraw-Hill, 1988.

[77] O. L. Gülder, "Turbulent premixed flame propagation models for different combustion regimes," *Symposium (International) on Combustion*, vol. 23, no. 1, pp. 743–750, 1991.

[78] D. Bradley, M. Lawes, and M. S. Mansour, "Correlation of turbulent burning velocities of ethanol-air, measured in a fan-stirred bomb up to 1.2 MPa," *Combustion and Flame*, vol. 158, no. 1, pp. 123–138, 2011.

[79] J. Vancoillie, S. Verhelst, and J. Demuynck, "Laminar Burning Velocity Correlations for Methanol-Air and Ethanol-Air Mixtures Valid at SI Engine Conditions," *SAE Technical Paper*, no. 2011-01-0846, 2011.

[80] F. N. Egolfopoulos, D. X. Du, and C. K. Law, "A study on ethanol oxidation kinetics in laminar premixed flames, flow reactors, and shock tubes," *Symposium (International) on Combustion*, vol. 24, no. 1, pp. 833–841, 1992.

[81] S. Y. Liao, D. M. Jiang, Z. H. Huang, K. Zeng, and Q. Cheng, "Determination of the laminar burning velocities for mixtures of ethanol and air at elevated temperatures," *Applied Thermal Engineering*, vol. 27, no. 2-3, pp. 374–380, 2007.

[82] A. A. Konnov, R. J. Meuwissen, and L. P. H. de Goey, "The temperature dependence of the laminar burning velocity of ethanol flames," *Proceedings of the Combustion Institute*, vol. 33, no. 1, pp. 1011–1019, 2011.

[83] O. L. Gülder, "Laminar burning velocities of methanol, ethanol and isooctane-air mixtures," *Symposium (International) on Combustion*, vol. 19, no. 1, pp. 275–281, 1982.

[84] J. P. J. van Lipzig, E. J. K. Nilsson, L. P. H. de Goey, and A. A. Konnov, "Laminar burning velocities of n-heptane, iso-octane, ethanol and their binary and tertiary mixtures," *Fuel*, vol. 90, no. 8, pp. 2773–2781, 2011.

[85] D. Bradley, M. Lawes, and M. S. Mansour, "Explosion bomb measurements of ethanol-air laminar gaseous flame characteristics at

pressures up to 1.4 MPa," *Combustion and Flame*, vol. 156, no. 7, pp. 1462–1470, 2009.

[86] P. S. Veloo, Y. L. Wang, F. N. Egolfopoulos, and C. K. West-brook, "A comparative experimental and computational study of methanol, ethanol, and n-butanol flames," *Combustion and Flame*, vol. 157, no. 10, pp. 1989–2004, 2010.

[87] M. Metghalchi and J. C. Keck, "Burning velocities of mixtures of air with methanol, isooctane, and indolene at high pressure and temperature," *Combustion and Flame*, vol. 48, pp. 191–210, 1982.

[88] D. Bradley, R. A. Hicks, M. Lawes, C. G. W. Sheppard, and R. Woolley, "The Measurement of Laminar Burning Velocities and Markstein Numbers for Iso-octane-Air and Iso-octane-n-Heptane-Air Mixtures at Elevated Temperatures and Pressures in an Explosion Bomb," *Combustion and Flame*, vol. 115, no. 1-2, pp. 126–144, 1998.

[89] J. Beeckmann, S. Kruse, and N. Peters, "Effect of Ethanol and n-Butanol on Standard Gasoline Regarding Laminar Burning Velocities," *SAE Technical Paper*, no. 2010-01-1452, 2010.

[90] Y. Huang, C. J. Sung, and J. A. Eng, "Laminar flame speeds of primary reference fuels and reformer gas mixtures," *Combustion and Flame*, vol. 139, no. 3, pp. 239–251, 2004.

[91] S. Jerzembeck, N. Peters, P. Pepiot-Desjardins, and H. Pitsch, "Laminar burning velocities at high pressure for primary reference fuels and gasoline: Experimental and numerical investigation," *Combustion and Flame*, vol. 156, no. 2, pp. 292–301, 2009.

[92] O. L. Gülder, "Burning velocities of ethanol-isooctane blends," *Combustion and Flame*, vol. 56, no. 3, pp. 261–268, 1984.

[93] G. Broustail, P. Seers, F. Halter, G. Moréac, and C. Mounaim-Rousselle, "Experimental determination of laminar burning velocity for butanol and ethanol iso-octane blends," *Fuel*, vol. 90, no. 1, pp. 1–6, 2011.

[94] G. Woschni, "A Universally Applicable Equation for the Instantaneous Heat Transfer Coefficient in the Internal Combustion Engine," *SAE Technical Paper*, no. 670931, 1967.

[95] O. Maiwald, *Experimentelle Untersuchungen und mathematische Modellierung von Verbrennungsprozessen in Motoren mit homo-*

gener Selbstzündung. Dissertation, Universität Karlsruhe (TH), 2005.

[96] P. V. Puzinauskas, "Examination of Methods Used to Characterize Engine Knock," *SAE Technical Paper*, no. 920808, 1992.

[97] M. Rothe, T. Heidenreich, U. Spicher, and A. Schubert, "Knock Behavior of SI-Engines: Thermodynamic Analysis of Knock Onset Locations and Knock Intensities," *SAE Technical Paper*, no. 2006-01-0225, 2006.

[98] V. Mittal, B. M. Revier, and J. B. Heywood, "Phenomena that Determine Knock Onset in Spark-Ignition Engines," *SAE Technical Paper*, no. 2007-01-0007, 2007.

[99] G. Brecq, A. Ramesh, M. Tazerout, and O. Le Corre, "An Experimental Study of Knock in a Natural Gas Fuelled Spark Ignition Engine," *SAE Technical Paper*, no. 2001-01-3562, 2001.

[100] X. Zhen, Y. Wang, S. Xu, Y. Zhu, C. Tao, T. Xu, and M. Song, "The engine knock analysis - An overview," *Applied Energy*, vol. 92, pp. 628–636, 2012.

[101] W. S. Wayne, N. N. Clark, and C. M. Atkinson, "A Parametric Study of Knock Control Strategies for a Bi-Fuel Engine," *SAE Technical Paper*, no. 980895, 1998.

[102] G. Fontana, F. Bozza, E. Galloni, and D. Siano, "Experimental and Numerical Analyses for the Characterization of the Cyclic Dispersion and Knock Occurrence in a Small-Size SI Engine," *SAE Technical Paper*, no. 2010-32-0069, 2010.

[103] J. M. Borg, G. Saikalis, S. Oho, and K. C. Cheok, "Knock Signal Analysis Using the Discrete Wavelet Transform," *SAE Technical Paper*, no. 2006-01-0226, 2006.

[104] N. Cavina, E. Corti, G. Minelli, D. Moro, and L. Solieri, "Knock Indexes Normalization Methodologies," *SAE Technical Paper*, no. 2006-01-2998, 2006.

[105] R. Worret, S. Bernhardt, F. Schwarz, and U. Spicher, "Application of Different Cylinder Pressure Based Knock Detection Methods in Spark Ignition Engines," *SAE Technical Paper*, no. 2002-01-1668, 2002.

[106] E. Corti and D. Moro, "Knock Indexes Thresholds Setting Methodology," *SAE Technical Paper*, no. 2007-01-1508, 2007.

[107] J. C. Zavala and C. Folkerts, "Knock Detection and Estimation Based on Heat Release Strategies," *SAE Technical Paper*, no. 2011-01-1409, 2011.

[108] C. Lämmle, *Numerical and experimental study of flame propagation and knock in a compressed natural gas engine.* PhD thesis, ETH Zurich, 2005.

[109] J. Warnatz, U. Maas, and R. W. Dibble, *Combustion: Physical and Chemical Fundamentals, Modeling and Simulation, Experiments, Pollutant Formation.* Springer Berlin Heidelberg, 2006.

[110] F. M. Haas, M. Chaos, and F. L. Dryer, "Low and intermediate temperature oxidation of ethanol and ethanol-PRF blends: An experimental and modeling study," *Combustion and Flame*, vol. 156, no. 12, pp. 2346–2350, 2009.

[111] I. Z. Syed, A. Mukherjee, and J. D. Naber, "Numerical Simulation of Autoignition of Gasoline-Ethanol/Air Mixtures under Different Conditions of Pressure, Temperature, Dilution, and Equivalence Ratio," *SAE Technical Paper*, no. 2011-01-0341, 2011.

[112] A. Yates, A. Bell, and A. Swarts, "Insights relating to the autoignition characteristics of alcohol fuels," *Fuel*, vol. 89, no. 1, pp. 83–93, 2010.

[113] D. J. Vermeer, J. W. Meyer, and A. K. Oppenheim, "Autoignition of hydrocarbons behind reflected shock waves," *Combustion and Flame*, vol. 18, pp. 327–336, June 1972.

[114] A. Burcat, W. Pitz, and C. Westbrook, "Comparative ignition of hexane and octane isomers in a shock tube," *International conference on shock waves and shock tubes*, vol. 18, pp. 771 – 780, 1993.

[115] K. Fieweger, R. Blumenthal, and G. Adomeit, "Shock-tube investigations on the self-ignition of hydrocarbon-air mixtures at high pressures," *Symposium (International) on Combustion*, vol. 25, no. 1, pp. 1579–1585, 1994.

[116] R. Blumenthal, K. Fieweger, K. H. Komp, and G. Adomeit, "Gas Dynamic Features of Self Ignition of Non Diluted Fuel/Air Mixtures at High Pressure," *Combustion Science and Technology*, vol. 113, pp. 137–166, Mar. 1996.

[117] K. Fieweger, R. Blumenthal, and G. Adomeit, "Self-ignition of S.I. engine model fuels: A shock tube investigation at high pressure," *Combustion and Flame*, vol. 109, pp. 599–619, June 1997.

[118] D. F. Davidson, M. A. Oehlschlaeger, J. T. Herbon, and R. K. Hanson, "Shock tube measurements of iso-octane ignition times and OH concentration time histories," *Proceedings of the Combustion Institute*, vol. 29, no. 1, pp. 1295–1301, 2002.

[119] M. A. Oehlschlaeger, D. F. Davidson, J. T. Herbon, and R. K. Hanson, "Shock tube measurements of branched alkane ignition times and OH concentration time histories," *International Journal of Chemical Kinetics*, vol. 36, pp. 67–78, Jan. 2004.

[120] D. F. Davidson, B. M. Gauthier, and R. K. Hanson, "Shock tube ignition measurements of iso-octane/air and toluene/air at high pressures," *Proceedings of the Combustion Institute*, vol. 30, pp. 1175–1182, Jan. 2005.

[121] M. S. P. Kahandawala, S. A. P. Corera, S. Williams, C. D. Carter, and S. S. Sidhu, "Investigation of kinetics of iso-octane ignition under scramjet conditions," *International Journal of Chemical Kinetics*, vol. 38, pp. 194–201, Mar. 2006.

[122] Y. Sakai, H. Ozawa, T. Ogura, A. Miyoshi, M. Koshi, and W. J. Pitz, "Effects of Toluene Addition to Primary Reference Fuel at High Temperature," *SAE Technical Paper*, no. 2007-01-4104, 2007.

[123] M. Yahyaoui, N. Djebaïli-Chaumeix, P. Dagaut, C.-E. Paillard, and S. Gail, "Experimental and modelling study of gasoline surrogate mixtures oxidation in jet stirred reactor and shock tube," *Proceedings of the Combustion Institute*, vol. 31, pp. 385–391, Jan. 2007.

[124] H.-P. S. Shen, J. Vanderover, and M. A. Oehlschlaeger, "A shock tube study of iso-octane ignition at elevated pressures: The influence of diluent gases," *Combustion and Flame*, vol. 155, pp. 739–755, Dec. 2008.

[125] M. Hartmann, I. Gushterova, M. Fikri, C. Schulz, R. Schieß l, and U. Maas, "Auto-ignition of toluene-doped n-heptane and iso-octane/air mixtures: High-pressure shock-tube experiments and kinetics modeling," *Combustion and Flame*, vol. 158, pp. 172–178, Jan. 2011.

[126] T. Malewicki, A. Comandini, and K. Brezinsky, "Experimental and modeling study on the pyrolysis and oxidation of iso-octane," *Proceedings of the Combustion Institute*, vol. 34, no. 1, pp. 353–360, 2013.

[127] S. Li, A. Campos, D. F. Davidson, and R. K. Hanson, "Shock tube measurements of branched alkane ignition delay times," *Fuel*, vol. 118, pp. 398–405, Feb. 2014.

[128] M. P. Halstead, L. J. Kirsch, and C. P. Quinn, "The autoignition of hydrocarbon fuels at high temperatures and pressures - Fitting of a mathematical model," *Combustion and Flame*, vol. 30, no. 0, pp. 45–60, 1977.

[129] J. F. Griffiths, P. A. Halford-Maw, and D. J. Rose, "Fundamental features of hydrocarbon autoignition in a rapid compression machine," *Combustion and Flame*, vol. 95, pp. 291–306, Nov. 1993.

[130] R. Minetti, M. Ribaucour, M. Carlier, and L. R. Sochet, "Autoignition Delays of a Series of Linear and Branched Chain Alkanes in the Intermediate Range of Temperature," *Combustion Science and Technology*, vol. 113, pp. 179–192, Mar. 1996.

[131] R. Minetti, M. Carlier, M. Ribaucour, E. Therssen, and L. R. Sochet, "Comparison of oxidation and autoignition of the two primary reference fuels by rapid compression," *Symposium (International) on Combustion*, vol. 26, no. 1, pp. 747–753, 1996.

[132] C. V. Callahan, T. J. Held, F. L. Dryer, R. Minetti, M. Ribaucour, L. R. Sochet, T. Faravelli, P. Gaffuri, and E. Rani, "Experimental data and kinetic modeling of primary reference fuel mixtures," *Symposium (International) on Combustion*, vol. 26, no. 1, pp. 739–746, 1996.

[133] J. F. Griffiths, P. A. Halford-Maw, and C. Mohamed, "Spontaneous ignition delays as a diagnostic of the propensity of alkanes to cause engine knock," *Combustion and Flame*, vol. 111, pp. 327–337, Dec. 1997.

[134] S. Tanaka, F. Ayala, J. C. Keck, and J. B. Heywood, "Two-stage ignition in HCCI combustion and HCCI control by fuels and additives," *Combustion and Flame*, vol. 132, pp. 219–239, Jan. 2003.

[135] X. He, M. T. Donovan, B. T. Zigler, T. R. Palmer, S. M. Walton, M. S. Wooldridge, and A. Atreya, "An experimental and model-

ing study of iso-octane ignition delay times under homogeneous charge compression ignition conditions," *Combustion and Flame*, vol. 142, pp. 266–275, Aug. 2005.

[136] S. M. Walton, X. He, B. T. Zigler, M. S. Wooldridge, and A. Atreya, "An experimental investigation of iso-octane ignition phenomena," *Combustion and Flame*, vol. 150, pp. 246–262, Aug. 2007.

[137] X. He, S. M. Walton, B. T. Zigler, M. S. Wooldridge, and A. Atreya, "Experimental investigation of the intermediates of isooctane during ignition," *International Journal of Chemical Kinetics*, vol. 39, pp. 498–517, Sept. 2007.

[138] G. Mittal and C.-J. Sung, "Homogeneous charge compression ignition of binary fuel blends," *Combustion and Flame*, vol. 155, pp. 431–439, Nov. 2008.

[139] C. F. Cullis and E. J. Newitt, "The Gaseous Oxidation of Aliphatic Alcohols. I. Ethyl alcohol: The Products Formed in the Early Stages," *Proceedings of the Royal Society of London. Series A, Mathematical and Physical Sciences*, vol. 237, no. 1211, pp. 530–542, 1956.

[140] J. A. Barnard and H. W. D. Hughes, "The pyrolysis of ethanol," *Transactions of the Faraday Society*, vol. 56, no. 0, pp. 55–63, 1960.

[141] D. F. Cooke, M. G. Dodson, and A. Williams, "A shock-tube study of the ignition of methanol and ethanol with oxygen," *Combustion and Flame*, vol. 16, no. 3, pp. 233–236, 1971.

[142] K. Natarajan and K. A. Bhaskaran, "Experimental and analytical investigation of high temperature ignition of ethanol," *Proc Int Symp Shock Tubes Waves*, vol. 13, p. 834, 1981.

[143] A. A. Borisov, V. M. Zamanskii, A. A. Konnov, V. V. Lissyanskii, S. A. Rusakov, and G. I. Skachkov, "High-temperature ignition of mixtures of ethanol and acetaldehyde with oxygen," *Sov. J. Chem. Phys.*, vol. 4, pp. 2561–2575, 1989.

[144] M. P. Dunphy and J. M. Simmie, "High-temperature oxidation of ethanol. Part 1.-Ignition delays in shock waves," *Journal of the Chemical Society, Faraday Transactions*, vol. 87, no. 11, pp. 1691–1696, 1991.

[145] H. J. Curran, M. P. Dunphy, J. M. Simmie, C. K. Westbrook, and W. J. Pitz, "Shock tube ignition of ethanol, isobutene and MTBE: Experiments and modeling," *Symposium (International) on Combustion*, vol. 24, no. 1, pp. 769–776, 1992.

[146] K. A. Heufer and H. Olivier, "Determination of ignition delay times of different hydrocarbons in a new high pressure shock tube," *Shock Waves*, vol. 20, no. 4, pp. 307–316, 2010.

[147] L. R. Cancino, M. Fikri, A. A. M. Oliveira, and C. Schulz, "Measurement and Chemical Kinetics Modeling of Shock-Induced Ignition of Ethanol-Air Mixtures," *Energy & Fuels*, vol. 24, no. 5, pp. 2830–2840, 2010.

[148] C. Lee, S. Vranckx, K. A. Heufer, S. V. Khomik, Y. Uygun, H. Olivier, and R. X. Fernandez, "On the Chemical Kinetics of Ethanol Oxidation: Shock Tube, Rapid Compression Machine and Detailed Modeling Study," *Zeitschrift für Physikalische Chemie*, vol. 226, no. 1, pp. 1–28, 2011.

[149] J. Li, A. Kazakov, M. Chaos, and F. L. Dryer, "Chemical Kinetics of Ethanol Oxidation," in *5th US Combustion Meeting*, (San Diego), 2007.

[150] M. Fikri, J. Herzler, R. Starke, C. Schulz, P. Roth, and G. T. Kalghatgi, "Autoignition of gasoline surrogates mixtures at intermediate temperatures and high pressures," *Combustion and Flame*, vol. 152, no. 1-2, pp. 276–281, 2008.

[151] M. P. Halstead, L. J. Kirsch, A. Prothero, and C. P. Quinn, "A Mathematical Model for Hydrocarbon Autoignition at High Pressures," *Proceedings of the Royal Society of London. A. Mathematical and Physical Sciences*, vol. 346, pp. 515–538, Nov. 1975.

[152] R. A. Cox and J. A. Cole, "Chemical aspects of the autoignition of hydrocarbon-air mixtures," *Combustion and Flame*, vol. 60, pp. 109–123, May 1985.

[153] E. I. Axelsson, K. Brezinsky, F. L. Dryer, W. J. Pitz, and C. K. Westbrook, "Chemical kinetic modeling of the oxidation of large alkane fuels: N-octane and iso-octane," *Symposium (International) on Combustion*, vol. 21, no. 1, pp. 783–793, 1988.

[154] E. Axelsson and L.-G. Rosengren, "Isooctane combustion in a flat flame," *Combustion and Flame*, vol. 62, pp. 91–93, Oct. 1985.

[155] K. Brezinsky and F. L. Dryer, "Molecular Structure and Component Blending Effects on Knock Related Chemistry," *SAE Technical Paper*, no. 872109, 1987.

[156] J. A. Barnard and B. A. Harwood, "Slow combustion and cool-flame behavior of iso-octane," *Combustion and Flame*, vol. 21, pp. 345–355, Dec. 1973.

[157] C. K. Westbrook, J. Warnatz, and W. J. Pitz, "A detailed chemical kinetic reaction mechanism for the oxidation of iso-octane and n-heptane over an extended temperature range and its application to analysis of engine knock," *Symposium (International) on Combustion*, vol. 22, no. 1, pp. 893–901, 1989.

[158] M. Schreiber, A. Sadat Sakak, A. Lingens, and J. F. Griffiths, "A reduced thermokinetic model for the autoignition of fuels with variable octane ratings," *Symposium (International) on Combustion*, vol. 25, no. 1, pp. 933–940, 1994.

[159] Y. Simon, G. Scacchi, and F. Baronnet, "Études des réactions d'oxydation du n-heptane et de l'isooctane," *Canadian Journal of Chemistry*, vol. 74, pp. 1391–1402, July 1996.

[160] P. Dagaut, M. Reuillon, and M. Cathonnet, "High Pressure Oxidation of Liquid Fuels From Low to High Temperature. 1. n-Heptane and iso-Octane.," *Combustion Science and Technology*, vol. 95, pp. 233–260, Dec. 1993.

[161] G. M. Côme, V. Warth, P. A. Glaude, R. Fournet, F. Battin-Leclerc, and G. Scacchi, "Computer-aided design of gas-phase oxidation mechanisms - Application to the modeling of n-heptane and iso-octane oxidation," *Symposium (International) on Combustion*, vol. 26, no. 1, pp. 755–762, 1996.

[162] D. Bradley, M. Lawes, C. G. W. Sheppard, and R. Woolley, "Study of turbulence and combustion interaction: measurement and prediction of the rate of turbulent burning," *Periodic Report*, vol. 30, p. 94, 1994.

[163] H. Pitsch, N. Peters, and K. Seshadri, "Numerical and asymptotic studies of the structure of premixed iso-octane flames," *Symposium (International) on Combustion*, vol. 26, no. 1, pp. 763–771, 1996.

[164] A. Ciajolo, A. D'Anna, and R. Mercogijano, "Slow-Combustion of n-Heptane, iso-Octane and a Toluene/n-Heptane Mixture," *Combustion Science and Technology*, vol. 90, pp. 357–371, Apr. 1993.

[165] A. D'Anna, R. Mercoguano, R. Barbella, and A. Ciajolo, "Low Temperature Oxidation Chemistry of iso-Octane under High Pressure Conditions," *Combustion Science and Technology*, vol. 83, pp. 217–232, June 1992.

[166] E. Ranzi, T. Faravelli, P. Gaffuri, A. Sogaro, A. D'Anna, and A. Ciajolo, "A wide-range modeling study of iso-octane oxidation," *Combustion and Flame*, vol. 108, pp. 24–42, Jan. 1997.

[167] F. L. Dryer and K. Brezinsky, "A Flow Reactor Study of the Oxidation of n-Octane and Iso-Octane," *Combustion Science and Technology*, vol. 45, pp. 199–212, Feb. 1986.

[168] S. G. Davis and C. K. Law, "Laminar flame speeds and oxidation kinetics of iso-octane-air and n-heptane-air flames," *Symposium (International) on Combustion*, vol. 27, no. 1, pp. 521–527, 1998.

[169] H. J. Curran, W. J. Pitz, C. K. Westbrook, G. V. Callahan, and F. L. Dryer, "Oxidation of automotive primary reference fuels at elevated pressures," *Symposium (International) on Combustion*, vol. 27, no. 1, pp. 379–387, 1998.

[170] H. K. Ciezki and G. Adomeit, "Shock-tube investigation of self-ignition of n-heptane-air mixtures under engine relevant conditions," *Combustion and Flame*, vol. 93, pp. 421–433, June 1993.

[171] U. C. Müller, M. Bollig, and N. Peters, "Approximations for burning velocities and markstein numbers for lean hydrocarbon and methanol flames," *Combustion and Flame*, vol. 108, pp. 349–356, Feb. 1997.

[172] R. Ogink and V. Golovitchev, "Gasoline HCCI Modeling: Computer Program Combining Detailed Chemistry and Gas Exchange Processes," *SAE Technical Paper*, no. 2001-01-3614, 2001.

[173] J.-S. Chen, T. A. Litzinger, and H. J. Curran, "The Lean Oxidation of Iso-Octane in the Intermediate Temperature Regime at Elevated Pressures," *Combustion Science and Technology*, vol. 156, pp. 49–79, July 2000.

[174] H. J. Curran, P. Gaffuri, W. J. Pitz, and C. K. Westbrook, "A comprehensive modeling study of iso-octane oxidation," *Combustion and Flame*, vol. 129, pp. 253–280, May 2002.

[175] H. S. Soyhan, F. Mauss, and C. Sorusbay, "Chemical kinetic modeling of combustion in internal combustion engines using reduced chemistry," *Combustion Science and Technology*, vol. 174, pp. 73–91, Nov. 2002.

[176] S. Tanaka, F. Ayala, and J. C. Keck, "A reduced chemical kinetic model for HCCI combustion of primary reference fuels in a rapid compression machine," *Combustion and Flame*, vol. 133, pp. 467–481, June 2003.

[177] F. Buda, R. Bounaceur, V. Warth, P. A. Glaude, R. Fournet, and F. Battin-Leclerc, "Progress toward a unified detailed kinetic model for the autoignition of alkanes from C4 to C10 between 600 and 1200 K," *Combustion and Flame*, vol. 142, pp. 170–186, July 2005.

[178] H. Machrafi, K. Lombaert, S. Cavadias, P. Guibert, and J. Amouroux, "Reduced chemical reaction mechanisms: experimental and HCCI modelling investigations of autoignition processes of iso-octane in internal combustion engines," *Fuel*, vol. 84, pp. 2330–2340, Dec. 2005.

[179] M. Jia and M. Xie, "A chemical kinetics model of iso-octane oxidation for HCCI engines," *Fuel*, vol. 85, pp. 2593–2604, Dec. 2006.

[180] T. Lu and C. K. Law, "Linear time reduction of large kinetic mechanisms with directed relation graph: n-Heptane and iso-octane," *Combustion and Flame*, vol. 144, pp. 24–36, Jan. 2006.

[181] O. C. Kwon, M. I. Hassan, and G. M. Faeth, "Flame/Stretch Interactions of Premixed Fuel-Vapor/O/N Flames," *Journal of Propulsion and Power*, vol. 16, pp. 513–522, May 2000.

[182] M. Chaos, A. Kazakov, Z. Zhao, and F. L. Dryer, "A high-temperature chemical kinetic model for primary reference fuels," *International Journal of Chemical Kinetics*, vol. 39, pp. 399–414, July 2007.

[183] Y. Ra and R. D. Reitz, "A reduced chemical kinetic model for IC engine combustion simulations with primary reference fuels," *Combustion and Flame*, vol. 155, pp. 713–738, Dec. 2008.

[184] B. M. Gauthier, D. F. Davidson, and R. K. Hanson, "Shock tube determination of ignition delay times in full-blend and surrogate

fuel mixtures," *Combustion and Flame*, vol. 139, pp. 300–311, Dec. 2004.

[185] G. Mittal and C.-J. Sung, "A Rapid Compression Machine for Chemical Kinetics Studies at Elevated Pressures and Temperatures," *Combustion Science and Technology*, vol. 179, pp. 497–530, Mar. 2007.

[186] M. Mehl, W. J. Pitz, M. Sjöberg, and J. E. Dec, "Detailed Kinetic Modeling of Low-Temperature Heat Release for PRF Fuels in an HCCI Engine," *SAE Technical Paper*, no. 2009-01-1806, 2009.

[187] T. Tsurushima, "A new skeletal PRF kinetic model for HCCI combustion," *Proceedings of the Combustion Institute*, vol. 32, no. 2, pp. 2835–2841, 2009.

[188] S. Voglsam and F. Winter, "A global combustion model for simulation of n-heptane and iso-octane self ignition," *Chemical Engineering Journal*, vol. 203, pp. 357–369, Sept. 2012.

[189] K. Kumar, J. E. Freeh, C. J. Sung, and Y. Huang, "Laminar flame speeds of preheated iso-octane /O2/N2 and n-heptane /O2/N2 mixtures," *Journal of propulsion and power*, vol. 23, no. 2, pp. 428–436, 2007.

[190] J. X. Zhou, M. Cordier, C. Mounaïm-Rousselle, and F. Foucher, "Experimental estimate of the laminar burning velocity of iso-octane in oxygen-enriched and CO2-diluted air," *Combustion and Flame*, vol. 158, pp. 2375–2383, Dec. 2011.

[191] Y. Liu, M. Jia, M. Xie, and B. Pang, "Improvement on a skeletal chemical kinetic model of iso-octane for internal combustion engine by using a practical methodology," *Fuel*, vol. 103, pp. 884–891, Jan. 2013.

[192] M. P. Dunphy, P. M. Patterson, and J. M. Simmie, "High-temperature oxidation of ethanol. Part 2.-Kinetic modelling," *Journal of the Chemical Society, Faraday Transactions*, vol. 87, no. 16, pp. 2549–2559, 1991.

[193] A. A. Borisov, V. M. Zamanskii, A. A. Konnov, V. V. Lissyanskii, S. A. Rusakov, and G. I. Skachkov, "A mechanism of high-temperature ethanol ignition," *Sov. J. Chem. Phys.*, vol. 9, pp. 2527–2537, 1992.

[194] T. S. Norton and F. L. Dryer, "An experimental and modeling study of ethanol oxidation kinetics in an atmospheric pressure

flow reactor," *International Journal of Chemical Kinetics*, vol. 24, no. 4, pp. 319–344, 1992.

[195] T. S. Norton and F. L. Dryer, "The flow reactor oxidation of C1-C4 alcohols and MTBE," *Symposium (International) on Combustion*, vol. 23, no. 1, pp. 179–185, 1991.

[196] B. Aboussi, *Etude Experimentale et Modelisation de l'Oxydation de l'Ethanol*. Dissertation, Université d'Orléans, Orleans - France, 1991.

[197] N. M. Marinov, "A detailed chemical kinetic model for high temperature ethanol oxidation," *International Journal of Chemical Kinetics*, vol. 31, no. 3, pp. 183–220, 1999.

[198] P. Saxena and F. A. Williams, "Numerical and experimental studies of ethanol flames," *Proceedings of the Combustion Institute*, vol. 31, no. 1, pp. 1149–1156, 2007.

[199] P. Dagaut and C. Togbe, "Experimental and Modeling Study of the Kinetics of Oxidation of Ethanol-Gasoline Surrogate Mixtures (E85 Surrogate) in a Jet-Stirred Reactor," *Energy & Fuels*, vol. 22, no. 5, pp. 3499–3505, 2008.

[200] O. Röhl and N. Peters, "A Reduced Mechanism for Ethanol Oxidation," in *European Combustion Meeting*, (Wien), 2009.

[201] O. Röhl, S. Jerzembeck, J. Beeckmann, and N. Peters, "Numerical Investigation of Laminar Burning Velocities of High Octane Fuel Blends Containing Ethanol," *SAE Technical Paper*, no. 2009-01-0935, 2009.

[202] I. Z. Syed, Y. Yeliana, A. Mukherjee, J. D. Naber, and D. Michalek, "Numerical Investigation of Laminar Flame Speed of Gasoline - Ethanol/Air Mixtures with Varying Pressure, Temperature and Dilution," *SAE Int. J. Engines*, vol. 3, no. 1, pp. 517–528, 2010.

[203] N. Leplat, P. Dagaut, C. Togbé, and J. Vandooren, "Numerical and experimental study of ethanol combustion and oxidation in laminar premixed flames and in jet-stirred reactor," *Combustion and Flame*, vol. 158, no. 4, pp. 705–725, 2011.

[204] H. Machrafi, S. Cavadias, and J. Amouroux, "The development and experimental validation of a reduced ternary kinetic mechanism for the auto-ignition at HCCI conditions, proposing a global

reaction path for ternary gasoline surrogates," *Fuel Processing Technology*, vol. 90, pp. 247–263, Feb. 2009.

[205] A. D. B. Yates and C. L. Viljoen, "An Improved Empirical Model for Describing Auto-ignition," *SAE Technical Paper*, no. 2008-01-1629, 2008.

[206] S. S. Goldsborough, "A chemical kinetically based ignition delay correlation for iso-octane covering a wide range of conditions including the NTC region," *Combustion and Flame*, vol. 156, pp. 1248–1262, June 2009.

[207] A. M. Douaud and P. Eyzat, "Four-Octane-Number Method for Predicting the Anti-Knock Behavior of Fuels and Engines," *SAE Technical Paper*, no. 780080, 1978.

[208] A. Vandersickel, M. Hartmann, K. Vogel, Y. M. Wright, M. Fikri, R. Starke, C. Schulz, and K. Boulouchos, "The autoignition of practical fuels at HCCI conditions: High-pressure shock tube experiments and phenomenological modeling," *Fuel*, vol. 93, no. 0, pp. 492–501, 2012.

[209] J. C. Livengood and P. C. Wu, "Correlation of autoignition phenomena in internal combustion engines and rapid compression machines," *Symposium (International) on Combustion*, vol. 5, no. 1, pp. 347–356, 1955.

[210] A. Boretti, "Towards 40% efficiency with BMEP exceeding 30 bar in directly injected, turbocharged, spark ignition ethanol engines," *Energy Conversion and Management*, vol. 57, no. 0, pp. 154–166, 2012.

[211] W. S. Wayne, N. N. Clark, and C. M. Atkinson, "Numerical Prediction of Knock in a Bi-Fuel Engine," *SAE Technical Paper*, no. 982533, 1998.

[212] F.-A. Lafossas, M. Castagne, J. P. Dumas, and S. Henriot, "Development and Validation of a Knock Model in Spark Ignition Engines Using a CFD code," *SAE Technical Paper*, no. 2002-01-2701, 2002.

[213] S. Richard, S. Bougrine, G. Font, F.-A. Lafossas, and F. Le Berr, "Réduction d'un modèle de combustion 3D en vue d'obtenir un modèle 0D physique permettant de simuler le dégagement d'énergie, le cliquetis et les émissions de polluants des moteurs à

allumage commandé," *Oil & Gas Science and Technology - Rev. IFP*, vol. 64, no. 3, pp. 223–242, 2009.

[214] S. Bougrine, S. Richard, and D. Veynante, "Modelling and Simulation of the Combustion of Ethanol blended Fuels in a SI Engine using a 0D Coherent Flame Model," *SAE Technical Paper*, no. 2009-24-0016, 2009.

[215] X. Zhen, Y. Wang, S. Xu, and Y. Zhu, "Study of knock in a high compression ratio spark-ignition methanol engine by multi-dimensional simulation," *Energy*, vol. 50, pp. 150–159, Feb. 2013.

[216] A. D. B. Yates, A. Swarts, and C. L. Viljoen, "Correlating Auto-Ignition Delays And Knock-Limited Spark-Advance Data For Different Types Of Fuel," *SAE Technical Paper*, no. 2005-01-2083, 2005.

[217] C. L. Viljoen, A. D. B. Yates, A. Swarts, G. Balfour, and K. Möller, "An Investigation of the Ignition Delay Character of Different Fuel Components and an Assessment of Various Autoignition Modelling Approaches," *SAE Technical Paper*, no. 2005-01-2084, 2005.

[218] F. Bozza, G. Fontana, E. Galloni, and E. Torella, "3D-1D Analyses of the Turbulent Flow Field, Burning Speed and Knock Occurrence in a Turbocharged SI Engine," *SAE Technical Paper*, no. 2007-24-0029, 2007.

[219] S. Sazhin, E. Sazhina, and M. Heikal, "The Shell autoignition model: a new mathematical formulation," *Combustion and Flame*, vol. 117, pp. 529–540, May 1999.

[220] E. Sazhina, S. Sazhin, M. Heikal, and C. Marooney, "The Shell autoignition model: applications to gasoline and diesel fuels," *Fuel*, vol. 78, pp. 389–401, Mar. 1999.

[221] P. Eckert, S.-C. Kong, and R. D. Reitz, "Modeling Autoignition and Engine Knock Under Spark Ignition Conditions," *SAE Technical Paper*, no. 2003-01-0011, 2003.

[222] K. Nakama, J. Kusaka, and Y. Daisho, "Study of Knock Control in Small Gasoline Engines by Multi-Dimensional Simulation," *SAE Technical Paper*, no. 2006-32-0034, 2006.

[223] V. Giglio, G. Police, N. Rispoli, B. Iorio, and A. di Gaeta, "Experimental Evaluation of Reduced Kinetic Models for the Simulation

of Knock in SI Engines," *SAE Technical Paper*, no. 2011-24-0033, 2011.

[224] M. Mehl, T. Faravelli, E. Ranzi, T. Lucchini, A. Onorati, F. Giavazzi, P. Scorletti, and D. Terna, "Kinetic Modeling of Knock Properties in Internal Combustion Engines," *SAE Technical Paper*, no. 2006-01-3239, 2006.

[225] E. J. Lyford-Pike and J. B. Heywood, "Thermal boundary layer thickness in the cylinder of a spark-ignition engine," *International Journal of Heat and Mass Transfer*, vol. 27, pp. 1873–1878, Oct. 1984.

[226] I. Wiebe, "Halbempirische Formel fur die Verbrennungsgeschwindigkeit," *Verlag der Akademie der Wissenschaften der UdSSR, Moscow*, 1956.

[227] D. E. Franzke, *Beitrag zur Ermittlung eines Klopfkriteriums der ottomotorischen Verbrennung und zur Vorausberechnung der Klopfgrenze.* PhD thesis, University of Munich, 1981.

[228] J. Koch, M. Schmitt, Y. M. Wright, K. Steurs, and K. Boulouchos, "LES Multi-Cycle Analysis of the Combustion Process in a Small SI Engine," *SAE Int. J. Engines*, vol. 7, no. 1, 2014.

Bibliography

List of Figures

List of Tables

Nomenclature

α	Temperature coefficient
β	Pressure coefficient
χ	Concentration
Δp_{95}	95th percentile for $MAPO$ values
ΔT	Difference in temperature
$\dot{m}_{evap}$	Evaporation rate
γ	Pressure exponent in Arrhenius equation
λ	Air-to-fuel ratio
μ	Viscosity
ν	wave number
ϕ	Fuel-to-air ratio
ρ	Density
ρ_b	Burned density
ρ_u	Unburned density
τ	Ignition delay time
τ_{fit}	Ignition delay time correlation (3-Arrh type) fitted to simulation results
τ_h	Ignition delay time in the high temperature region
τ_l	Ignition delay time in the low temperature region
θ	Degree crank angle
θ_{knock}	Crank angle at the onset of knock
$\tilde{p}$	High pass filtered pressure

ζ	Crank angle integration window
A	Constant in Arrhenius equation
a	Thermal diffusivity
A_G	Parameter according to Gülder
AF_{ST}	Stoichiometric air-to-fuel ratio
B	Bore
BTE	Brake thermal efficiency
c	Speed of sound
c_p	Specific heat capacity
CA	Crank angle
CA_{50}	50% evaporation time
$CAaTDCf$	Crank angle after top dead center firing
$CAbTDCf$	Crank angle before top dead center firing
CFD	Computational fluid dynamics
CFR	Cooperative Fuel Research
CNG	Compressed natural gas
$Corr$	Correlation
CoV	Coefficient of Variation
CR	Compression ratio
DI	Direct injection
DL	Damage limit
E	Ethanol content by volume
E_a	Activation energy in Arrhenius equation
E_{mot}	Signal energy of the motored pressure
E_{res}	Signal energy of the pressure oscillations
ECU	Engine control unit
EGR	Exhaust gas recirculation
EVO	Exhaust valve opening
Ex	Expansion factor
f	Frequency

f_{corr}	Correction function for the influence of the cylinder wall
$f_{fit,knock}$	Fitness evaluation function for the knocking cycles and/or operating points
f_{fit}	Fitness evaluation function
f_{va}	Ethanol blending fraction
FFV	Flex fuel vehicles
H_u	Lower heating value
HC	Unburned hydrocarbons
HTC	Heat transfer coefficient
i	Index
I_2	Knock index
IDT	Ignition delay time
$IMEP$	Indicated mean effective pressure
$IMPG$	Integral of the modulus of the pressure gradient
$IMPO$	Integral of the modulus of pressure oscillations
IVC	Intake valve closing
K_n	Knock intensity parameter
KI	Knock integral
KI_{end}	Knock integral value at the end of the cycle
KI_{SOK}	Knock integral value at the onset of knock
KI_{xb}	Knock index based on x_b
KL	Knock limit
$KLSA$	Knock limited spark advanced
$KnTd$	Knocking tendency
L	Latent heat of vaporization
M	Molecular mass
m_f	Fuel mass
m_{air}	Air mass
m_{ST}	Exponent for the turbulent flame speed
m_u	unburned mass

$MAPO$	Maximum amplitude of the pressure oscillations
$MAPO_{95}$	95th percentile for $MAPO_{rel}$ values
$MAPO_{ref}$	MAPO value at late spark timings
$MAPO_{rel}$	MAPO value relative to the value at late spark timings
MBT	Maximum brake torque timing
$meas$	Measured
MON	Motor octane number
N	Engine speed
n	Number of cycles/operating points
n_{ST}	Exponent for the turbulent flame speed
NO_x	Nitrogen oxides
NTC	Negative temperature coefficient
ON	Octane number
Ox	Oxidizer
p	Pressure
p_{cyl}	Cylinder pressure
p_{filt}	High pass filtered pressure
PFI	Port fuel injection
PRF	Primary reference fuel
Q_L	Heat required for vaporization
Q_u	Heat release due to auto-ignition
RCM	Rapid compression machine
Re	Reynolds number
ref	Reference
RON	Research octane number
S	Scaling factor
S_L	Laminar flame speed
S_T	Turbulent flame speed
$SEHRRO$	Signal energy of the heat release rate oscillations
$SEPO$	Signal energy of the pressure oscillations

SI	Spark ignition
sim	Simulation
SOK	Start of knock
$SOK\ HHR$	Start of knock based on heat release rate criterion
$SOK\ p_{crit}$	Start of knock based on pressure oscillation criterion
$SOK\ p_{max}$	Start of knock based on maximum pressure oscillation criterion
T	Temperature
T_{bound}	Temperature in the boundary layer
T_{in}	Intake temperature
T_{IVC}	Temperature at IVC
t_{knock}	Time to the onset of knock
$T_{u,peak}$	Peak unburned temperature
TDC	Top dead center
tot	Total
TWC	Three way catalyst
u'	Turbulence intensity
v	Gas velocity
V_b	Volume fraction burned
v_p	Piston velocity
$V_{u,th}$	Volume fraction of the unburned gas within the boundary layer
WOT	Wide open throttle
x	Distance between the piston and the cylinder head
x_p	Piston position relative to the TDC
x_b	Mass fraction burned
x_{Qu}	Burned mass fraction due to auto-ignition
$x_{u,th,thr}$	Threshold value for the mass fraction of the unburned gas within the boundary layer
$x_{u,th}$	Mass fraction of the unburned gas within the boundary layer

Curriculum Vitae

Personal Data

Name	Karel Frans Hilda Maria Steurs
Date of birth	September 3rd, 1984
Place of birth	Mechelen, Belgium
Nationality	Belgian
Place of residence	Zürich, Switzerland

Education

2007 - 2013	Swiss Federal Institute of Technology, Zürich Aerothermochemistry and Combustion Systems Laboratory *Doctoral student, research scientist and teaching assistant*
2006 - 2007	Swiss Federal Institute of Technology, Zürich *Erasmus exchange studies in Mechanical Engineering with a focus on Energy Flows and Processes*
2002 - 2007	Ghent University, Belgium *Mechanical and Electrotechnical Engineering with a focus on Mechanical Energy Technology*
1996 - 2002	Sint-Jan Berchmanscollege, Westmalle, Belgium *High school degree in Latin - Mathematics*

Publications

Journal Papers

1. U. Gerke, K. Steurs, P. Rebecchi and K. Boulouchos, "Derivation of burning velocities of premixed hydrogen/air flames at engine-

relevant conditions using a single-cylinder compression machine with optical access," *International Journal of Hydrogen Energy*, vol. 35, no. 6, pp. 2566-2577, 2010.

2. M. D. Galus, R.A. Waraich, F. Noembrini, K. Steurs, G. Georges, K. Boulouchos, K.W. Axhausen and G. Andersson, "Integrating Power Systems, Transport Systems and Vehicle Technology for Electric Mobility Impact Assessment and Efficient Control," *IEEE Transactions on Smart Grid*, vol. 3, no. 2, pp. 934-949, 2012.

3. K. Steurs, C. K. Blomberg and K. Boulouchos, "Knock in an Ethanol Fueled Spark Ignition Engine: Detection Methods with Cycle-Statistical Analysis and Predictions Using Different Auto-Ignition Models," *SAE Int. J. Engines*, vol. 7, no. 2, 2014.

4. J. Koch, M. Schmitt, Y. Wright, K. Steurs and K. Boulouchos, "LES Multi-Cycle Analysis of the Combustion Process in a Small SI Engine," *SAE Int. J. Engines*, vol. 7, no. 1, 2014.

5. K. Steurs, C. K. Blomberg and K. Boulouchos, "Formulation of a Knock Model for Ethanol and Iso-Octane under Specific Consideration of the Thermal Boundary Layer within the End-Gas," *SAE Int. J. Engines*, vol. 7, no. 4, 2014.

Conference Papers

1. K. Steurs, Ph. Dietrich and K. Boulouchos, "Energy management strategy for a series hybrid electric sports car," in *Int. Advanced Mobility Forum*, (Geneva, Switzerland), 2010.

2. K. Steurs, Ph. Dietrich and K. Boulouchos, "The improvement of fuel consumption for a plug-in series hybrid electric vehicle when the driving distance is known beforehand," in *Int. Sc. Conf. on Hybrid and Electric Vehicles*, (Reuil-Malmaison), France, 2011.

Reports

1. K. Steurs, Ph. Dietrich and K. Boulouchos, "Ableitung der optimalen Betriebsstrategie eines seriellen Hybridfahrzeuges," in *Final report*, 2012.

2. K. Steurs, P. Obrecht and K. Boulouchos, "Optimal Combustion Systems for Liquid Fuels," in *Final report*, 2014.